Luminosity evaluation and fragmentation studies for the DELPHI experiment at LEP

Christina Zacharatou Jarlskog

LUND
UNIVERSITY

DEPARTMENT OF PHYSICS, LUND 2001

To my children,
Maria Christina and Peter

ISBN 91-7874-126-2
LUNFD6 / (NFFL-7193) 2001

Luminosity evaluation and fragmentation studies for the DELPHI experiment at LEP

By due permission of the Faculty of Mathematics and Natural Science at Lund University to be publicly discussed at lecture hall B of the Department of Physics, on May 28th, 2001, at 10:15 a.m. for the degree of Doctor of Philosophy

by

Christina Zacharatou Jarlskog

Department of Physics, Lund University
Professorsgatan 1
Box 118, S-221 00 Lund
Sweden

This thesis is based on the following articles, included as Appendices A to D:

A *Measurement of the beam parameter variations in DELPHI with the VSAT,* DELPHI 95-150 LEDI 2.

B *VSAT luminosity for the 1995 scan,* DELPHI 2000-005 PHYS 848.

C *Measurement of the beam parameters during the 1995 Z^0 scan with the DELPHI VSAT,* DELPHI 2000-006 PHYS 849.

D *Hadronization corrections to helicity components of the fragmentation functio*n, hep-ph / 0104118, submitted to Eur. Phys. Journal C.

Abstract

The first subject addressed in this thesis is the contribution of the VSAT luminosity to the lineshape analysis, i.e. to the extraction of the mass and width of the Z^0 boson from LEP1 DELPHI data. The VSAT detector has contributed to the lineshape parameter determination by providing a relative luminosity measurement of high accuracy.

The second subject of the thesis is the extraction of the helicity components of the fragmentation function. The analysis is performed on data collected by the DELPHI detector from 1992 to 1995. The study concentrates on the correction required for the hadronization process. Hadronization mainly affects the longitudinal component of the fragmentation function. The corrected measurement is used for the extraction of the strong coupling constant.

Contents

Preface

This dissertation summarizes my participation in the DELPHI experiment. It is based on four reports, which are given as Appendices A to D. The first three Appendices present my work in the VSAT group. Chapter 2 gives an overview of lineshape studies, which is where the VSAT luminosity is used. My involvement in these studies was therefore indirect, as my contribution was mainly on beam parameter evaluation, energy calibration and luminosity determination. Appendix D refers to my second project in DELPHI, namely the fragmentation function component extraction for LEP1. Chapter 4 presents my contribution in detail. My VSAT and QCD efforts are presented here in opposite ways, so-to-speak. The VSAT related Appendices are closer to my work than what is treated in Chapter 2. On the other hand, Chapter 4 is a better account of what I did myself than Appendix D.

As all the work presented in the thesis is team work, I would like to clarify further where my own contribution is hidden.

I will first address the VSAT analysis. During part of the data-taking in 1994 and during the LEP1 part of 1995, I was stationed at CERN. I was then responsible for the off-line analysis of the data. The 1994 and 1995 beam parameter analysis of Appendices A and C was performed by me, whereas the plots for 1993 beam parameters of Appendix A reflect an analysis performed by Sissi Rinaudo. The transport equations and the FASTSIM corrections are also her own work. The FASTSIM simulations were run by Sverker Almehed. A similar sharing holds for Appendix B. The data analysis was done by me, whereas FASTSIM runs were made by Sverker Almehed and the slope calculation was made by Sissi Rinaudo. The luminosity calculation was done with a program whose main author is Sissi Rinaudo.

Coming to the QCD analysis described in Chapter 4 and Appendix D, I wrote the small program which performed the smearing and I ran some of the simulations used in Section 4 of Appendix D, but the main ideas about the hadronization correction belong to Torbjörn Sjöstrand. On the other hand, the data analysis was done by me, mainly guided by Oxana Smirnova. Oxana Smirnova did part of the evaluation of the systematic errors herself. Moreover, the strong coupling constant evaluation was done by a program of her own.

I found my work in DELPHI a fascinating task. I finish this thesis with the hope that my work was a small, yet useful, contribution to the gigantic efforts of the DELPHI collaboration.

Lund, April 2001

Christina Zacharatou Jarlskog

CHAPTER 1

THE COLLIDER AND THE DETECTOR

The analysis presented in this thesis was performed on data collected by the DELPHI detector from 1992 to the first period of 1995. The DELPHI detector is one of the four detectors operating at the LEP storange ring, which is situated at the Swiss-French border near Geneva. In this Chapter, the LEP collider and the DELPHI detector are described.

1.1 LEP

The Large Electron Positron collider was the largest collider in the world with its 27 km circumference. It was a magnificent piece of machinery built in the 1980s, where especially the design of good RF cavities was a major challenge. The electron and positron beams were accelerated in opposite directions by the same set of magnets and in the same vacuum pipe. They were steered to collide at four points along the ring. Each interaction point was surrounded by a very big detector, which had the shape of a cylinder, the beam pipe being on the axis of the cylinder (Fig. 1.1). The four detectors were ALEPH, L3, OPAL and DELPHI .

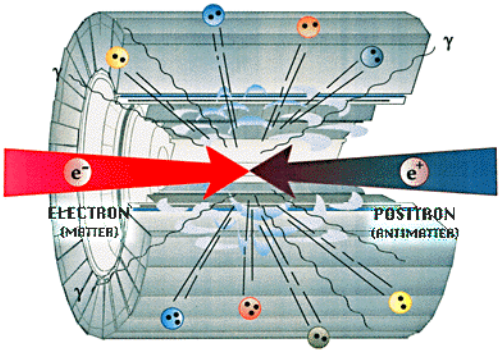

Figure 1.1. Electron and positron beams colliding in the center of one of the four LEP detectors.

The design studies of the LEP collider took place in 1976-1978. The plan behind the machine was to study the electroweak theory by first creating Z^0 particles at a center-of-mass energy of about 90 GeV and then increasing the energy to about 180 GeV to produce pairs of W particles. The collider had been operating at Z^0 energy from the beginning of its operation in 1989 until the first running period of 1995. In this time span, millions of Z^0 events have been recorded by the four detectors surrounding the ring. In the fall of 1995, the energy of LEP was increased, first to 130-140 GeV and then to 161-172 GeV in 1996. In 1997, the energy per beam

was 91-92 GeV, allowing the creation of Z^0 pairs. The physics run of 1998 took place at 189 GeV. A year followed with the energy climbing to 192-204 GeV. In 2000, the collider was operating at 200-208 GeV till the final run in November 2000, which marked the end of the operation of the gigantic machine.

For the accurate Z^0 lineshape measurements, it was necessary to measure the beam energy with very high precision, of the order 1 MeV. This was achieved by resonant depolarization [1], which allowed for some rather spectacular corrections of variations of the beam energy due to the tide effects from the position of the Sun and the Moon, the rain fall in the area and the departures of TGV trains from Geneva to Paris.

1.1.1 The tunnel and main ring

Apart from the four experimental caverns, the underground structure of the tunnel comprises 18 pits, 3 km of secondary tunnel and a large number of chambers and alcoves [2]. The plane of the tunnel is inclided by 1.4 % to insure solid rock support for the main part of the tunnel and the caverns. During the construction, the tunneling machines were guided with a precision of about 1 cm. The components of the collider were subsequently aligned with a relative precision of less than about 0.1 mm.

Figure 1.2. The LEP tunnel. A few magnets are visible on the picture.

The main ring was not an ideal circle. It was made of eight arcs and eight straight sections. The length of one straight section was 500 m approximately. Each arc was composed of 31 ‘standard cells’. A ‘standard cell’ contained the following sequence of magnets: a defocusing quadrupole, a vertical orbit corrector, six bending dipoles, a focusing sextupole, a focusing quadrupole, a horizontal orbit corrector, another six bending dipoles and a defocusing sextupole. The length of one standard cell was 79.11 m. About three quarters of the main ring were occupied by standard cells.

Apart from the magnets that directed the beam, the experiments had four large solenoidal magnets, which surrounded the four interaction points and were required to measure particle momenta. Moreover, in order to increase the interaction rate, magnets were needed to tightly focus the beam bunches before they met in the center of the detectors. This

was accomplished by a set of superconducting quadrupoles that focused the transverse beam dimensions to about 10 µm and 250 µm in the vertical and horizontal planes, respectively.

Maintaing a very low vacuum in the beam pipe was vital for the operation of the collider. A typical fill at LEP lasted for 12 hours. This time allowed the 10^{12} particles in the beams to fly around the ring about 500 million times. This could lead to particle losses due to collisions of the beam particles with residual gas molecules. To minimize the losses, the pressure in the vacuum chamber was reduced to $8{\cdot}10^{-12}$ Torr without beam and to 10^{-9} Torr approximately in the presence of beam. The rise in pressure was due to the synchrotron radiation of the beam, which induced gas desorption from the wall of the vacuum chamber.

The beams were accelerated by 128 RF cavities. Each cavity was coupled to a low-loss storage cavity so that the electromagnetic power continuously oscillated between the two sets of cavities and attained its peak value in the accelerating cavities when the beam bunches traversed them. The operating frequency was 352.21 MHz, corresponding to 31320 times the revolution frequency. This implied the same number of stable beam regions (RF buckets) along the ring. The beam bunches needed to be injected at the appropriate regions. This required a very precise synchronization between the RF systems of LEP and its injector, the SPS.

1.1.2 Injectors and pre-injectors

The electrons and positrons of LEP were accelerated by a series of injectors and pre-injectors before being engaged into the main ring (Fig. 1.3). First, there were two linear accelerators for the electron and positron beams (LIL). In the two linacs, the particles achieved energies of 200 MeV and 600 MeV. The beams were stored in the electron-positron accumulator before being injected into the proton synchrotron (PS). The PS accelerated both beams to 3.5 GeV. The next step was to bring the beams into the super proton synchrotron (SPS), where the energy of the electrons and positrons was increased to 20 GeV. The beams finally left the SPS to be injected into the main ring of LEP.

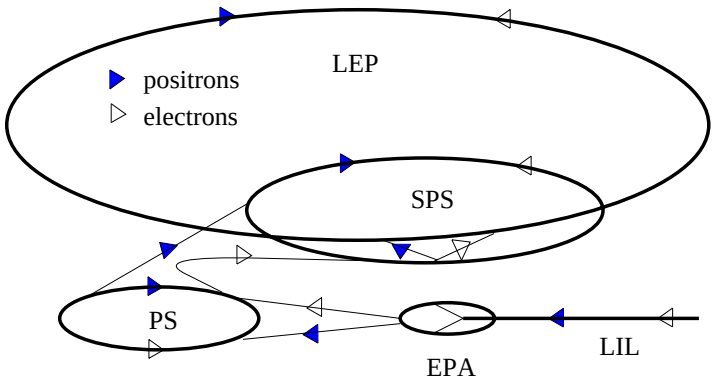

Figure 1.3. The injectors of LEP: linacs (LIL), electron-positron accumulator (EPA), proton synchrotron (PS) and super proton synchrotron (SPS).

1.2 The DELPHI detector

DELPHI stands for 'DEtector with Lepton, Photon and Hadron Identification'. It was a general purpose detector with its design particularly stressing particle identification and high granularity over a solid angle of 4π. The detector started operating in 1989. The detector ran every year usually from May to November. In this section, the detector is briefly described [3].

As was mentioned in Section 1.1, the DELPHI detector had a cylindrical shape. The concave part of this cylinder is called 'the barrel', whereas the two bases of the cylinder are called 'endcaps' or 'forward regions'. The barrel covered the polar angles between 40° and 140° approximately (Fig. 1.4).

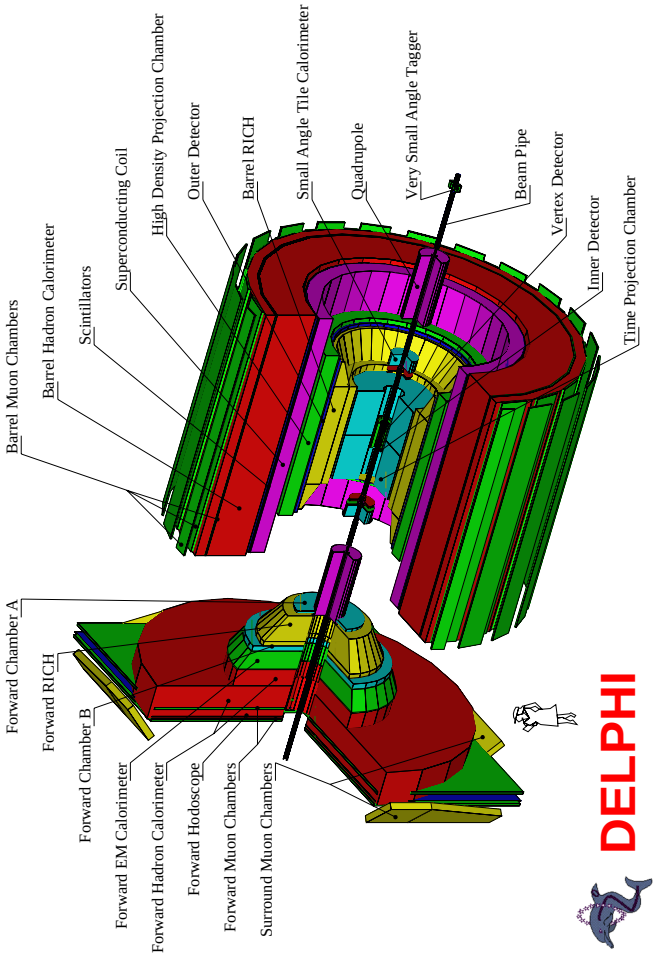

Figure 1.4. Schematic representation of the DELPHI detector showing the barrel and one endcap. The Forward Chamber A was attached to the TPC but is here shown as part of the endcap for clarity.

The standard coordinate system of DELPHI has the z axis in the direction of the electron beam. The x axis points towards the center of the LEP ring and the y axis points upwards. The polar angle to the z axis is denoted by θ (Fig. 1.5). The azimuthal angle in the xy plane is called ϕ. The radial coordinate in the xy plane is $R = (x^2 + y^2)^{1/2}$. Due to this definition of coordinates, the expression '$R\phi$-measurement' is often used to refer to measurements in the xy plane.

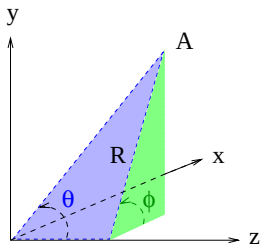

Figure 1.5. DELPHI coordinates for a particle at point A.

The innermost detectors were tracking devices, which measure the trace of particles. They were divided in two groups: (a) tracking detectors in the barrel and (b) tracking detectors in the endcaps. The first group comprised four detectors. As particles fly out from the interaction region, they met these four detectors in the following order: Vertex Detector (VD), Inner Detector (ID), Time Projection Chamber (TPC) and Outer Detector (OD). The second group of tracking detectors was made of the Forward Chambers. There were two Forward Chamber volumes in each endcap: the Forward Chambers A (FCA) and the Forward Chambers B (FCB). In total, there were thus six tracking detectors in DELPHI. All tracking devices were in a highly uniform magnetic field of 1.23 T. The field was parallel to the z axis. It was provided by a superconducting solenoid, as was mentioned in Section 1.1.1. The field made the particles bend in the xy-plane (Fig. 1.5).

Particle identification was provided by Ring Imaging CHerenkov detectors (RICH), which comprised one volume in the barrel (BRICH) and one volume in each endcap (FRICH). The BRICH and FRICH became fully operational in 1992 and 1994, respectively.

The outer detectors were calorimeters, i.e. absorption devices that measured the energy of the particles. DELPHI had four electromagnetic calorimeters. The barrel calorimeter was the High density Projection Chamber (HPC). The endcap calorimeter was the Forward ElectroMagnetic Calorimeter (FEMC), occuping one volume in each endcap.

The other two electromagnetic calorimeters were mainly used for luminosity measurements and were therefore placed close to the beam pipe. These were the Small Angle Tagger (SAT) and the Very Small Angle Tagger (VSAT). In April 1994, the Small angle TIle Calorimeter (STIC) replaced the Small Angle Tagger (SAT). Additional scintillators had been installed in the regions between the barrel and each endcap and in the gaps between the HPC modules to achieve complete hermiticity. The HAdron Calorimeter (HAC) was placed in the barrel on the iron yoke of the magnet.

Muon identification was achieved by three muon detectors: one in the barrel (Barrel Muon Chambers), one in the endcaps (Forward Muon Chambers, one volume in each endcap) and the Surrounding Muon Chambers (SMC).

1.2.1 The vertex detector

The VD was the closest detector to the beam pipe. It provided very precise tracking, principally in order to detect very short lived particles. It also contributed to the reconstruction of the primary vertex. It consisted of three coaxial cylindrical layers of silicon strip detectors at average radii of 6.3 cm (closer layer), 9 cm (inner layer) and 10.9 cm (outer layer) (Fig. 1.6).

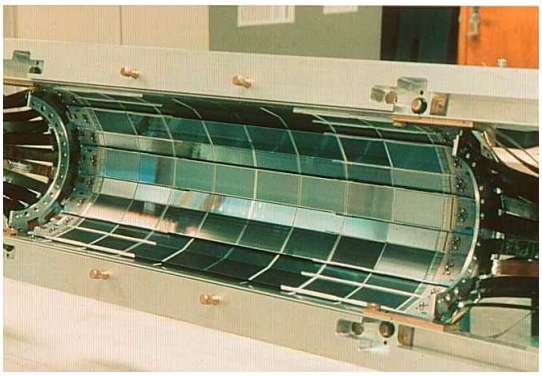

Figure 1.6. View of the inner layer of the vertex detector (12 sectors are shown).

Each layer was made of 24 sectors covering the full azimuthal angle. There was an overlapping between neighbouring sectors. Fig. 1.6 shows 12 sectors of the inner layer. Particles with polar angles between 44° and 136° crossed all three layers of VD. The readout pitch in the $R\phi$ plane was 50 μm. The detector was upgraded for the 1994 run by adding a second side of silicon detectors to the closer and outer layers. The second side had strips orthogonal to the strips of the preexisting side so as to measure the z coordinate of the track. The polar angle coverage of the closer layer was improved to 25°-155°. In the closer layer, the z coordinate readout pitch was 49.5 μm at polar angles near 90° and increased to 150 μm at smaller polar angle values. The corresponding values for the outer layer were 42 μm and 84 μm.

1.2.2 The inner detector

The ID was the second closest detector to the beam pipe after the VD. It had two components: the jet chamber, measuring position with a precision smaller than this of the VD, and the Trigger Layers (TL). The jet chamber extended between radii of 12 cm and 23 cm and covered polar angles between 15° and 165°. It was a drift chamber subdivided into 24 sectors of 15° (Fig. 1.7). Each sector could measure up to 24 points per track. A track with polar angle between 23° and 157° would cross at least 10 wires. The TL consisted of five coaxial cylindrical MWPC layers of 192 sense wires. The wires in neighbouring layers were displaced by half a cell. The cell width was 8 mm approximately. The TL polar angle coverage was 30°-150° up to 1994 data. In the beginning of 1995, this changed to 15°-165° and the minimum polar angle for crossing the 10 innermost wires of the jet chamber became 15°.

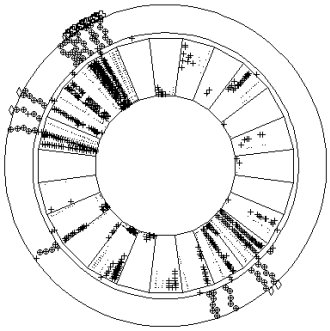

Figure 1.7. Schematic view of the ID. The 24 sectors of the jet drift chamber are seen with crosses representing track hits. The circled crosses denote hits in the TL tubes. They were combined with hits in the OD to be used for triggering.

In $R\phi$, the resolution of the ID was about 40 μm. In azimuthal angle, the resolution was 1.2 mrad approximately.

1.2.3 The time projection chamber

The TPC was the main tracking detector of DELPHI. It also contributed to charged particle identification by energy loss measurement. It consisted of two cylindrical drift volumes with a length of 130 cm each (Fig. 1.8). The drift volumes were separated by a high tension plate (20 kV) producing an electric field of 150 V / cm. The inner radius of TPC was 0.29 m and and the outer radius was 1.22 m. The active volume of the detector was between radii of 40 cm and 110 cm. The polar angle coverage was 39° -141° .

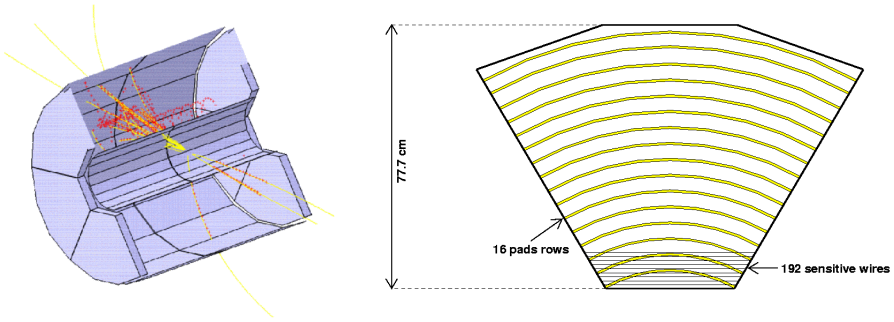

Figure 1.8. Left: view of the two drift chambers of the TPC, separated by a high tension plate in the middle. The three sectors of the endcap on the left are also shown. Right: one sector of the TPC. Each circle segment denotes a row of pads.

The drift volumes contained a gas mixture of 80% Ar and 20% CH_4. When a charged particle traversed a drift volume it ionized the gas and the electrons produced by the ionization drifted towards the endcaps of the TPC. Each endcap consisted of six proportional chambers called sectors (Fig. 1.8). Each sector had 16 rows of pads allowing the reconstruction of 16 points per track. Each row contained 105 pads. In front of the pads, there was an anode at 1430 volts containing 192 sense wires per sector. These wires were used for the energy loss measurement. Particles with polar angles between 20° and 160° produced signals in at least three pad rows. The precision of the position measurement was 150 μm in $R\phi$ and 600 μm in z, approximately.

1.2.4 The outer detector

The OD was the last tracking detector particles would cross in the barrel region of DELPHI (apart from muons, which would also reach the muon chambers). Like the other tracking devices discussed so far, the OD had the shape of a cylinder with the axis along the beam direction.

The inner and outer radii of the cylinder were 1.97 m and 2.06 m, respectively. It covered polar angles between 42° and 138°. The OD was divided in 24 azimuthal modules. Each module contained five layers of drift tubes. The layers were displaced with respect to each other. Each layer in a sector contained 32 columns of drift tubes.

When a particle crossed the OD, the drift distance for each tube was measured, giving in total five measurements in $R\phi$ (one for each layer). The precision of the $R\phi$ measurement was 110 μm. Moreover, the three internal layers provided measurements in z by calculating the time difference between the arrivals of the signals at the two ends of the anode wire. The precision of this measurement was 3.5 cm.

The measurements of OD and ID were combined for triggering.

1.2.5 The forward chambers

The tracking devices described above were all located in the barrel region. The endcap regions had two tracking detectors: the forward chamber A and the forward chamber B.

The FCA was located at about 1.6 m in $|z|$ from the DELPHI origin. It consisted of three modules attached to each of the TPC endcaps. A module was made of two planes of drift tubes. The planes were split into half-discs with an outer radius of 103 cm. The modules were rotated with respect to each other by 120°. The detector covered polar angles from 11° to 32° and from 148° to 169°.

The precision of the position measurements was 0.29 mm in x, 0.24 mm in y, 8.5 mrad in polar angle and 24 mrad in azimuthal angle. For trigger purposes, the FCA measurements were combined with the FCB measurements.

The FCB was a drift chamber located at 2.75 m in $|z|$ from the center of DELPHI. It surveyed polar angles between 11° and 36° and from 144° to 169°. It consisted of two modules (in each endcap). Each module had about 2000 wires divided into 12 planes, 4 for

each wire orientation, as shown in Fig. 1.9. The precision of the parameters of the reconstructed track segment was 0.15 mm in x and y, 3.5 mrad in polar angle and $4/\sin\theta$ mrad in azimuthal angle.

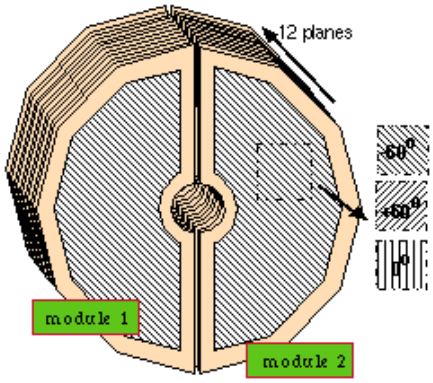

Figure 1.9. The two modules of FCB.

1.2.6 The barrel electromagnetic calorimeter

The HPC was located between the outer detector and the solenoid. It was a cylinder of 5.08 m in z, placed at radii between 2.08 m and 2.6 m. It consisted of 144 modules arranged in 6 rings. A module was similar to a TPC containing layers of lead wires in a gas volume. The lead wires functioned as converters but they also provided the drift field. The total converter thickness was $18\ X_0/\sin\theta$. Each module had 9 rows of 128 pads. In the first row (nearest to the interaction point), the pad width was 2 cm. In the last row, the pads were 8 cm wide.

Energy calibration and alignement were performed using $Z \rightarrow e^- e^+$ events. The resolution in z for 45 GeV electrons was 0.13 cm in the innermost rings (smallest $|z|$) and 0.31 cm in the outer rings. The resolution in polar angle was 0.6 mrad and in azimuthal angle was 3.1 mrad. The energy resolution for 45 GeV electrons was 6.5% approximately.

1.2.7 The forward electromagnetic calorimeter

The FEMC measured the energy of electromagnetically interacting particles by collecting the Cherenkov light (Section 1.2.10) emitted by the charged tracks of the shower which was produced when the particles crossed the lead glass modules of the calorimeter. The modules of FEMC had the form of truncated pyramids with inner face dimensions of $5.0^x5.0$ cm^2 and outer face dimensions of $5.6^x5.6$ cm^2. The depth of a module was 40 cm (20 radiation lengths). The modules pointed towards the center of DELPHI. There was one array of modules in each side of DELPHI. One array was made of 4532 modules. The front faces of the arrays were placed at $|z|$ = 284 cm. The FEMC covered polar angles from $8°$ to $35°$ and from $145°$ to $172°$.

Bhabha events ($e^-e^+ \rightarrow e^-e^+$) were used to calibrate 90% of the detector. In the region of $\theta > 32°$, the Bhabha electrons interacted with the TPC support structures and their energy was reduced. This region of the FEMC was calibrated with muons instead.

The energy resolution for Bhabha electrons was 4.8%. For neutral particles of energy larger than 2 GeV, the average precision on the reconstructed hit position in x and y projected to $|z| = 284$ cm was about 0.5 cm.

1.2.8 The luminometers

The absolute luminosity measurement was performed by the SAT and later by the STIC. The relative luminosity measurement has been performed by the VSAT.

The SAT consisted of two modules surrounding the beam pipe at $|z|=2.3$ m. Acceptance masks were installed in front of one module. Between the module and the masks, a two-plane silicon tracker was placed. The modules were made of alternating layers of lead sheets and plastic scintillating fibers aligned parallel to the beam. The polar angles covered were between 43 mrad and 135 mrad.

The STIC was a sampling lead-scintillator calorimeter. It had two cylindrical modules placed at $|z|=2.2$ m, covering polar angles from 29 mrad to 185 mrad. Each module was equipped with two planes of silicon strip detectors for the measurement of the direction of the shower. The energy resolution of STIC at 45 GeV was 3%.

The VSAT was also a sampling calorimeter. It consisted of four rectangular modules, two on either side of the interaction region, at $|z|=7.7$ m. Each module contained 12 tungsten absorbers of two radiation lengths each interspaced with 11 silicon planes for energy measurement, giving about 4% accuracy at 45 GeV. Three silicon strip planes measured the x (two planes) and y (one plane) coordinate of the shower maximum with a resolution of about 170 μm. The angular acceptance of the detector was 5-7 mrad in polar angle.

1.2.9 The hadron calorimeter

The HAC was made of a barrel section and two endcaps (Fig. 1.10). The barrel section consisted of 24 modules covering polar angles from 43° to 137°. Each endcap was made of 12 sectors. Apart from the hadronic energy measurement, the detector could also be used for distinguishing between hadrons and muons.

Each of the barrel modules was made of 20 layers of limited streamer mode detectors inserted into 2 cm slots between 5 cm iron plates. The modularity of endcaps was similar to the barrel with a sampling depth of 19 layers. The detectors were wire chambers consisting of a plastic cathode forming eight cells with one anode wire in each. The hadron calorimeter contained by far the largest volume of gas in DELPHI (Ar/CO2/i-butane at a proportion of 1/6/3). Dimuon events were used for the calibration. In the barrel region, the accuracy of the energy measurement was $\sigma(E)/E=(0.21^2+1.12^2/E)^{1/2}$.

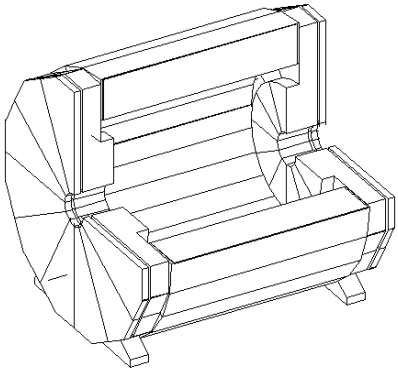

Figure 1.10. The hadron calorimeter of DELPHI.

1.2.10 The ring imaging Cherenkov detectors

The RICH detectors of DELPHI were used for particle identification. They made DELPHI have the best identification capacity of the LEP experiments.

The barrel RICH identified particles with momentum between 0.7 GeV and 45 GeV. The identification of the particles was performed as follows. When the velocity of a charged particle exceeded the velocity of light in a medium, electromagnetic radiation (Cherenkov light) was emitted by the atoms in the medium. The radiation formed a cone whose axis was the direction of the particle. The opening angle of the cone, θ, was given by the relation $\cos\theta=(\beta n)^{-1}$, where β is the velocity of the particle and n is the refractive index of the medium (radiator). Particles of different mass would cause Cherenkov radiation to be emitted after different momentum thresholds. Therefore, the momentum above which a particle could be seen by the RICH depended both on the mass of the particle and on the refractive index of the medium. The barrel RICH had two radiators: a liquid radiatior (C_6F_{14}) with n=1.2718 and a gas radiator (C_5F_{12}) with n=1.0019. The momentum thresholds (in GeV) for Cherenkov radiation emission from pions, kaons and protons are given in Table 1.1.

	pion	**kaon**	**proton**
liquid radiator	0.17	0.7	1.2
gas radiator	2.3	8.2	16.0

Table 1.1: Momentum thresholds in GeV for Cherenkov emission in the two radiators of the barrel RICH.

To identify particles, the detector used the momentum measured by the tracking system to calculate the expected Cherenkov angles (if the momentum is above threshold) for a given particle flavour and compare it with the measured angle. From the comparison, a possibility could be extracted for the particle to have a certain mass.

When a particle entered the RICH, it first traversed a 1 cm thick layer of liquid radiator and then a 40 cm thick layer of gas radiator. The emitted Cherenkov photons were detected in a common photon detector, where they were converted to photoelectrons. Mirrors were used to reflect the radiated photons in the gas radiator onto the photon detector.

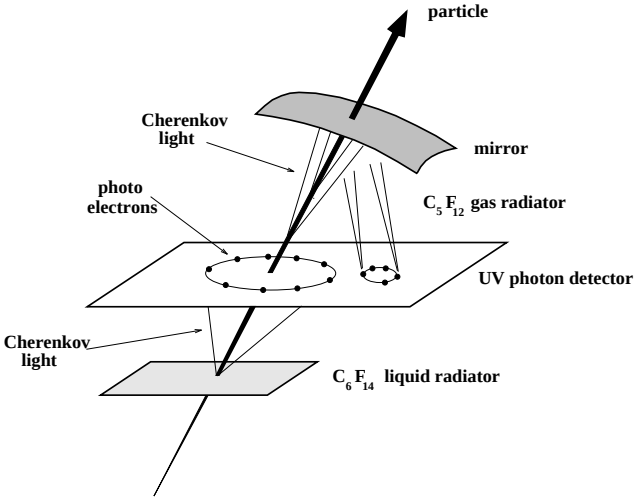

Figure 1.11. Cherenkov light emitted by a charged particle in the two radiators of the barrel RICH.

The forward RICH detectors operated in a similar way as the detectors in the barrel. The gas radiator was C4F10 (n=1.0015). The detector was located at $|z|$ between 1.7 m and 2.7 m. It covered polar angles from $15°$ to $35°$.

1.2.11 Momentum precision and alignment

The momentum precision of the tracking system of DELPHI was determined by measuring the momenta of muons in $Z \rightarrow \mu^-\mu^+$ events in which the acollinearity of the muons was less than $0.15°$. The reconstructed muon tracks were required to contain information from all tracking detectors in the barrel: VD, ID, TPC and OD. It was found that the momentum precision in the barrel region was $0.57 \cdot 10^{-3}$ GeV^{-1}. The momentum precision in the forward region was determined by using muon tracks which had been reconstructed by the FCB and had traversed at least the closer layer of the VD. A gaussian fit gave a precision of $1.31 \cdot 10^{-3}$ GeV^{-1}.

The alignment of the tracking detectors was performed also using $Z \rightarrow \mu^-\mu^+$ events. To align the detectors in the barrel region, the OD was used as reference. Then the position of the VD, with respect to the OD, was determined assuming the two muons are collinear. The tracks formed by the OD and VD were subsequently used as reference in order to align the ID and the TPC. The forward chambers, FCA and FCB, were aligned by extrapolating to the forward region the muon tracks that had been reconstructed by the TPC. The tracking system having been aligned, the dimuon tracks were extrapolated to align the HPC and the RICH.

CHAPTER 2

LUMINOSITY FOR Z LINESHAPE STUDIES

2.1 Introduction

The mass of the Z^0 is one of the fundamental parameters in the Standard Model. The DELPHI experiment has been performing high precision measurements of its value in what is usually referred to as 'lineshape studies'. This means that the energy was varied over the Z^0 peak and the cross sections were measured at each energy point. Lineshape studies include consistency checks of the predictions of the Standard Model and investigations for new physics. This chapter attempts to present an overview of these studies and to illustrate how the VSAT luminosity has been contributing to them.

As already mentioned, lineshape analyses require scan data, i.e. data taken at different energy points around the Z^0 pole. During LEP1, scans have taken place in 1989, 1990, 1991, 1993 and 1995. In 1992 and 1994, the machine was running only on top of the Z^0. Nevertheless, 1992 and 1994 measurements were also included in the lineshape analyses. The observables used in these analyses were the hadronic cross sections, the leptonic cross sections and the leptonic forward-backward asymmetries. In order for the cross sections to be calculated, a luminosity measurement was required. Given the collected statistics (of the order 10^6 for hadronic events), the luminosity error should be of the order 0.1%.

Section 2.2 explains how the luminosity is used for the extraction of the mass and width of the Z^0, i.e. in the hadronic cross section calculation. Section 2.3 describes how the Z^0 parameters are extracted once the hadronic cross sections have been calculated.

2.2 The use of the luminosity

DELPHI has been measuring the luminosity, L, by recording the rate of Bhabha events in the very forward region, R, and dividing by the accepted cross section, σ, of this process, $L=R/\sigma$. In the first years of operation of the detector, the absolute luminosity was measured by the SAT luminometer, which had a significant systematic error. In order to improve the luminosity error, the VSAT detector was designed to provide a high precision relative (to the SAT) luminosity measurement for the off-peak energy points. The VSAT luminosity, being a relative measurement, was almost free of systematic uncertainties and was mainly limited by statistics. To insure a high Bhabha rate, the VSAT was placed very close to the beam pipe, as described in chapter 1, to profit from a visible cross section of 500 nb (approximately 20 times the cross section seen by the SAT). Moreover, at the angular region of the VSAT, the electroweak interference can be neglected and therefore the lineshape parameters calculated using VSAT luminosity are not affected by corrections for the energy dependence of the interference contribution. In 1994, the STIC luminometer replaced the SAT.

The STIC gave an absolute luminosity measurement with an error that could almost compete with the relative accuracy of the VSAT. The luminosity analysis of the VSAT (for the 1995 scan) has been presented in detail in [4] and also in Appendices A-C and therefore no further account will be given in this chapter.

In the analysis of 1989 data [5], the acceptance of the SAT was defined by a lead mask and two cuts, one on the azimuthal and one on the radial coordinate of the shower. Because of uncertainties in the internal geometry of the detector, these cuts introduced a systematic error on the luminosity measurement equal to 1%. Furthermore, the background subtraction implied a luminosity systematic error of 0.5% and 1.5% for the two samples collected (corresponding to a maximum outer radius of the lead mask equal to 12 cm and 13 cm). The SAT used two triggers for selecting Bhabha events, each being based on a different energy cut. The systematic error on the luminosity due to these energy cuts was estimated to be 1%. As the visible cross section was sensitive to variations of the z-coordinate of the interaction point, it was corrected for these variations. The correction depended on the position of the lead mask with respect to the interaction region, which was uncertain by 5 mm. This resulted in a systematic error of 0.5% for the luminosity. Additionally, a 0.6% systematic error was considered for trigger efficiency. The theoretical uncertainty for the cross section calculation gave a systematic error of 1%. Monte Carlo modeling and statictics added systematic uncertainties of 1% and 0.6%, respectively. The overall systematic error for the total SAT sample was thus 2.4%. The hadronic cross section, $\sigma_h(s)$, at each energy point, $E=\sqrt{s}$, was calculated was follows:

$$\sigma_h(s) = \frac{N_h - N_b}{\varepsilon L} \qquad (2.1)$$

where N_h is the number of hadronic events, N_b is the number of background events, ε is the efficiency for the hadronic event selection and L is the time integrated luminosity. The systematic error of the SAT luminosity (2.4%) was the main component of the normalization uncertainty of the cross sections (2.6%). (Lineshape results are shown in Table 2.1.)

In the 1990 run [6], the SAT had a new ϕ-mask, covering $\pm 15^o$ around the vertical junction region between the two half modules. The position of the lead mask with respect to the interaction region was measured with a precision of 1 mm, reducing the related systematic error on the luminosity to 0.13%. Due to a precise survey of the internal geometry of the detector, the systematic error due to the ϕ-cut in the event selection was reduced to 0.4%. Other improvements included a better evaluation of the trigger efficiency, a better detector simulation and higher statistics of simulated events. The result was a reduction of the total systematic error for the SAT luminosity to 0.9%. For the calculation of the hadronic cross sections, a new factor was introduced in eq. 2.1, taking into account the energy spread of the beams. The normalization uncertainty for the cross sections was 1.1%.

In 1991, the collaboration used the VSAT luminosity measurement for the first time in the lineshape studies. The total systematic uncertainty of the SAT measurement was 0.6% whereas the total systematic error for the (relative) VSAT measurement was 0.09% at the off-peak energy points [6]. From this error, 0.07% was the uncorrelated error [3] and 0.06% was the correlated error.

During the data taking of 1992, the machine was operating on the Z pole. The luminosity measurement was given by the SAT. The total error on the luminosity was 0.46%. The VSAT measurement was used only as a cross-check of the SAT luminosity.

In 1993, LEP was operating at three energy points close to the Z^0 pole. The total systematic error of the SAT luminosity was 0.29% [7]. In the same year, the VSAT luminosity was used for the off-peak energy points. The improvement of the VSAT analysis was threefold. First, high statistics extensive simulations were performed in order to correct the accepted cross section for its dependence on beam parameters. Moreover, a better determination of the alignment of the detector with respect to the beam pipe was achieved. Lastly, a restricted fiducial volume was introduced in the offline event selection. The uncorrelated error of the VSAT luminosity was reduced to 0.02%, whereas the correlated systematic error was 0.06%. The correlated error was added to the statistical error of the VSAT on peak (0.05%). Those errors gave the VSAT normalization error relative to the SAT luminosity. The uncorrelated errors were added quadratically to the statistical errors at each energy point.

In 1994, the collider was running on the Z^0 pole. The absolute luminosity measurement was performed by the STIC. In comparison to the SAT, the STIC had the following advantages: a better energy resolution, which allowed for a better background subtraction, a better knowledge of the internal geometry and a good spatial resolution, which gave a very accurate determination of the acceptance of the detector. The total experimental systematic error for the STIC luminosity was 0.09%, both for 1994 and for 1995. The theoretical error was 0.11%. As was the case in 1992, the measurement of the luminosity by the VSAT was used as a cross-check of the absolute luminosity measurement.

In 1995, a new scan took place. Data were taken at three energy points. The VSAT lost a considerable fraction of the statistics at the beginning of the year due to a new mode of minibunch operation, thus not being able to provide a luminosity for all the runs of this period although still maintaining its error at the 0.1% level. As the STIC luminosity error was also very low, the collaboration used the VSAT measurement only as a cross-check of the STIC luminosity. The two measurements agreed with each other, as is shown in Appendix B. The 1995 beam parameter analysis is summarized in Appendix C, whereas results from 1994 and 1993 are given in Appendix A.

2.3 Lineshape analysis

In order to extract the mass and width of the Z^0, the hadronic cross sections (eq. 2.1) are fitted by theoretical expressions. To exemplify the lineshape analysis, a short description is given below of the extraction of these parameters from the data of the first scan in 1989 [5].

The cross section was given as the sum of the pure continuum cross section, $\sigma_\gamma(s)$, and the cross section for the Z^0 exchange and interference terms. The latter term was given by the expression:

$$\sigma_Z(s) = 12\pi \frac{\Gamma_e \Gamma_h}{(s - M_Z^2)^2 + (s^2/M_Z^2)\Gamma_Z^2} \left[\left(\frac{s}{M_Z^2} + R \frac{s - M_Z^2}{M_Z^2} \right) F - (2 + R) G \right] \qquad (2.2)$$

where Γ_e and Γ_h are the electron and hadron partial widths and M_Z and Γ_Z are the mass and the full width of the Z^0. R is a function due to the γ–Z interference. It takes values in the interval 0.07-0.12, depending on the mass of the top quark and the mass of the Higgs

(assumed to equal to 130 GeV and 100 GeV, respectively, in 1989). The radiative corrections are incorporated in the functions F and G.

Three fits were performed to the hadronic cross sections. In the least model dependent fit, the free parameters were Γ_Z, M_Z and $\Gamma_e\Gamma_h$. This choice resulted in a determination of Γ_Z, which was not affected by the normalization error of 2.6%. In the second fit, the value of $\Gamma_e\Gamma_h$ was fixed to 0.146 GeV^2, i.e. to the prediction of the Standard Model. The partial widths from the Standard Model were combined with the new value of the full width to extract the value of the invisible width, Γ_{inv}, i.e. the partial width for channels with no charged particles in the final state, which are assumed to be the neutrino channels, and the number of light neutrino species thereafter (Table 2.1). Lastly, a third fit was performed where all parameters were taken from the Standard Model. An overall normalization factor was also left as a free parameter. The quality of the third fit exhibited a good agreement between the data and the Standard Model. From the extracted value of M_Z, the hadronic cross sections were calculated, assuming two and four neutrinos. The data clearly favoured three light neutrinos. Another determination of the number of neutrinos was made, using the results of the first fit and the ratio of the flavour averaged leptonic to hadronic widths, as was obtained in [8]. This measurement was not affected by the uncertainty coming from the top mass. It confirmed the results of the second fit. The Z^0 mass and width from the 1989 analysis are given in Table 2.1.

year	M_Z (GeV)	Γ_Z (GeV)	N_ν
1989	91.171 ± 0.030 (stat.) ± 0.030 (beam)	2.511 ± 0.065	2.97± 0.12± 0.23
1989-1990	91.177 ± 0.022	2.465 ± 0.020	2.94 ± 0.10
1990-1991	91.186 ± 0.009	2.484 ± 0.012	3.07 ± 0.05
1990-1992	91.187 ± 0.009	2.483 ± 0.012	3.060 ± 0.041
1990-1995	91.1864 ± 0.0028	2.4876 ± 0.0041	2.984 ± 0.017
ADLO	91.1875 ± 0.0021	2.4952 ± 0.0023	2.9841 ± 0.0083

Table 2.1: Mass and width of the Z^0 resonance and number of light neutrino species from DELPHI data. The error quoted as 'beam' refers to the uncertainty in the center of mass energies.

The 1989 analysis was performed on 11000 hadronic events. After the 1990 run, the analysis was repeated for the full statistics, namely 125000 hadronic events [6]. Apart from the increase in statistics, the new analysis benefited from a lower error on the luminosity, as already mentioned in Section 2.2. Instead of eq. 2.2, a program called ZFITTER was used to perform fits to the data, containing formulae for electroweak corrections to the Born cross section. The program included theoretical expressions for the hadronic and leptonic cross sections and for the leptonic asymmetries. A combined fit was performed to all measurements (except the endcap $e^+e^- \rightarrow e^+e^-$ cross sections). A separate fit to the hadronic lineshape was also performed, in the same way as the first fit in the 1989 analysis described above. The combined fits are described in detail in [6]. The mass and width of the resonance are given in Table 2.1. In 1989 and 1990, seventeen energy points around the Z pole were covered.

A new lineshape analysis followed [9] for 450000 hadronic and leptonic events collected in 1990 and 1991. Eight energy points were scanned in 1991. The contribution of the VSAT measurement reduced the statistical error of the Z^0 mass and width by 20% approximately [10]. The observed cross sections and asymmetries were fitted in a nine-parameter fit. The extracted values for the mass and width of the Z^0 are given in Table 2.1.

During 1992, 696500 hadronic events were collected on peak [11]. A new nine-parameter fit was performed combining data from 1990, 1991 and 1992. The mass and width of the resonance were essentially the same as in the previous analysis.

A new evaluation of the lineshape parameters was presented in [7]. It included all data from 1990 to 1995. The nine-parameter fit results for M_Z and Γ_Z are shown in Table 2.1. The five-parameter fit results are shown in Fig. 2.1.

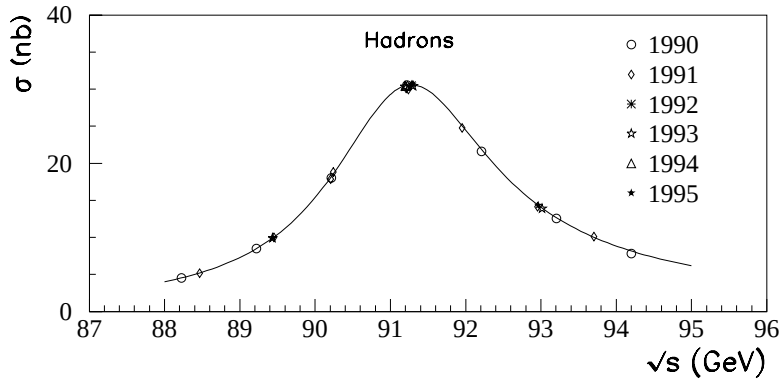

Figure 2.1. DELPHI hadronic cross sections (1990-1995). The curve shows the result of the five-parameter fit [7].

The combined results from the four LEP experiments are reported in [12]. The number of hadronic events used in this combination is shown in Table 2.2. The Z^0 mass and width are given in the last row of Table 2.1.

year	ALEPH	DELPHI	L3	OPAL	All
1990-1991	433	357	416	454	1660
1992	633	697	678	733	2741
1993	630	682	646	649	2607
1994	1640	1310	1359	1601	5910
1995	735	659	526	659	2579
total	**4071**	**3705**	**3625**	**4096**	**15497**

Table 2.2: Number of hadronic events (divided by 10^3) per year and per experiment, used in the combined lineshape analysis [12].

2.4 Summary

The electroweak parameters discussed in the previous sections play a crucial role in the quest for new phenomena beyond the Standard Model. DELPHI has been striving for the highest accuracy possible in the determination of these parameters, as new physics could manifest itself in small deviations from the values predicted by the Standard Model. All scan data agreed with the Standard Model. The invisible and total widths were used to set lower limits for the masses of new particles, as is shown, e.g., in [6].

The VSAT measurement improved significantly the error of the mass and width of the Z^0 by contributing with a relative luminosity determination in 1991 and 1993. In 1992, 1994 and 1995, the VSAT measurement was used to provide confidence to the scan results.

CHAPTER 3

QCD

3.1 Introduction

The field theory of strong interactions, Quantum Chromodynamics (QCD), does not allow for accurate calculations at low energy but can be solved pertubatively at the asymptotic limit, i.e. the strong coupling constant α_s is small enough for the theory to be calculable only at very small distances (large energies) but the theory cannot describe the hadronization process that brings us from partons to the observale hadrons. The properties of the hadronization, or fragmentation, process can only be extracted from experimental measurements, e.g. in terms of fragmentation functions, and be described by phenomenological models.

The study presented in the next chapter deals with the extraction of the transverse and longitudinal helicity components of the fragmentation function, which receive their major contributions from the fragmentation of quarks and gluons, respectively. As the theoretical input available is at perturbative level, emphasis has been put on the removal from the measurement of non-perturbative contributions.

3.2 Hadron production in e^+e^- annihilation

Electron-positron annihilation is a favoured process for the study of fragmentation functions. The colliding leptons are structureless objects, giving a well-defined initial state, where no additional non-perturbative input is needed, as the case would be, e.g., for a proton beam, requiring the knowledge of parton density functions. Moreover, there are no beam remnants in the final state, again in contrast to a ep or $p\bar{p}$ experiment, which reduces the difficulty of event selection.

The hadron production in electron-positron annihilation can be viewed as taking place in two steps: (a) a perturbative part, including the hard process and the shower development and (b) a non-perturbative part, including the hadronization process and the decay of short-lived particles (Fig. 3.1).

In the Standard Model, the cross-section for the hard process, i.e. the production of the primary $q\bar{q}$ pair at an angle θ with respect to the beam direction is given by (see e.g. [13]):

$$\frac{d\sigma}{d\cos\theta} = \sigma_{q\bar{q}}\frac{3}{8}\left(1 + \frac{8}{3}A_{FB}\cos\theta + \cos^2\theta\right) \qquad (3.1)$$

The forward-backward asymmetry term (A_{FB}) is due to the γ-Z interference and is small at LEP1 energies. In this work, no effort was made to distinguish between the quark and antiquark, so the asymmetry term in Eq. 3.1 is not visible to the analysis.

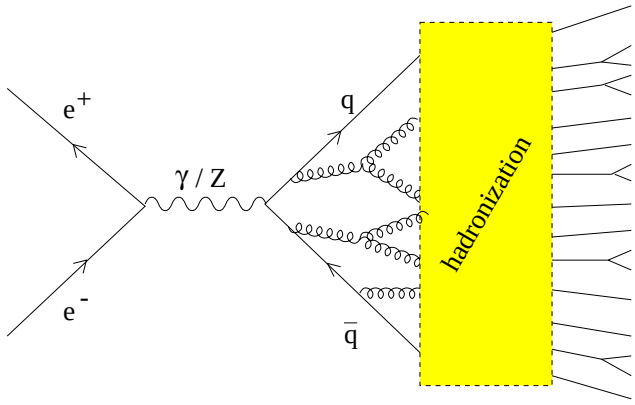

Figure 3.1. Development of the hadroproduction at electron-positron annihilation.

Neglecting the annihilation into a photon, the total cross-section for $q\bar{q}$ production at $E_{cm}=M_Z$ is

$$\sigma_{q\bar{q}} = \frac{12\pi\Gamma_{ee}\Gamma_{q\bar{q}}}{M_Z^2\Gamma_Z^2} \qquad (3.2)$$

where Γ_{ee} and $\Gamma_{q\bar{q}}$ are the partial widths for the decay of the Z into e^+e^- and $q\bar{q}$, respectively and Γ_Z is the total width for the decay of the Z.

At this point, perturbative QCD [14] can be invoked to derive cross-sections for more complicated configurations. This is done at two levels: (a) matrix elements are calculated [15] for a sufficiently low number of partons, i.e. $q\bar{q}g$, $q\bar{q}gg$ or $q\bar{q}q\bar{q}$, (b) parton showers are used to describe the emission of partons at higher orders. In the parton shower picture, the evolution of the state proceeds by means of three splittings: $q \rightarrow qg$, $g \rightarrow gg$ and $g \rightarrow q\bar{q}$. Each parton is characterized by a virtuality scale, Q^2, which, in a sense, also gives the time scale of the process: the virtuality scale decreases as we move forward in time, i.e. from the hard process towards the final state that we observe in the detector. The shower stops developing when a cut-off value, Q_0, is reached (around 1 GeV). Beyond this point in time, perturbative QCD cannot be used anymore because α_s becomes too large (Section 3.3). This is when the non-perturbative part of the process, i.e. fragmentation, begins.

A number of phenomenological models have been developed to account for the fragmentation process. These models are implemented as event generators based on Monte Carlo techniques. The generators follow the same route as outlined above for the production of the event, i.e. they use matrix elements or partons showers first but then they follow different models for the fragmentation process, such as the Lund string model [16], which is implemented in the JETSET generator [17] and which is used in the present analysis.

Returning to the perturbative part of the hadron production in electron-positron annihilation, the observed hadron is characterized by its emission angle, θ, with respect to the beam axis and the scaling variable

$$x = \frac{2p_h \cdot q}{q^2} \tag{3.3}$$

where p_h and q are the four-momenta of the produced hadron and the propagator, respectively. In perturbative QCD calculations, the hadrons are assumed to be massless and the scaling variable is equal to the energy fraction carried by the hadron. In the measurement, however, the scaling variable is taken as being the momentum of the hadron divided by the beam energy (refer to as x_p in the next chapter). The double differential cross-section for the hadroproduction process, $e^+e^- \rightarrow hX$, where a hadron, h, has been measured in the final state, can be written as [18]

$$\frac{d^2\sigma}{dx d\cos\theta} = \frac{3}{8}(1+\cos^2\theta)\frac{d\sigma_T}{dx} + \frac{3}{4}\sin^2\theta\frac{d\sigma_L}{dx} + \frac{3}{4}\cos\theta\frac{d\sigma_A}{dx} \tag{3.4}$$

where T and L denote the contributions from transverse and longitudinal polarization states of the Z with respect to the $q\bar{q}$ axis, respectively, θ is the polar angle of the hadron with respect to the beam axis and A denotes the forward-backward asymmetry term, which, as pointed out above, cannot be observed in the present analysis.

The transverse and longitudinal components of the fragmentation function are defined by normalizing the corresponding cross sections to the total cross section, $\sigma_{tot} = \sigma_T + \sigma_L$:

$$F_T = \frac{1}{\sigma_{tot}}\frac{d\sigma_T}{dx}, \qquad F_L = \frac{1}{\sigma_{tot}}\frac{d\sigma_L}{dx} \tag{3.5}$$

Their extraction from LEP1 data (1992-1995) is presented in the following Chapter.

3.3 The strong coupling constant

QCD suffers from ultraviolet divergencies which are introduced by virtual corrections to the gluon propagator. Renormalization takes care of the divergencies but leads to a dependence of the coupling constant, α_s, on the renormalization scale, μ^2:

$$\mu^2\frac{\partial\alpha_s}{\partial\mu^2} = \beta(\alpha_s) = -b_0\alpha_s^2 + b_1\alpha_s^3 + O(\alpha_s^4) \tag{3.6}$$

where

$$b_0 = \frac{11C_A - 2n_f}{12\pi}, \qquad b_1 = \frac{17C_A^2 - 5C_An_f - 3C_Fn_f}{24\pi^2} \tag{3.7}$$

n_f is the number of active flavours and C_A and C_F are colour factors. Since $n_f < 33/2$, the beta function, $\beta(\alpha_s)$, is negative. This has as a result that α_s decreases as the scale increases (asymptotic freedom).

Eq. 3.6 can be used to relate α_s values at two different scales:

$$\alpha_s(Q^2) = \frac{\alpha_s(\mu^2)}{w}\left(1-\frac{b_1}{b_0}\frac{\alpha_s(\mu^2)}{w}\ln w\right) \tag{3.8}$$

where

$$w = 1 - b_0\alpha_s(\mu^2)\ln\frac{\mu^2}{Q^2} \tag{3.9}$$

From the measurement of σ_L, it is possible to extract the strong coupling constant. In next-to-leading order of perturbative QCD, this measurement can be extracted as follows [19]:

$$\frac{\sigma_L}{\sigma_{tot}} = \frac{\alpha_s}{\pi} + \frac{\alpha_s^2}{\pi^2}(13.583 - n_f 1.028) \tag{3.10}$$

This equation assumes that all final state particles have been measured, both charged and neutral. As in the present analysis only charged particles are taken into account, the measured σ_L has to be corrected for the missing information. This is done with the help of the tuned simulation, as will be explained in the following chapter.

3.4 The tuned generator

As all simulated data for the LEP1 analyses at DELPHI were produced by JETSET 7.3, the present section gives the parameters of the generator's LEP1 tuning and a comparison between the tuned program and its default version.

By tuning is generally meant the determination of a set of parameters of the fragmentation model for which the latter provides an optimal description of a number of observables [20]. In the case in question, these measures were (a) the hadronic event shapes and (b) the charge particle inclusive distributions measured by DELPHI and (c) information on identified particles from all LEP experiments. The tuning was realized on 1991 and 1992 data. The resulting JETSET 7.3 parameters [17], which were used in the LEP1 production [21], are given in Table 3.1 and Table 3.2.

index	tuned value	default value
11	3	1
12	3	2
22	2	1
41	2	1
46	3	0

Table 3.1: Tuned and default MSTJ parameters for JETSET 7.3.

index	tuned value	default value
51	2	0
52	7	3
110	2	1

Table 3.1: Tuned and default MSTJ parameters for JETSET 7.3.

index	tuned value	default value
2	0.28	0.3
3	0.55	0.4
4	0.07	0.05
19	0.5	1
21	0.428 GeV	0.35 GeV
25	0.7	1
26	0.2	1
41	0.354	0.5
42	0.523 GeV^{-2}	0.9 GeV^{-2}
54	-0.030476	-0.06
55	-0.002326	-0.006
81	0.346 GeV	0.4 GeV
82	2.25 GeV	1 GeV
93	0.394 GeV	0.2 GeV
123	91.187 GeV	91.2 GeV
124	2.489 GeV	2.4 GeV

Table 3.2: Tuned and default PARJ parameters for JETSET 7.3

In addition, the parameter PARJ(107) was set to 4, selecting a DELPHI routine for initial state radiation (switched off by default). The properties affected by these parameters are described below (as taken from the JETSET manual [17]):

- MSTJ(11) selects the longitudinal fragmentation function, which determines the fraction of the available energy a new hadron will take.

The default value applies the Lund symmetric fragmentation function for all flavours. The tuned value chooses the hybrid scheme, i.e. light flavours fragment according to the Lund symmetric fragmentation function (PARJ(41)-PARJ(45)) whereas charm and heavier are treated separately (PARJ(51)-PARJ(59), PARJ(46)-PARJ(48)).

- MSTJ(12) selects the model for baryon production. The default setting allows for diquark-antidiquark pair production where the diquark can be split according the the 'popcorn' scheme. In the tuned version, the first rank baryons are suppressed by a factor PARJ(19).
- MSTJ(22) is the cut-off on decay length for a particle that can in principle decay. The default value forces particles to decay when declared unstable. In the tuned program, the particle decays only if its average invariant lifetime is larger than PARJ(71).
- MSTJ(41) determines the branchings that can occur in the shower. The default is to have QCD type branchings of quarks and gluons. The tuned value also permits photons to be emitted from quarks and leptons.
- MSTJ(46) decides whether the azimuthal distributions in a shower branching are homogeneous (default) or not. In the tuned option, the azimuthal angle in gluon decays is not homogeneous.
- MSTJ(51) selects Bose-Einstein effects (absent by default).
- MSTJ(52) gives the number of particles species for which Bose-Einstein correlations are requested. By default, all pions are included. The tuned value included also the kaons (K^+, K^-, K^0_S, K^0_L).
- MSTJ(110) determines the choice of second-order contributions to the 3-jet rate. The default value selects the GKS second-order matrix elements. The tuned value ressorts to the Zhu parametrization of the ERT matrix elements.
- PARJ(2) is the suppression of s quark pair production compared to u or d pair production.
- PARJ(3) is the extra suppression of strange diquark production compared to the normal suppression of strange quarks.
- PARJ(4) is the suppression of spin 1 diquarks compared to spin 0 ones (excluding the factor 3 coming from spin counting).
- PARJ(19) is the extra baryon suppression factor, which multiplies the ordinary diquark-antidiquark production probability for the breakup closest to the endpoint of a string but leaves other breakups unaffected.
- PARJ(21) is the width σ of the Gaussian p_x and p_y transverse momentum distributions for primary hadrons.
- PARJ(25) (PARJ(26)) is an extra suppression factor for η (η') production in the fragmentation. When an η (η') is rejected, a new flavour pair is generated and a new hadron is formed.

- PARJ(41), PARJ(42) give the parameters a and b of the symmetric Lund fragmentation function.
- PARJ(54), PARJ(55) select the parametrization of the fragmentation function for c and b quarks, respectively. For the tuned values, the SLAC parametrization is selected.
- PARJ(81) is the Λ value used in running α_s for parton showers.
- PARJ(82) is the invariant mass cut-off m_{min} of parton showers, below which partons are not assume to radiate.
- PARJ(93) gives the size of the Bose-Einstein effect region.
- PARJ(123), PARJ(124) give the mass and width, respectively, of the Z^0.

A comparison was made of the tuned and default generator, in order to assess the impact of the tuning on the main parameters of the analysis presented in Chapter 4. In order to compare the tuned program to the default version, nine groups of parameters/code modifications were considered, affecting:

- the Bose-Einstein correlations (MSTJ(51), MSTJ(52), PARJ(92), PARJ(93)),
- the η, η' suppression (PARJ(25), PARJ(26)),
- the flavour composition of the particles (PARJ(2), PARJ(3), PARJ(4), PARJ(19)),
- the fragmentation functions (MSTJ(11), PARJ(41), PARJ(42), PARJ(54), PARJ(55)),
- the stability of the particles K_S^0, Λ, Σ^-, Σ^+, Ξ^-, Ξ^0 and Ω^- (MSTJ(22)),
- the parton shower development (MSTJ(41), MSTJ(46), PARJ(81), PARJ(82)),
- the width of the transverse momentum distribution (PARJ(21)),
- the decay tables (DELPHI routine FILCST),
- the spin properties (changes in the routine LUKFDI).

The function of the above parameters (routines) in the DELPHI tuned program was investigated as follows. Each of the seven first sets of parameters above were set to their default values giving seven versions of the program (called ‘modified tuned’ here). There were two additional versions created by disregarding the routine FILCST in the first case and by disabling the changes in LUKFDI in the second case. In total, this procedure gave nine ‘modified tuned’ programs, which were run to produce one million events. Moreover, a modified version of the tuned program was obtained by disregarding all nine changes above. For each of the above ten modified versions of the tuned program, the distributions of the track momentum and of the track cosine of polar angle have been compared with the corresponding distributions obtained from the tuned program by subtracting the two and dividing by the tuned distribution. The ten relative differences are shown in the plots (a) - (j) of Fig. 3.2 and Fig. 3.3. The relative difference between the tuned and the default generator is shown in plot (k) of the same figures.

Fig. 3.2 shows that the shower development parameters constitute the main source of ‘disagreement’ between the two versions of the program, giving differences up to 70% for high momentum particles. The next most significant differences are due to the fragmentation function and transverse momentum width properties. All three properties are crucial to the analysis discussed in Chapter 4. The cosθ distributions are not affected as strongly as the momentum distributions by the tuning.

In the following, only the tuned version of JETSET 7.3 is used.

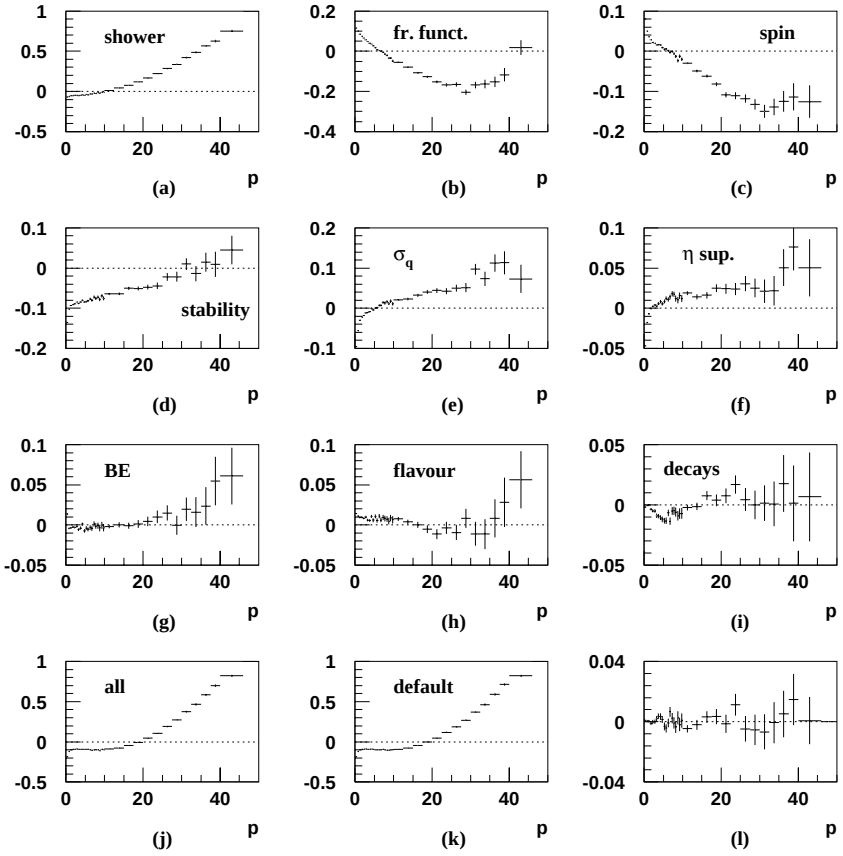

Figure 3.2. Relative (to the tuned) difference tuned minus modified tuned track momentum distributions when the following parameters / properties have been set to default: (a) parton shower development, (b) fragmentation functions, (c) spin, (d) stability of K^0_S, Λ, Σ^-, Σ^+, Ξ^-, Ξ^0, Ω^-, (e) width of transverse momentum, (f) η, η' suppression, (g) Bose-Einstein effects, (h) flavour content and (i) decay tables. The relative difference for all nine modifications of the tuned program is shown in (j). The difference tuned minus default momentum is shown in (k). The relative (to the tuned) difference between the last two distributions is given in (l).

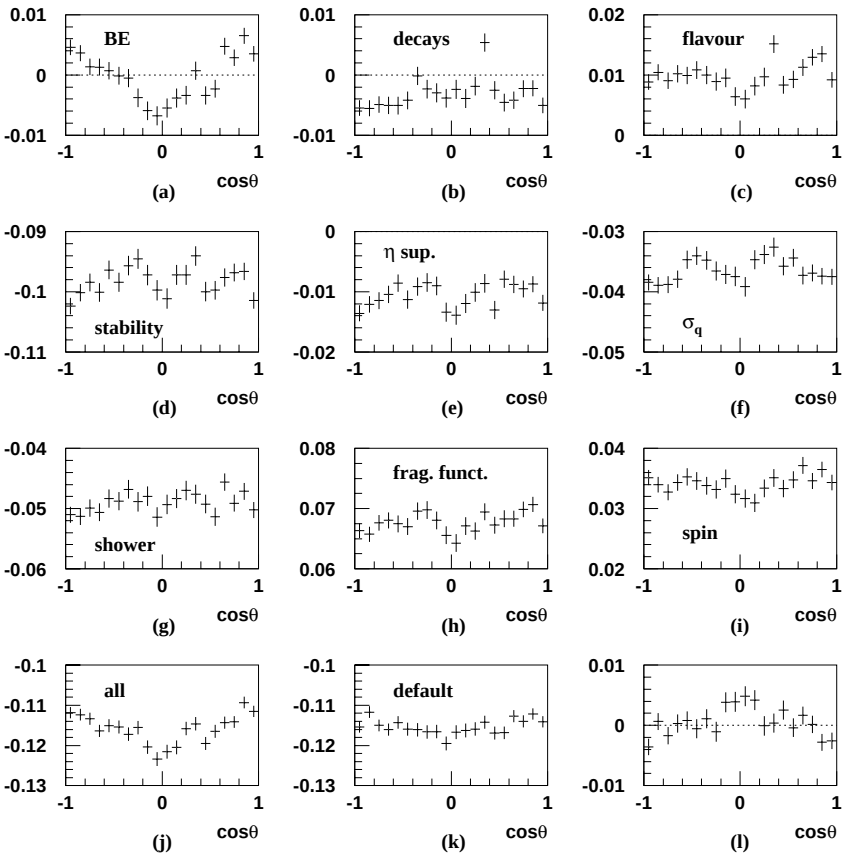

Figure 3.3. Relative (to the tuned) difference tuned minus modified tuned cosine of polar angle of the particle distributions when the following parameters / properties have been set to default: (a) Bose-Einstein effects, (b) decay tables, (c) flavour content, (d) stability of K^0_S, Λ, Σ^-, Σ^+, Ξ^-, Ξ^0, Ω^-, (e) η, η' suppression, (f) width of transverse momentum, (g) parton shower development, (h) fragmentation functions and (i) spin. The relative difference for all nine modifications of the tuned program is shown in (j). The relative (to the tuned) difference tuned minus default cosine theta is shown in (k). The difference between the last two distributions is given in (l).

CHAPTER 4

FRAGMENTATION FUNCTIONS

This chapter presents the extraction of the helicity components of the fragmentation function. The analysis is performed on data taken in 1992-1995 at Q=91.2 GeV and is meant as an update to the previous DELPHI analysis presented in [22], [23].

4.1 The measured distributions

The measured (raw data) distributions in x_p, the particle momentum divided by the beam energy, and $\cos\theta$, where θ is the polar angle of the particle (Fig. 1.5), for charged particles were obtained by processing the short DSTs (Data Summary Tapes) [24] with SKELANA [25]. A charged track was selected if it had [26]:

- an impact parameter in $R\phi$ below 5 cm,
- an impact parameter in z below $10\ \mathrm{cm}/\sin\theta$,
- a measured track length above 50 cm,
- a momentum between 0.1 GeV and 50 GeV,
- a polar angle between 11° and 169°,
- a momentum error, $\Delta p/p$, less than 100%.

An event was selected if it had [27]:

- at least 5 tracks with p>0.2 GeV,
- total energy above 15 GeV,
- more than 3 GeV of energy in each hemisphere,
- a sphericity axis polar angle between 26° and 154°,
- a momentum imbalance of 20 GeV at most.

The energies (of charged particles) were calculated using the measured momentum and assuming pion mass for the particles. The hemispheres were defined by the plane vertical to the sphericity axis. For all tracks in a specific event, the sums of the particle momenta in x, y and z were calculated. The quadratic sum of these three quantities was defined as the momentum imbalance of the event.

The statistics collected per year was the following: 551612 events in 1992, 552482 events in 1993, 1087172 events in 1994 and 521417 events in 1995. An example of raw data distribution in x_p and $\cos\theta$ is shown in Fig. 4.1.

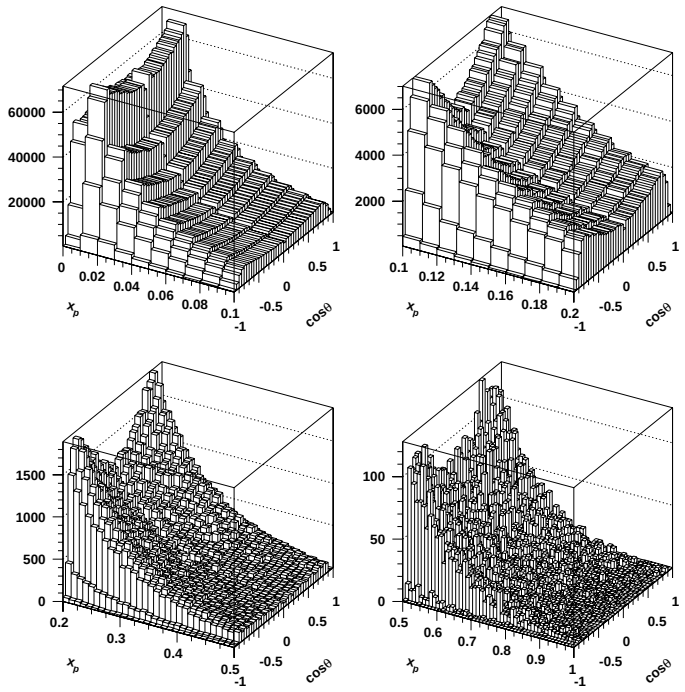

Figure 4.1. Distribution of x_p and $\cos\theta$ for charged particles (raw data 1992). The four plots represent different intervals of x_p.

4.2 Correction factors

The raw data discussed in the previous section needed to be corrected for the acceptance and resolution of the detector, detector inefficiencies, kinematic cuts, initial state radiation and secondary interactions with the detector's material. The correction factors were calculated with events initially generated with the DELPHI tuned JETSET 7.3 and then processed by the detector simulation (simulated events, for an ideal detector) and the data reconstruction program (reconstructed events). The track and event selection cuts for the reconstructed events were the same as for the real data (Section 4.1). The correction factors of a given interval i in x_p and $\cos\theta$ are obtained by dividing the simulated by the reconstructed distribution in this interval:

$$C_i(x_p, \cos\theta) = \frac{f_i(x_p, \cos\theta)_{simulated}}{f_i(x_p, \cos\theta)_{reconstructed}} \qquad (4.1)$$

In order to achieve enough statistics (Fig. 4.1), the range of the fractional momentum, x_p, of the particle was divided into 22 non-equidistant bins with smaller bins at low values (the momentum intervals are shown, e.g., in Fig. 4.2). The range of the cosine of the polar angle of the track, $\cos\theta$, was split into 40 equidistant bins. The corrections factors were

extracted according to Eq. 4.1 for each of the x_p and $\cos\theta$ bins separately. They are given in Fig. 4.2 - Fig. 4.5.

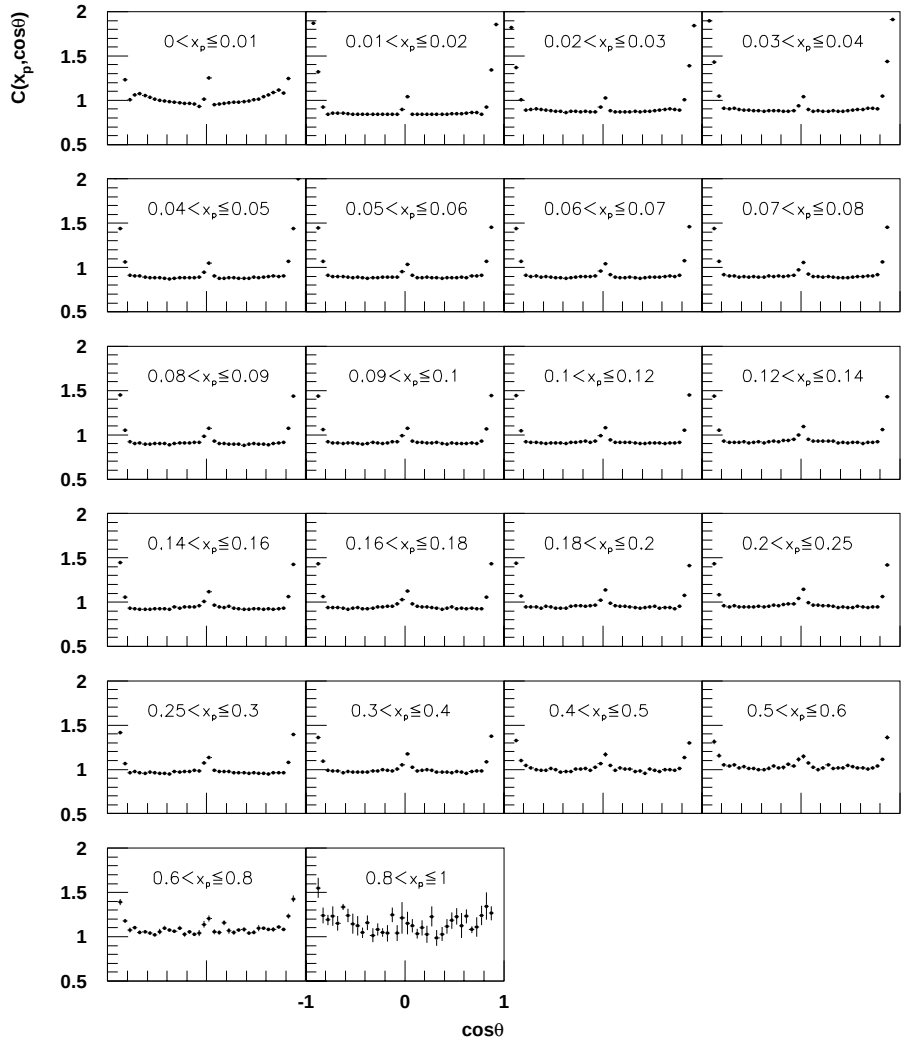

Figure 4.2. Correction factors for 1992. All plots have the same axes.

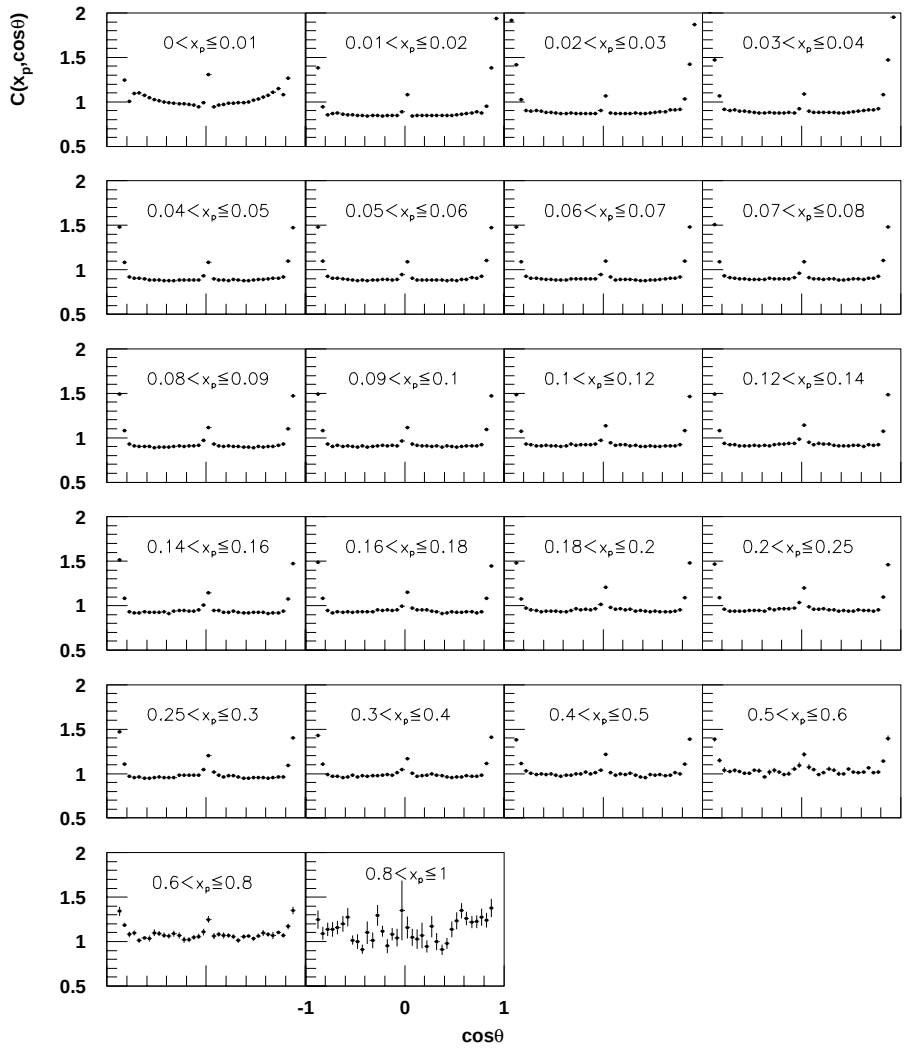

Figure 4.3. Correction factors for 1993. All plots have the same axes.

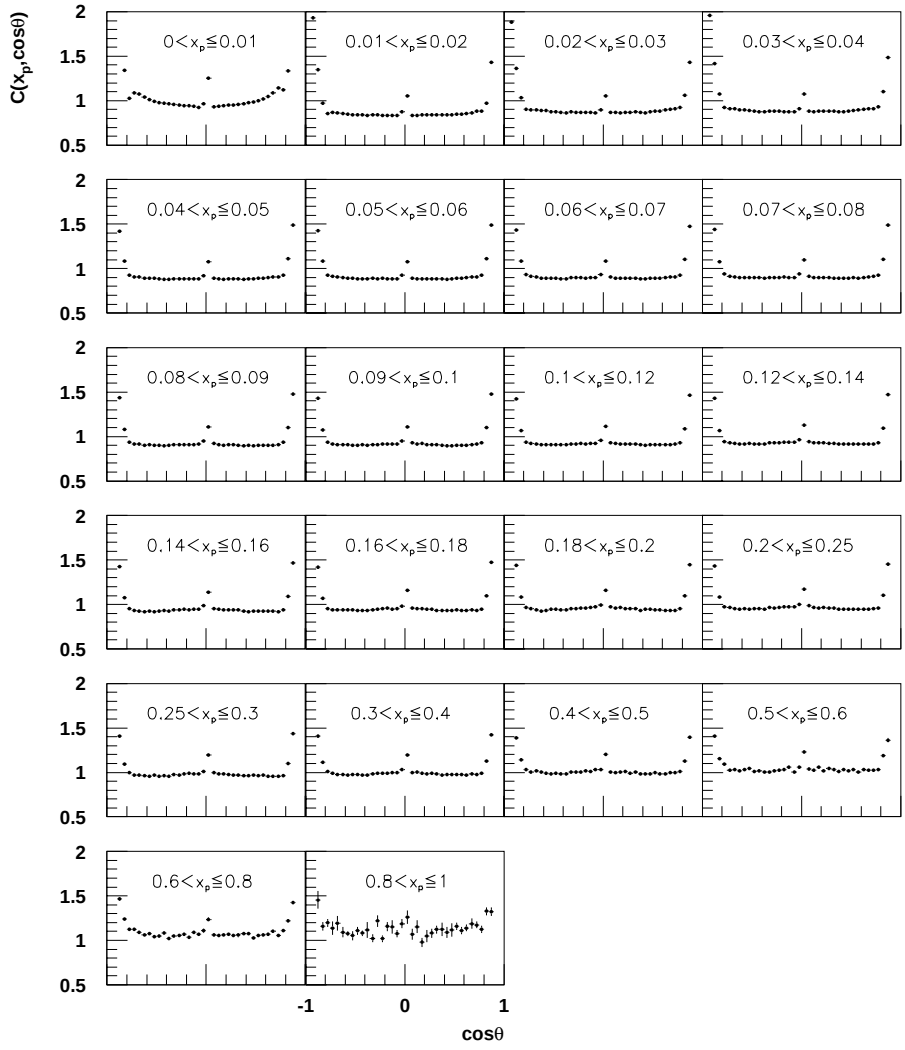

Figure 4.4. Correction factors for 1994. All plots have the same axes.

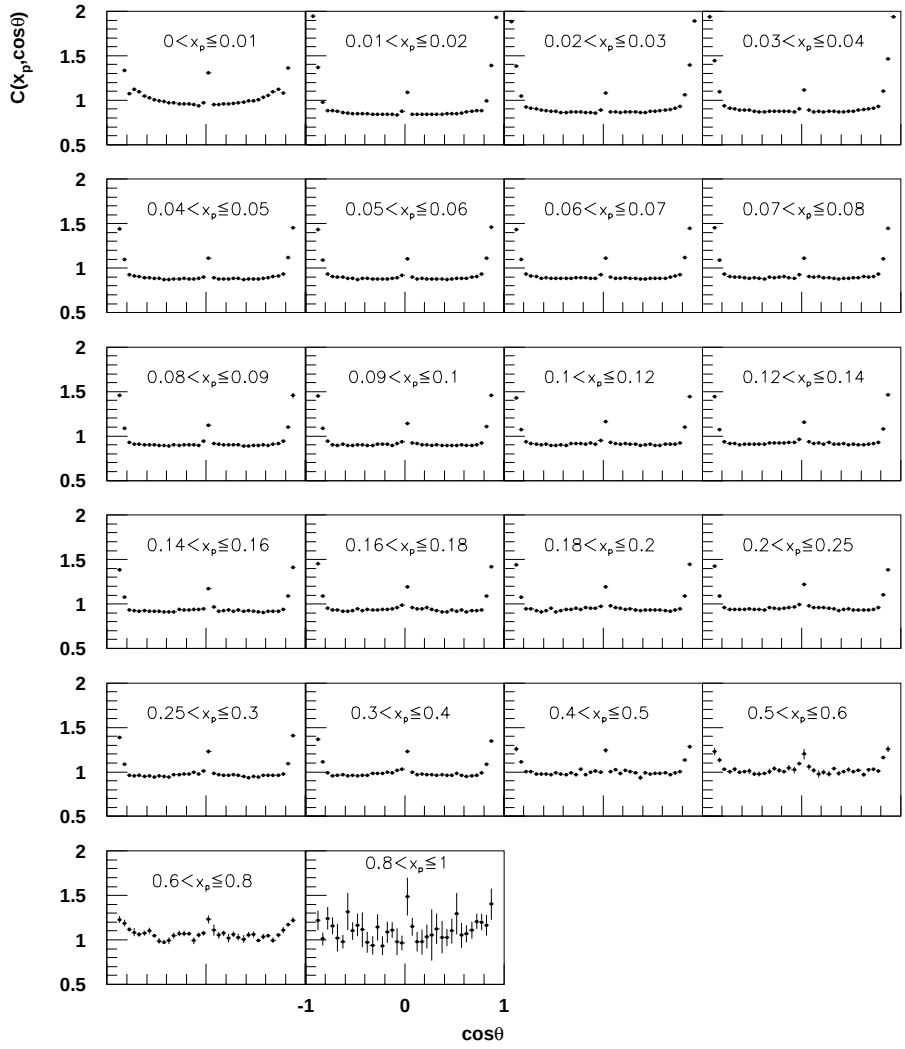

Figure 4.5. Correction factors for 1995. All plots have the same axes.

The number of simulated and reconstructed events per year are given in Table 4.1. The distributions in Fig. 4.2 - Fig. 4.5 have been normalized to these numbers.

year	number of simulated events	number of reconstructed events
1992	2299121	1722373
1993	1943948	1451797
1994	5568458	4173304
1995	1250970	928474

Table 4.1: Monte Carlo statistics for the extraction of the correction factors.

The errors of the correction factors were calculated as follows. The samples of 1992, 1993, 1994 and 1995 were subdivided into 12, 13, 14 and 12 subsets, respectively. The correction factors for each subset were calculated by Eq. 4.1. For each of the 40 cosθ bins and the 22 x_p bins, there were thus n values (n =12, 13, 14 or 12) for the correction factor. For each of the 880 bins, the error of the correction factor due to the variation of the n values in the i-th bin was calculated as the standard deviation of the mean

$$\delta C_{m_i} = \sigma_{\overline{C}_i} = \sqrt{\frac{1}{n(n-1)} \sum_{j=1}^{n} (C_i^j - \overline{C}_i)^2} \qquad (4.2)$$

where C_i^j is the value of the correction factor (calculated by Eq. 4.1) for the i-th bin and the j-th subset and $\overline{C}_i$ is the mean value of the j C_i^j values in bin i.

4.3 Corrected cross sections

The corrected double differential cross sections were extracted in two steps:

- the measured distributions in x_p and cosθ (Section 4.1) were normalized to the number of events and bin width,
- the correction factors were applied to the normalized distributions.

The corrected double differential cross sections were then given by

$$\sigma_i^{corr} = \frac{1}{\sigma_{tot}} \frac{d^2\sigma_i}{dx_p d\cos\theta} = C_i(x_p, \cos\theta) D_i^{meas} \qquad (4.3)$$

where D_i^{meas} are the measured distributions and C_i is the correction factor (Eq. 4.1). The index i refers to the x_p and cosθ bin. The corrected cross sections for 1992-1995 were subsequently combined as follows

$$\sigma_i^{combined} = \frac{\sum_{k=1}^{4} \frac{\sigma_i^{corr,k}}{(\delta\sigma_i^{corr,k})^2}}{\sum_{k=1}^{4} (\delta\sigma_i^{corr,k})^{-2}} \qquad (4.4)$$

where $\sigma_i^{corr,k}$ is the corrected cross section (Eq. 4.3) for the year 1992-1995 (denoted by the index $k = 1, \ldots, 4$) with error $\delta\sigma_i^{corr,k}$. The combined cross sections are shown in Fig. 4.6.

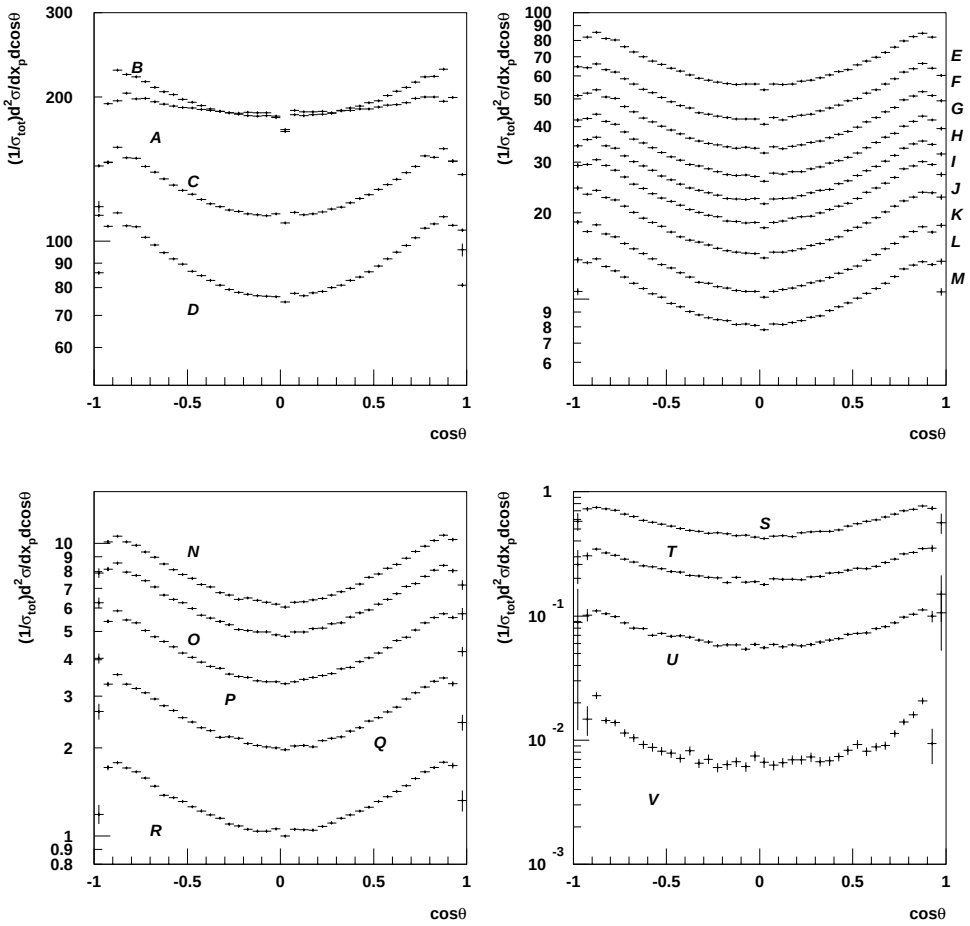

Figure 4.6. Combined (1992-1995) corrected double differential cross sections. The 22 x_p bins of e.g. Fig. 4.2 are labelled A to V in increasing momentum order.

4.4 Calculation by weights

The fragmentation functions, Eq. 3.5, were extracted with the weighting method [18]:

$$F_P = \int_{-v}^{v} W_P(\cos\theta, v)\left[\frac{1}{\sigma_{tot}}\frac{d^2}{dx_p d\cos\theta}\right]d\cos\theta \qquad (4.5)$$

where $P = T, L$, $v = |\cos\theta|_{max}$ and W_P are the weighting functions

$$W_T(\cos\theta, v) = ([5\cos^2\theta(3-v^2) - v^2(5-3v^2)]/(2v^5)),$$

$$W_L(\cos\theta, v) = ([v^2(5+3v^2) - 5\cos^2\theta(3+v^2)]/(4v^5)). \qquad (4.6)$$

For the extraction of the transverse (T) and longitudinal (L) components, nine equidistant values of $|\cos\theta|_{max}$ were considered between 0.95 and 0.55. The variation of the components as a function of $|\cos\theta|_{max}$ and x_p bin number (1-22) is shown in Fig. 4.7-Fig. 4.8. For the rest of the analysis, only the components corresponding to $|\cos\theta|_{max}$ = 0.85 were used (Fig. 4.9), as stable values of the fragmentation function components are obtained for this cosθ interval.

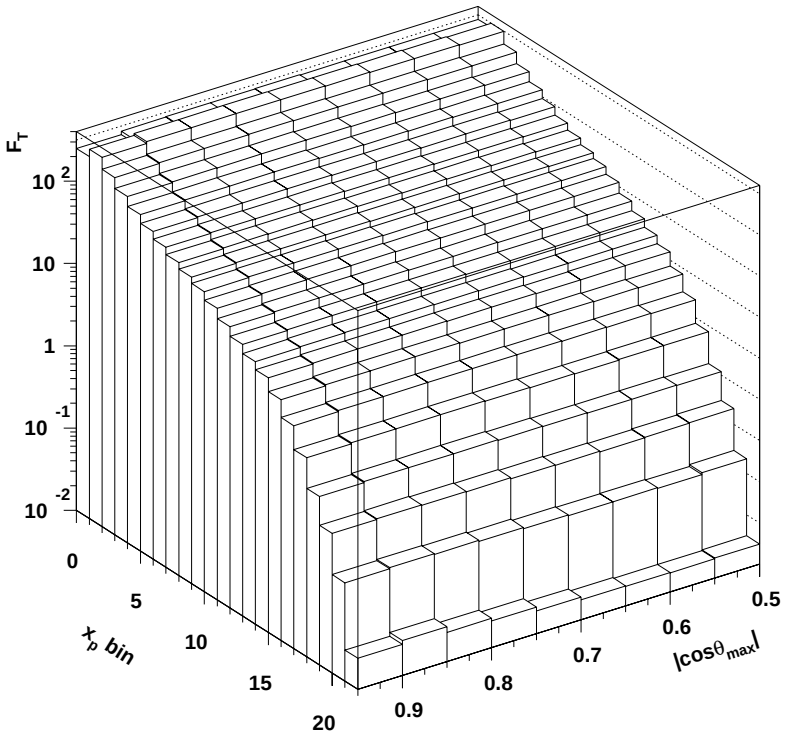

Figure 4.7. Variation of F_T from weights in the 22 x_p bins and for the 9 $|\cos\theta|_{max}$ values.

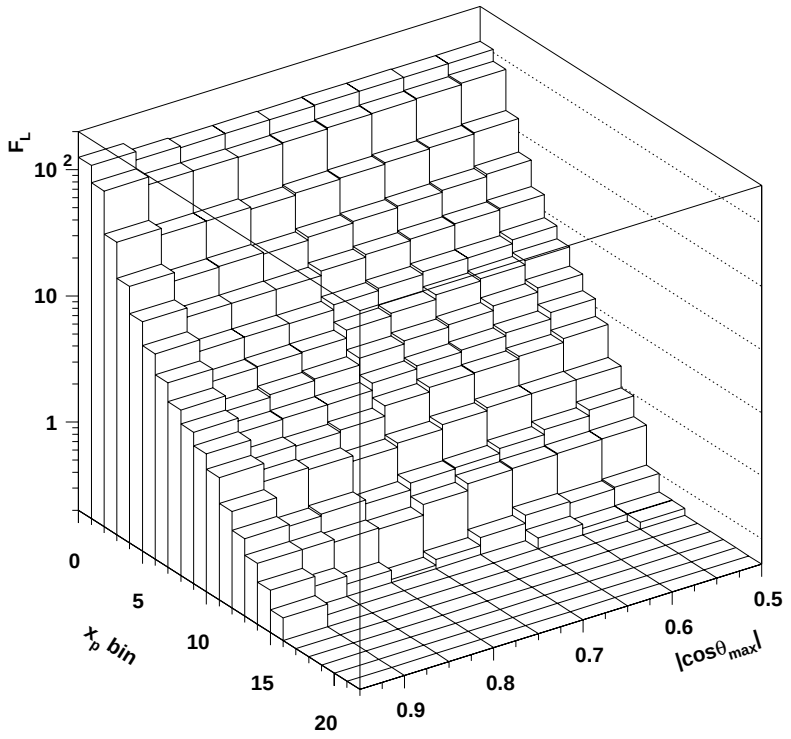

Figure 4.8. Variation of F_L from weights in the 22 x_p bins and for the 9 $|\cos\theta|_{max}$ values.

In Fig. 4.9, the comparison between the data and the three curves of simulated events shows that F_L from data is systematically below all simulations in almost all of the momentum interval, whereas this is not seen in F_T. This might be due to the fact that F_L is more sensitive than F_T to the fragmentation process. Moreover, the comparison shows that the tuned simulation is below the curve from Monte Carlo DSTs. A disagreement was expected due to the properties of the simulated DST events. JETSET 7.4 seems to describe the data better than the tuned simulation. It was not used by the collaboration for the production of the Monte Carlo DSTs, as it was not available when the tuned version was produced.

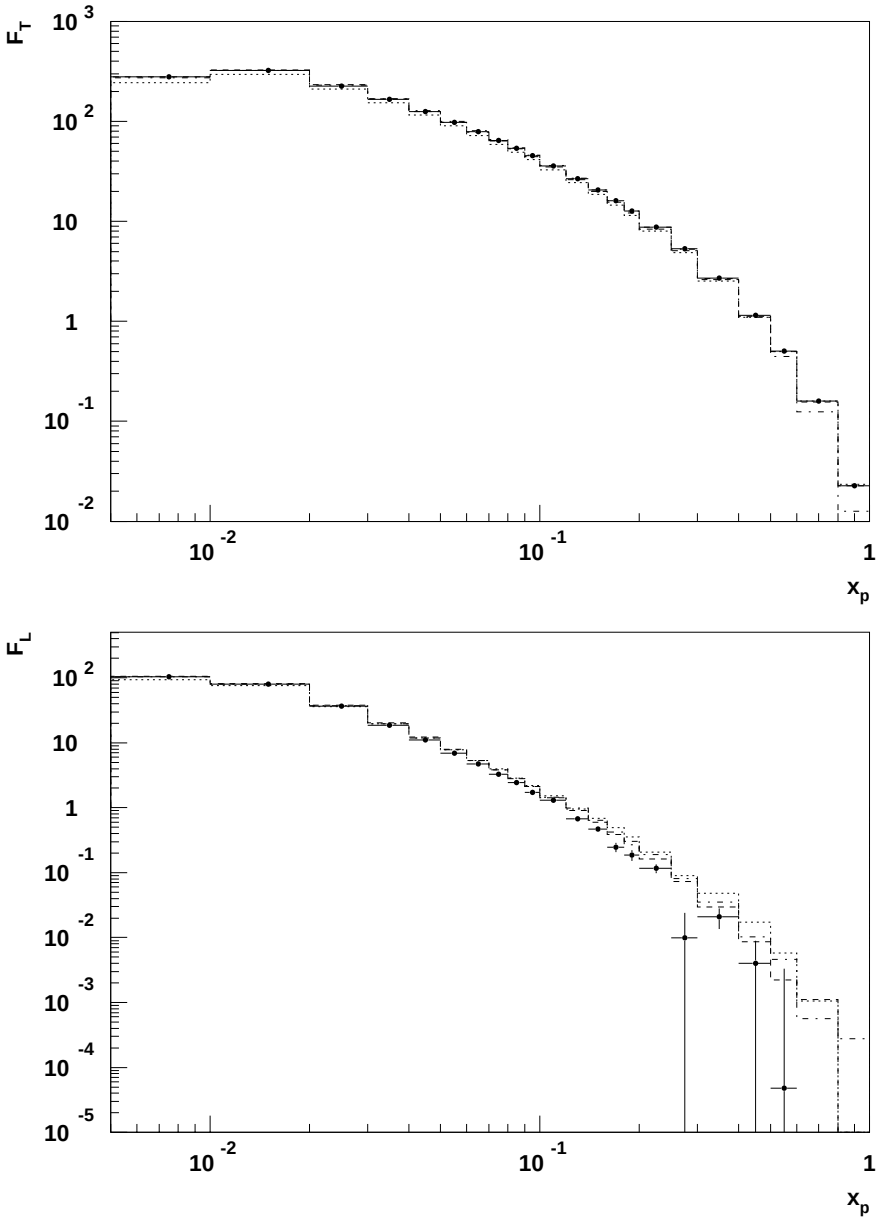

Figure 4.9. The transverse and longitudinal components of the fragmentation function, F_T and F_L, calculated from weights (Eq. 4.5). The points (solid line) are the data, the dashed line is the simulation on DELPHI DSTs, the dotted line is the tuned generator 7.3 and the dashed-dotted line is JETSET 7.4 (default).

4.5 Calculation by fitting

As a cross-check, the transverse and longitudinal components of the fragmentation function were extracted by fitting the differential cross section, Eq. 3.4, and treating the fragmentation function components as free parameters. The plots corresponding to Fig. 4.7-Fig. 4.8 are shown in Fig. 4.10-Fig. 4.11.

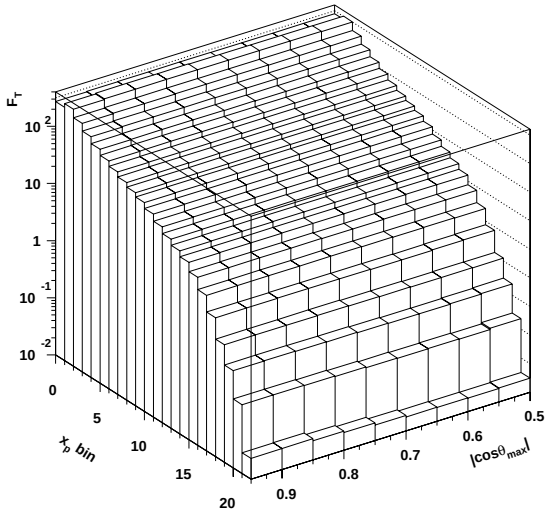

Figure 4.10. Variation of F_T from fitting in the 22 x_p bins and for the 9 $|\cos\theta|_{max}$ values.

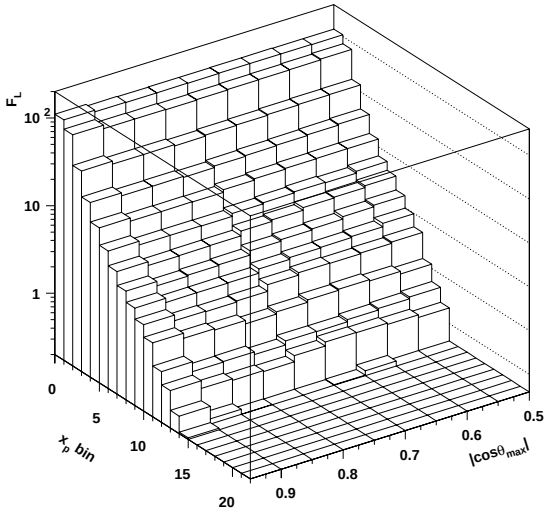

Figure 4.11. Variation of F_L from fitting in the 22 x_p bins and for the 9 $|\cos\theta|_{max}$ values.

The calculations by weighting and by fitting agree within errors in all x_p and $|\cos\theta|_{max}$ bins. The difference (weight calculation minus fit calculation) and relative difference (with respect to the weight calculation) for the transverse and longitudinal components are shown in Fig. 4.12. The comparison supports the choice of $|\cos\theta|_{max} = 0.85$ as the working interval as it is in the region of minimal difference between the two methods.

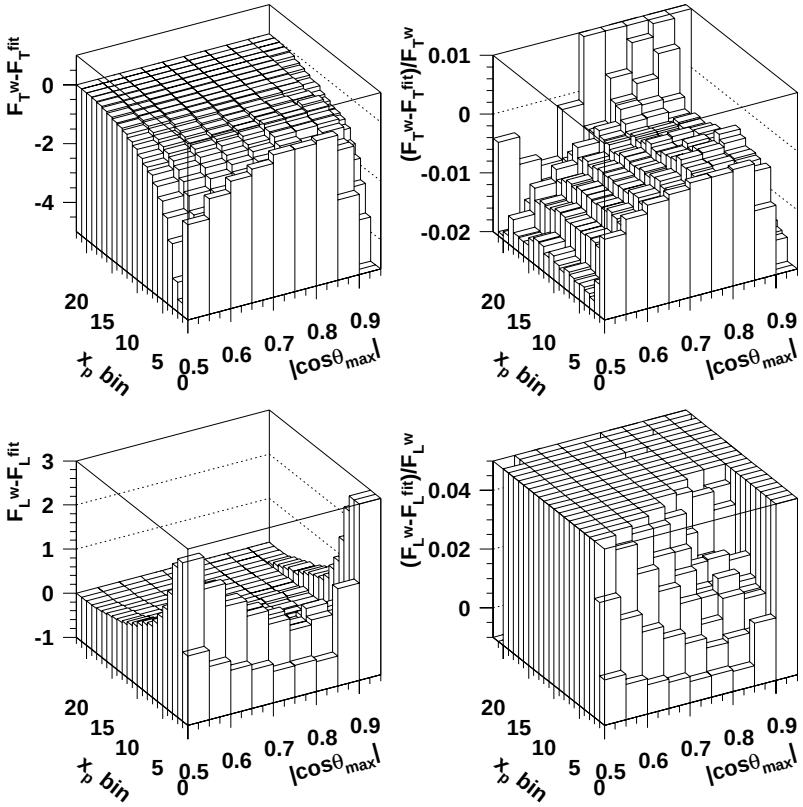

Figure 4.12. Difference (left) and relative difference (right) between the evaluations by weighting and by fitting of the transverse (up) and of the longitudinal (down, shown only up to 0.05 for the relative difference) components of the fragmentation function.

4.6 The fragmentation effect

After having confirmed that mass effects for b quarks can be neglected (Appendix D), the analysis addressed the issue of fragmentation effects [28], [29]. The hadrons are not emitted along the direction of their parent parton and this induces an artificial contribution to the fragmentation function components. This contribution will be positive for F_L and negative for F_T as can be deduced from the picture of a quark-antiquark pair moving back-to-back and producing a number of hadrons. The parton direction corresponds to the

$1+\cos^2\theta$ distribution in Eq. 3.4, therefore, if the hadrons were emitted along the direction of the initial partons, F_L would be vanishing. The smearing in the hadron p_T introduces a shift to a more isotropic picture, i.e. generates a $\sin^2\theta$ term in the angular distribution of the hadrons. This term is responsible for the appearance of a (positive) F_L component. F_T will be at the same time reduced so that the sum of two should remain constant. This nonvanishing component of F_L was extracted by running JETSET 7.4 with the parton shower switched off, i.e. while considering only $q\bar{q}$ events (Fig. 4.13). The fragmentation-induced F_L is clearly significant and mostly so at low x_p values. This was expected as the harder the hadron the closer it is emitted to the parent parton direction.

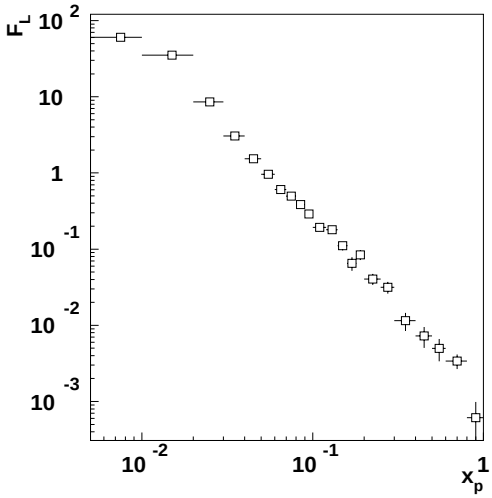

Figure 4.13. F_L from JETSET 7.4 (20 million events) in the absence of gluons.

Two different methods were used to correct the fragmentation function components for the fragmentation effect: the smearing method and the clustering method. They are described in Appendix D and in the following sections.

4.7 The smearing method

A first attempt to correct for the fragmentation effect was to use the simulation run mentioned above as follows [28] (Appendix D). Each (charged) hadron was assigned the closest in angle parton as being its parent parton. The angle between the two particles was then histogrammed for the 22 x_p bins of the analysis. The intention was to use this 'smearing angle' to distort (smear) the polar angle in Eq. 3.4 and then use this smeared expression for the extraction of the fragmentation function components. This would have as a result that the smearing effect would reside entirely in the angles thus leaving the extracted components unaffected by the smearing. Apart from the 7.4 version of the JETSET generator, the DELPHI tuning was also used to this purpose, with two different values for the width of the generated hadron transverse momentum distribution, σ_q: zero and the tuned value (0.428 GeV). The distributions of the smearing angle for these three cases are shown in Fig. 4.14-Fig. 4.16.

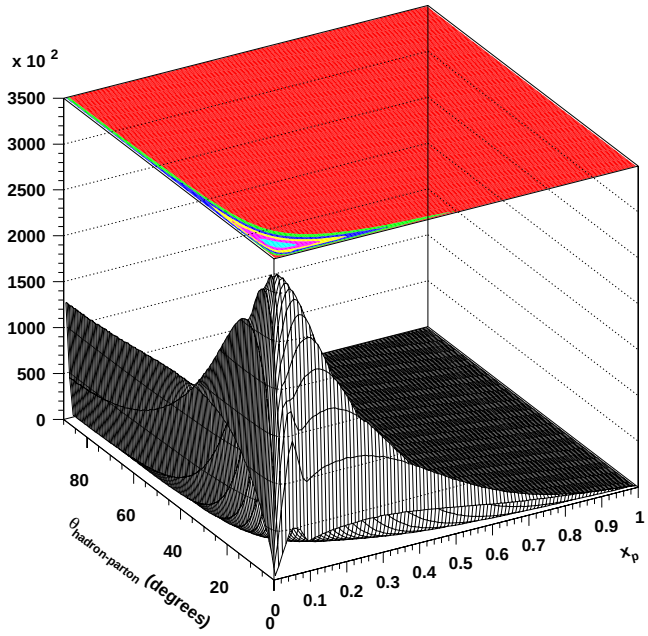

Figure 4.14. Angle between the hadron and the parton in two-jet events with the shower switched off (JETSET 7.4 (σ_q=0.36 GeV), 20 million events).

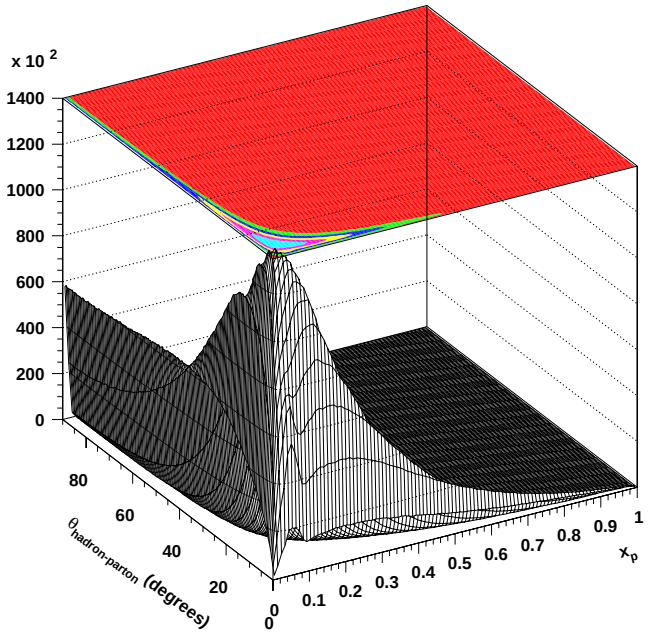

Figure 4.15. Angle between the hadron and the parton in two-jet events with the shower switched off (DELPHI tuning (σ_q=0.428 GeV), 5 million events).

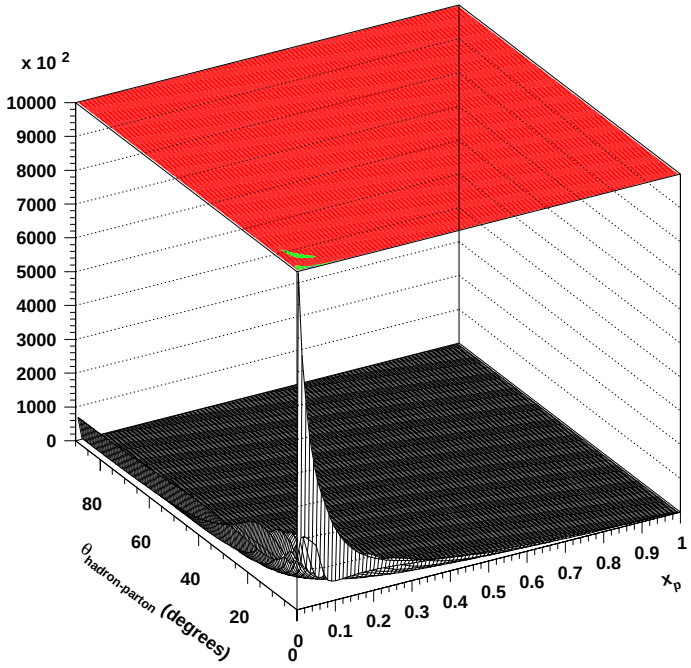

Figure 4.16. Angle between the hadron and the parton in two-jet events with the shower switched off (σ_q=0 GeV, 5 million events).

The smearing of the polar angle of the hadron was done as follows. First, it was assumed that the parton axis was along the z direction (Fig. 4.17(a)). The hadron is taken to be at angles θ_2 and ϕ with respect to that direction. This gives for the coordinates of the hadron:

$$x^0_{hadron} = \sin\theta_2 \cos\phi \tag{4.7}$$

$$y^0_{hadron} = \sin\theta_2 \sin\phi \tag{4.8}$$

$$z^0_{hadron} = \cos\theta_2 \tag{4.9}$$

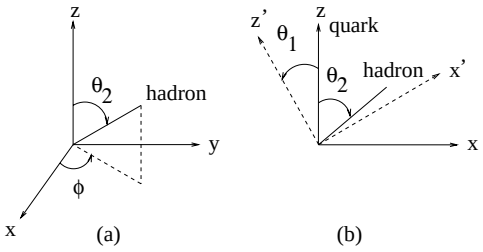

Figure 4.17. Angles used for the smearing. In (a), the parton direction is along the z axis. In (b), the parton direction is rotated to an angle θ_1 with respect to the z axis.

The system is then rotated in the (x,z) plane so that the parton is now at an angle θ_1 with respect to the z axis. Before the rotation, the coordinates of the hadron are, as shown in Fig. 4.17:

$$x^0_{hadron} = \sin\theta_2 \tag{4.10}$$

$$z^0_{hadron} = \cos\theta_2 \tag{4.11}$$

After the rotation, the coordinates of the hadron are:

$$x_{hadron} = \sin(\theta_1 + \theta_2) \tag{4.12}$$

$$z_{hadron} = \cos(\theta_1 + \theta_2) \tag{4.13}$$

The y coordinate is not affected by the rotation. From Eq. 4.12 and Eq. 4.13, the coordinates of the hadron after the rotation can be written as

$$x_{hadron} = \sin\theta_1\cos\theta_2 + \cos\theta_1\sin\theta_2 = \sin\theta_1 z^0_{hadron} + \cos\theta_1 x^0_{hadron} \tag{4.14}$$

$$z_{hadron} = \cos\theta_1\cos\theta_2 - \sin\theta_1\sin\theta_2 = \cos\theta_1 z^0_{hadron} - \sin\theta_1 x^0_{hadron} \tag{4.15}$$

From Eq. 4.7, Eq. 4.9 and Eq. 4.14, it follows that

$$x_{hadron} = \sin\theta_1\cos\theta_2 + \cos\theta_1\sin\theta_2\cos\phi \tag{4.16}$$

From Eq. 4.7, Eq. 4.9 and Eq. 4.15, it follows that

$$z_{hadron} = \cos\theta_1\cos\theta_2 - \sin\theta_1\sin\theta_2\cos\phi \tag{4.17}$$

and, therefore, the polar angle of the hadron is given by

$$\cos\theta = \cos\theta_1\cos\theta_2 - \sin\theta_1\sin\theta_2\cos\phi \tag{4.18}$$

where θ_1 is the parton angle and θ_2 is the smearing angle. Eq. 4.18 gives the smeared polar angle of the hadron that will be inserted in Eq. 3.4 to extract the fragmentation function components.

As the smearing of the polar angle in Eq. 3.4 cannot be done analytically, the following procedure was adopted. The functions

$$f_1 = 1 + \cos^2\theta \tag{4.19}$$

$$f_2 = \sin^2\theta \tag{4.20}$$

$$f_3 = 1 + \cos\theta \tag{4.21}$$

were defined. Additionally, a constant function was used for the ϕ angle, assuming this was isotropic. A loop over hadrons was then done, selecting randomly:

- a value for the polar angle of the parton according to Eq. 4.19
- a value for the polar angle of the parton according to Eq. 4.20
- a value for the polar angle of the parton according to Eq. 4.21
- a value for the angle ϕ from the constant distribution

The two-dimensional distributions of the smearing angle (Fig. 4.14-Fig. 4.16) were sliced in the 22 x_p bins. The resulting histograms were normalized to unit area (as shown, e.g. in Fig. 4.18) and used to select randomly the smearing angle for each hadron and each momentum bin.

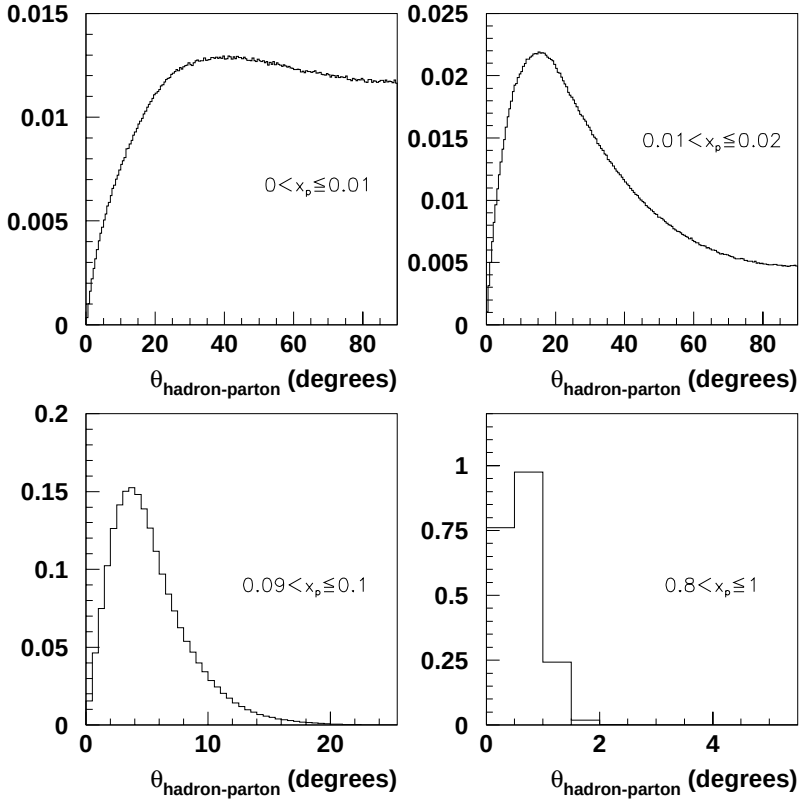

Figure 4.18. Smearing angle distributions for four momentum bins (DELPHI tuning, 5 million events). The distributions are normalized to unit area.

From the values of the randomly selected angles, the smeared hadron angle was calculated using Eq. 4.18 for each of the functions f_1, f_2 and f_3. The smeared functions thus produced are shown in Fig. 4.19. As the figure shows, the smearing of the polar angle is most significant in the first momentum bin and the effect gradually decreases till x_p values around 0.1 are reached. This x_p value corresponds to the tenth momentum bin. In higher momentum bins, the smearing does not affect significantly the fitting functions.

The smeared functions were subsequently used to do fits to the data in the same way as described in Section 4.5, the difference being that the fitting functions were now histogrammed and not analytical and that the four central points in the cosθ distributions were omitted (to optimize the fit). The fits in the first, second, tenth and last momentum bins are shown in Fig. 4.20. The extracted values for the fragmentation function components in

these bins are also shown in the figure. The resulting distributions of F_T and F_L are shown in Fig. 4.21 and Fig. 4.22, respectively, for all momentum bins and in Fig. 4.23 and Fig. 4.24, respectively, for the first ten momentum bins. There are four histograms in each plot, one without smearing and three corresponding to a different generator choice for the smearing angle. The ratio of F_T with smearing to F_T without smearing is given in Fig. 4.25. The smearing angle was taken from the DELPHI tuned generator. The same ratio for F_L is shown in Fig. 4.26. The correction for the transverse momentum of the hadrons is significant at low momenta, especially for F_L, which is reduced by one order of magnitude in the first momentum bin.

It should be noted, however, that the smearing procedure is rather approximate since it neglects completely the presence of gluon jets. This will be taken into account in the clustering method, which is described in the next section.

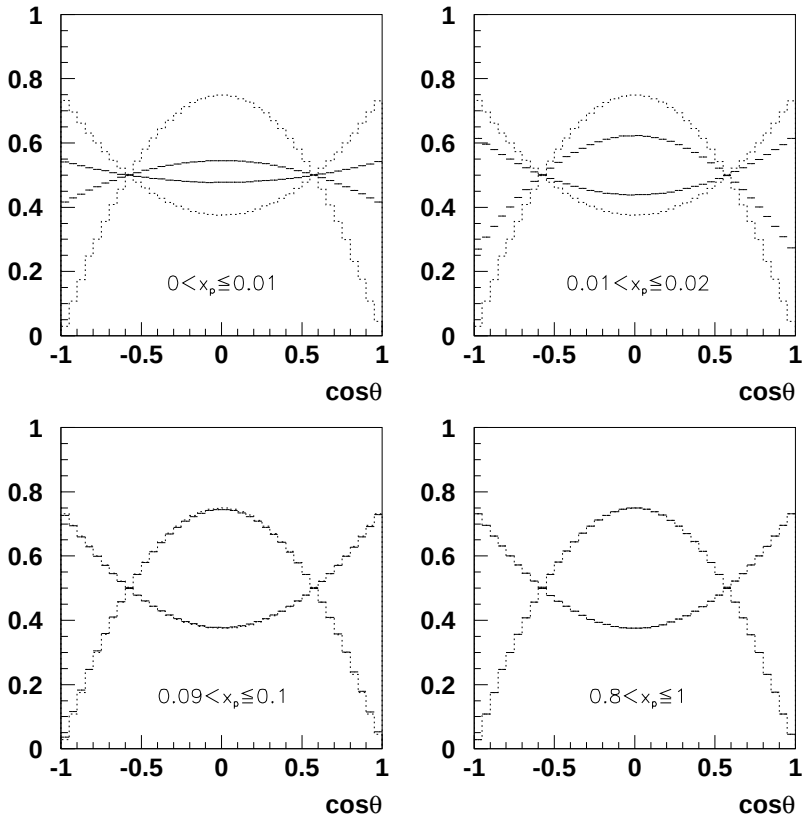

Figure 4.19. Smeared (solid histograms) and non-smeared (dotted histograms) functions f_1 and f_2 (Eq. 4.19, Eq. 4.20) for four momentum bins. In the first momentum bin (x_p less than 0.01), the smeared functions are almost flat, whereas there is essentially no change in the functions f_1 and f_2 for x_p greater than 0.1. In the last plot, corresponding to the last momentum bin, the solid and dotted histograms overlap.

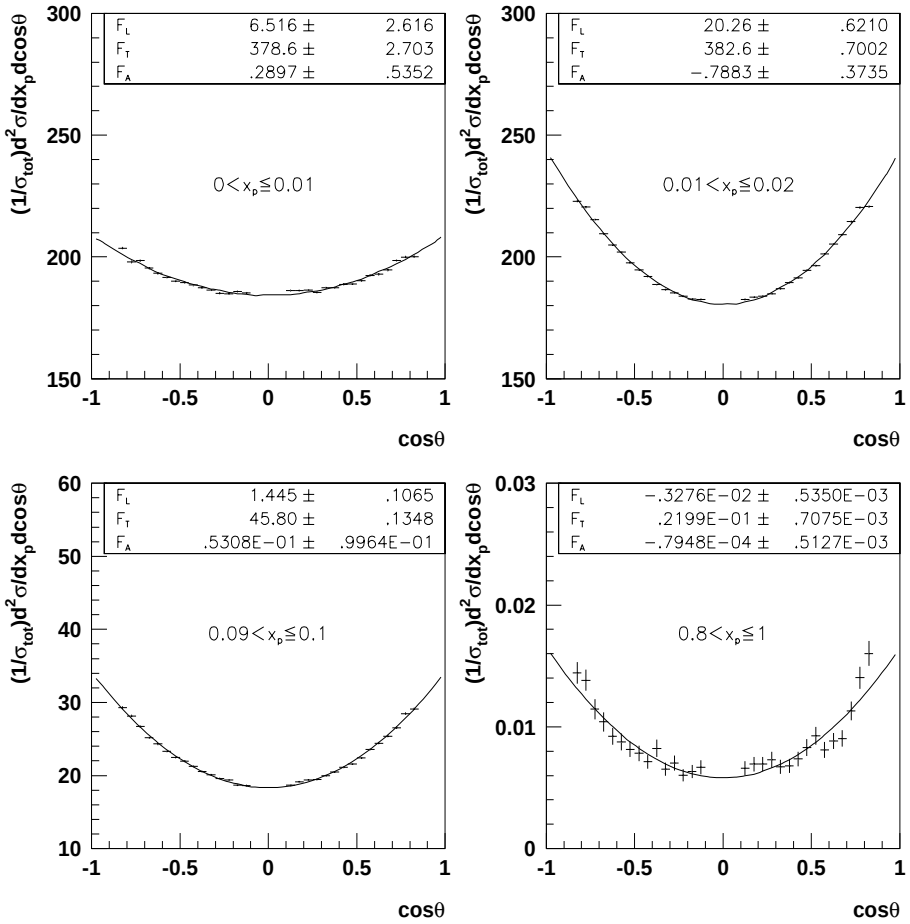

Figure 4.20. Fits to the data (Fig. 4.6) using smeared histogrammed functions of the polar angle of the hadron (Eq. 4.19-Eq. 4.21).

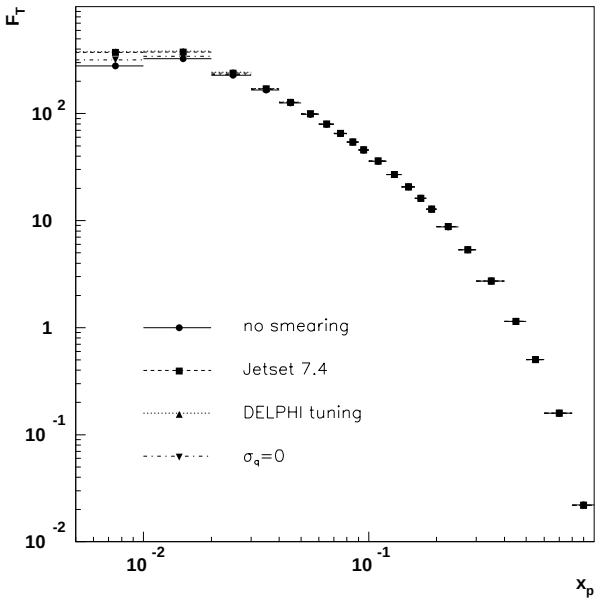

Figure 4.21. F_T without smearing and with smearing for three cases of smearing angle: from JETSET 7.4, from DELPHI tuning and for σ_q=0 GeV (in the tuned generator).

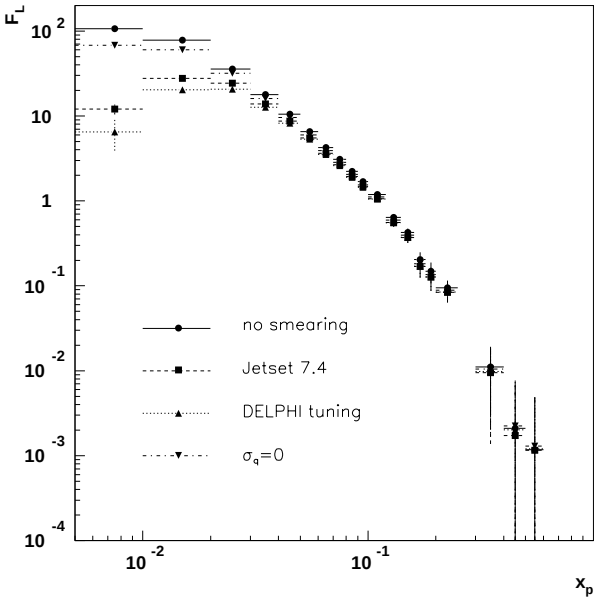

Figure 4.22. F_L without smearing and with smearing for three cases of smearing angle: from JETSET 7.4, from DELPHI tuning and for σ_q=0 GeV (in the tuned generator).

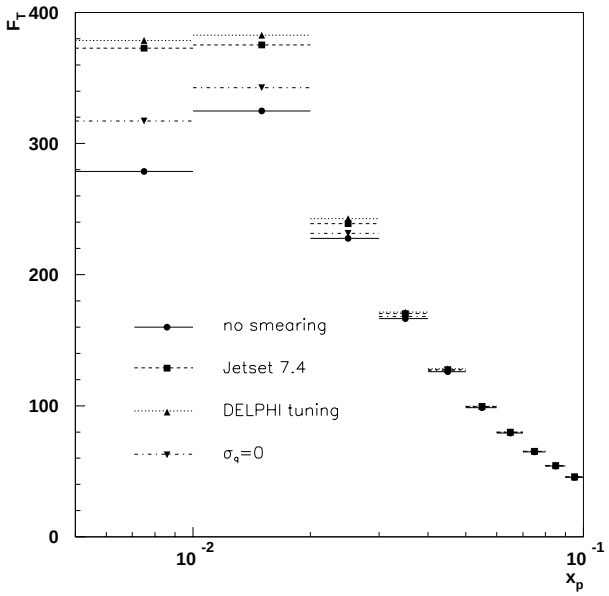

Figure 4.23. F_T in the first ten momentum bins without smearing and with smearing for three cases of smearing angle: from JETSET 7.4, from DELPHI tuning and for σ_q=0 GeV (in the tuned generator).

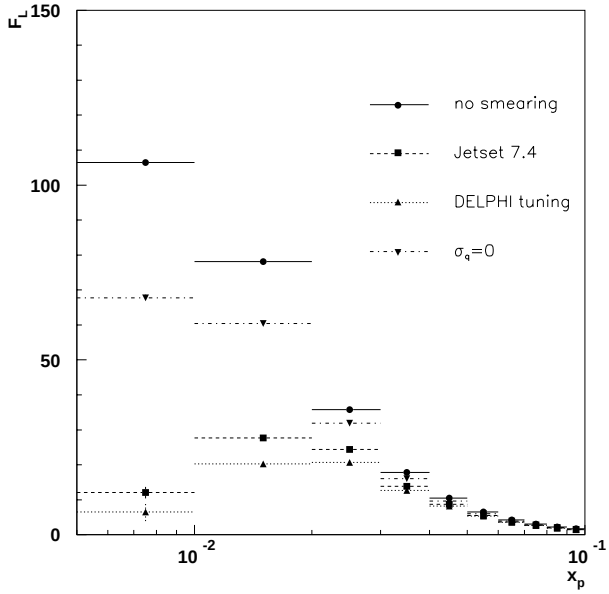

Figure 4.24. F_L in the first ten momentum bins without smearing and with smearing for three cases of smearing angle: from JETSET 7.4, from DELPHI tuning and for σ_q=0 GeV (in the tuned generator).

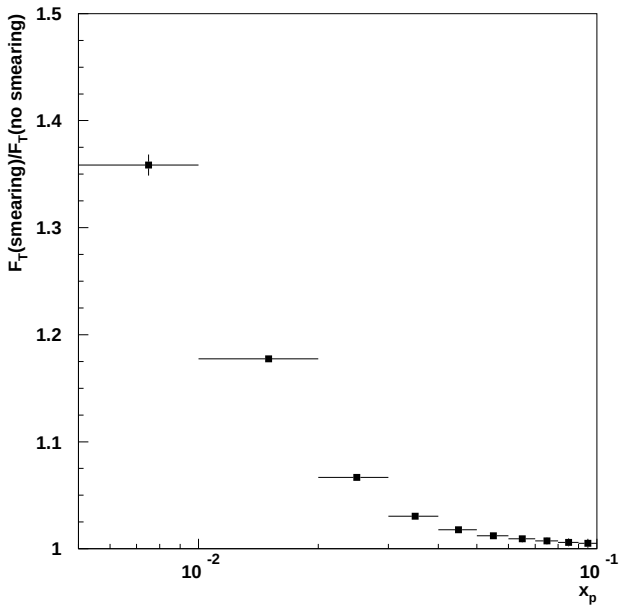

Figure 4.25. F_T with smearing divided by F_T without smearing. The smearing angle was taken from the DELPHI tuning. Only the first ten momentum bins are shown.

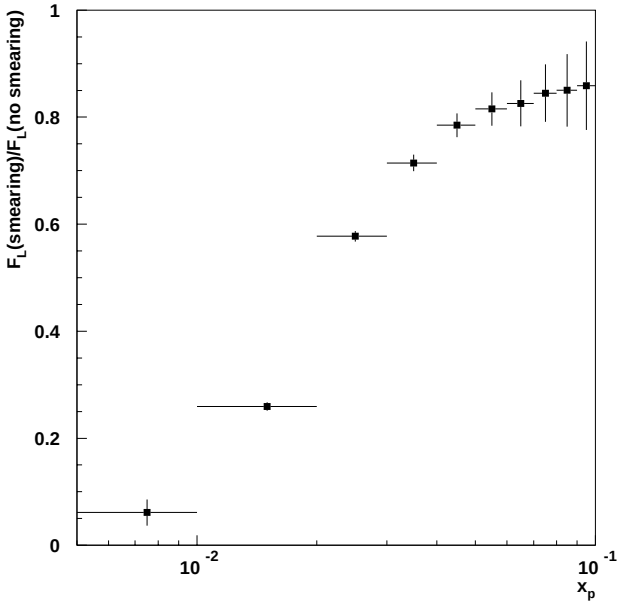

Figure 4.26. F_L with smearing divided by F_L without smearing. The smearing angle was taken from the DELPHI tuning. Only the first ten momentum bins are shown.

4.8 Correction by clustering

Having the string picture in mind, one expects to have a larger smearing at low momenta than what was assumed in the smearing method. This is due to the hyperbolic shape of the string, as shown in Fig. 4.27. Furthermore, the string will pull particles from, e.g., the gluon jet towards the antiquark jet and also from the antiquark jet towards the gluon jet, as shown by the vertical arrows in Fig. 4.27 (the string / drag effect) [30]. This means that the anisotropy introduced by the presence of the gluon will be reduced, i.e. the string is now giving a correction to F_T and F_L which has the opposite sign as the correction needed for the fragmentation p_T smearing. To account for these effects, the clustering method was introduced in the analysis [28] (Appendix D).

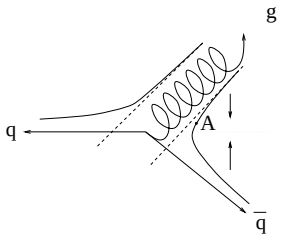

Figure 4.27. The string effect in a three- jet event.

The DELPHI tuned generator was used to generate 5 million events with no topology restrictions. Then, the Durham algorithm [31] was applied to cluster the stable hadrons[1] (only charged particles were considered) into a number of clusters, each assumed to represent a mother parton. The direction of each cluster was thus thought of as the direction of a parton, each having a number of daughter hadrons associated to it. The correction entailed replacing the polar angle of the (charged) hadrons by the polar angle of the associated cluster (parton). The momentum of the hadron was not changed. This resulted in having events where all hadrons were aligned with their parent partons, i.e. as Eq. 3.4 assumes to be the case. Consequently, applying Eq. 3.4 to the cluster-deduced polar angle ($\cos\theta$) distributions of the charged hadrons would give fragmentation function components which are not affected by smearing effects during the fragmentation procedure. The question was to find a suitabe clustering cut-off scale. This is addressed in Appendix D. A less strict way of discussing this question could be the following. As the parton polar angle is smeared by the hadronization process itself, the aim is to recover the (polar angle of the) mother parton at the moment hadronization began, i.e. approximately at the moment the parton shower stopped. The shower cut-off value for the default versions of JETSET 7.4 and JETSET 7.3 is 1 GeV. In the tuned simulation, this value is 2.25 GeV. Considering Fig. 4.9, it is difficult to have a strong preference for either value, therefore, exploring the interval 1-2 GeV would seem a reasonable possibility. In Appendix D, the range 1-4.5 GeV was considered. As 4.5 GeV seems to produce a rather large correction even at high momentum values (Fig. 5 in Appendix D), it was not considered in the data correction in this report. In Appendix D, both charged and neutral particles are clustered and the clustering cut-off used was the scaled cut-off parameter of the

[1] In the present context, by "hadrons" is meant "hadrons and their decay products", i.e. also leptons (or, for neutral particles, photons) from a hadron decay.

Durham algorithm. However, only charged particles are considered in the data. Therefore, instead of the scaled cut-off, the following distance measure will be used in the following:

$$y_{ij} = \sqrt{2min(E_i^2, E_j^2)(1 - \cos\theta_{ij})} \qquad (4.22)$$

where $E_{i,j}$ is the energy of the cluster i, j and θ_{ij} is the opening angle between the momentum vectors of the two clusters. The distance measure[2], or cut-off parameter, y_{ij}, is the maximum distance, below which two clusters can be joined in one and corresponds roughly to the relative transverse momentum of the two clusters. From Appendix D, the following values were considered for the cut-off parameter of the clustering: y=0.912 GeV, y=1.290 GeV and y=2.040 GeV (deduced from the cut-off values used in the Appendix by taking the square root and multiplying by the cms energy). The correction procedure is explained below.

For each value of the clustering cut-off parameter, the output of the generator was two sets of cosθ (cosine of polar angle) distributions, each distribution referring to a momentum bin (as in the data). The first set of distributions showed the polar angle of the charged hadrons. The second set showed the polar angle of the clusters. The former distributions were expected to show less structure than the latter ones, as can be seen in Fig. 4.28.

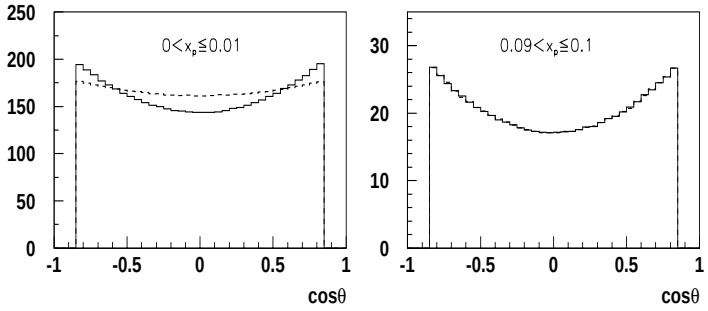

Figure 4.28. cosθ distributions for charged hadrons (dashed histograms) and clusters (solid histograms) in the first (left) and the tenth (right) momentum bin. The clustering was done for a cut-off parameter of 0.912 GeV. The solid and dashed histograms overlap in the latter case.

The 22 cosθ distributions of the hadrons and of the clusters were then normalized to number of events (5 million) and to bin width in cosθ and x_p, as was done in the data. The normalized distributions were used to extract the fragmentation function components for hadrons and for clusters. Both the weighting and the fitting methods were applied. In the fitting method, there were no central points excluded (cf p. 56). The components thus extracted are shown in Fig. 4.29 - Fig. 4.32.

[2] The distance measure, y_{ij}, will be referred to as 'y' in the following.

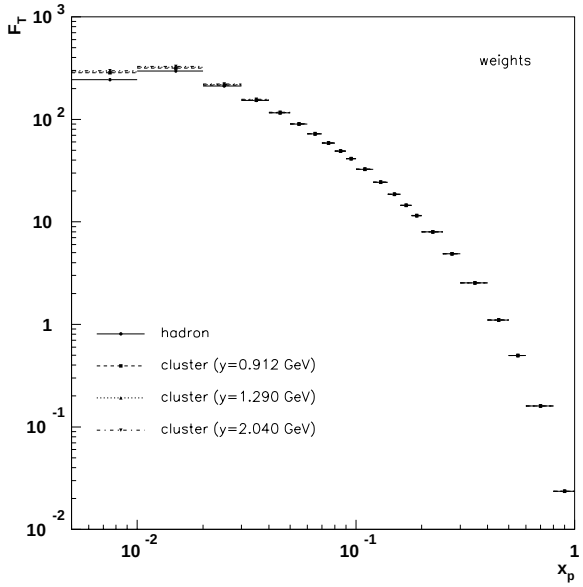

Figure 4.29. F_T from weights for hadrons and for clusters from Monte Carlo events (DELPHI tuning). Three values for the clustering cut-off parameter, y, were used.

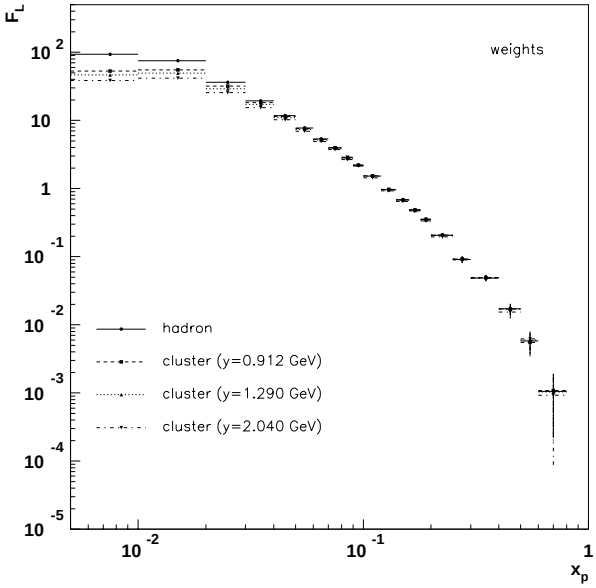

Figure 4.30. F_L from weights for hadrons and for clusters from Monte Carlo events (DELPHI tuning). Three values for the clustering cut-off parameter, y, were used.

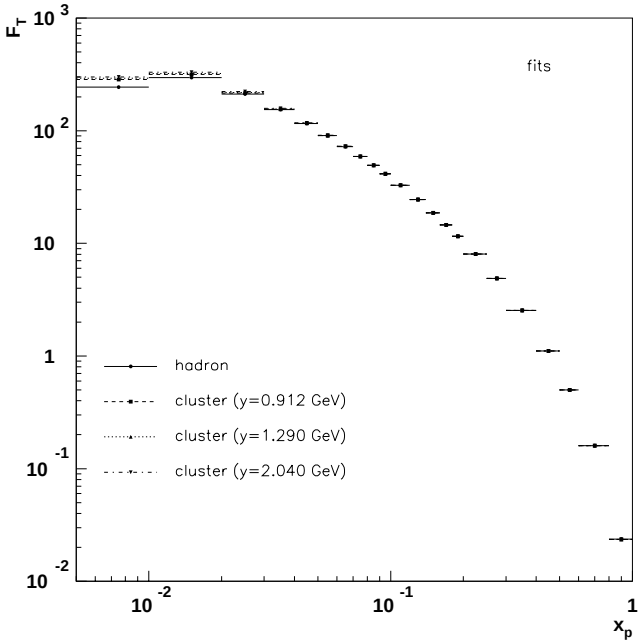

Figure 4.31. F_T from fits for hadrons and for clusters from Monte Carlo events (DELPHI tuning). Three values for the clustering cut-off parameter, y, were used.

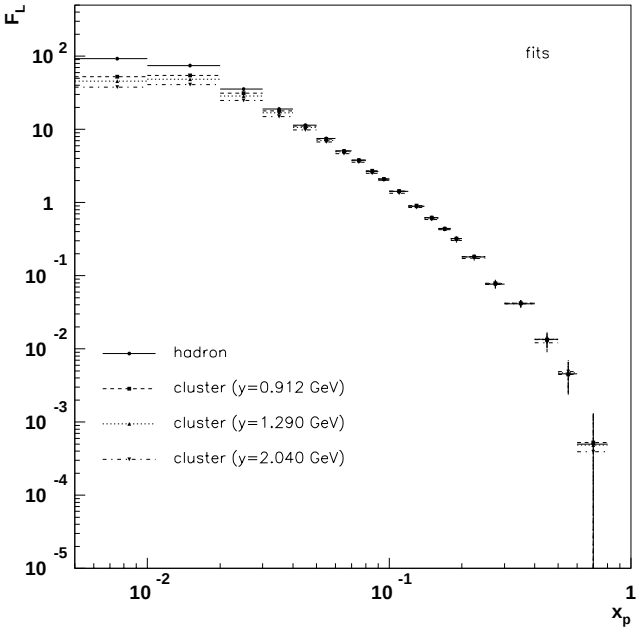

Figure 4.32. F_L from fits for hadrons and for clusters from Monte Carlo events (DELPHI tuning). Three values for the clustering cut-off parameter, y, were used.

From the Monte Carlo distributions above, a correction to the data can be calculated starting from the difference of the distributions of hadrons and clusters. However, the different normalization in data and Monte Carlo has to be taken into account, leading to a correction of the form:

$$(F_P)_{corrected} = (F_P)_{data} - \frac{(F_T + F_L)_{data}}{(F_T + F_L)_{MC}} (F_P^{\,hadron} - F_P^{\,cluster})_{MC} \qquad (4.23)$$

where P=T,L. $(F_P)_{data}$ is the original component as was extracted from the data and $(F_P)_{corrected}$ is the corrected component. The corrected fragmentation function components are given in Fig. 4.33 - Fig. 4.36. Results are shown both for the weighting method and for the fitting method. The correlation between errors has been taken into account [32].

The ratios of the fragmentation function components after and before the correction are shown in Fig. 4.37 and Fig. 4.38. As expected, the correction by clustering is milder than the correction by smearing but still significant for both helicity components.

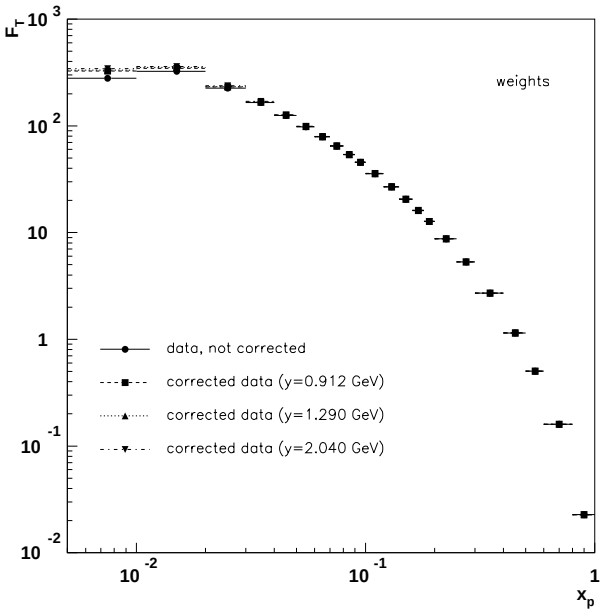

Figure 4.33. F_T from original data and F_T corrected for the fragmentation effect by clustering. The weighting method has been applied to data and Monte Carlo. The corrected component is given for three values of the cut-off parameter, y, for the Durham clustering algorithm.

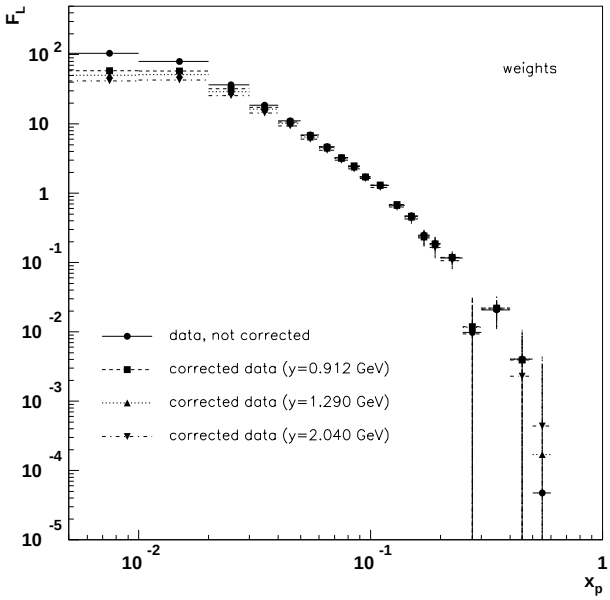

Figure 4.34. F_L from original data and F_L corrected for the fragmentation effect by clustering. The weighting method has been applied to data and Monte Carlo. The corrected component is given for three values of the cut-off parameter, y, for the Durham clustering algorithm.

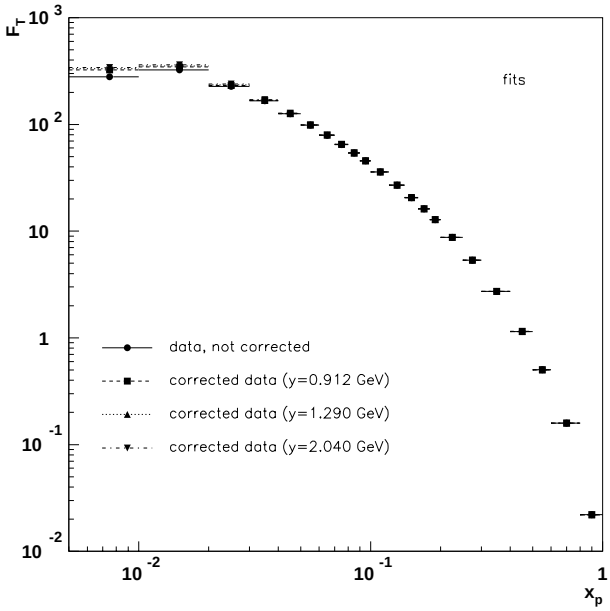

Figure 4.35. F_T from original data and F_T corrected for the fragmentation effect by clustering. The fitting method has been applied to data and Monte Carlo. The corrected component is given for three values of the cut-off parameter, y, for the Durham clustering algorithm.

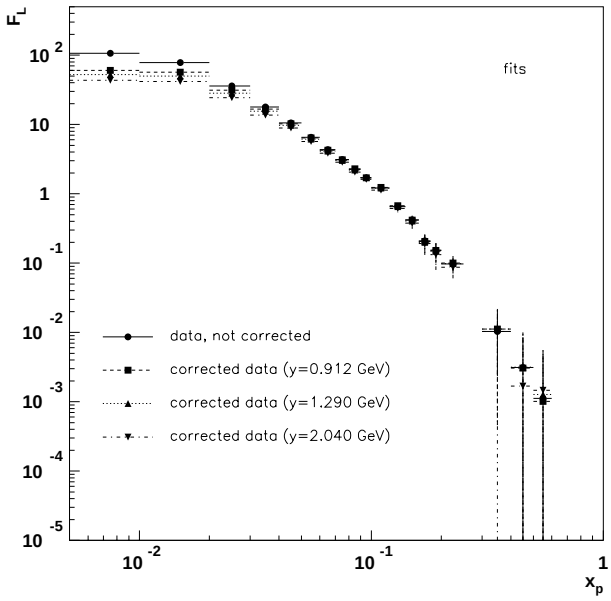

Figure 4.36. F_L from original data and F_L corrected for the fragmentation effect by clustering. The fitting method has been applied to data and Monte Carlo. The corrected component is given for three values of the cut-off parameter, y, for the Durham clustering algorithm.

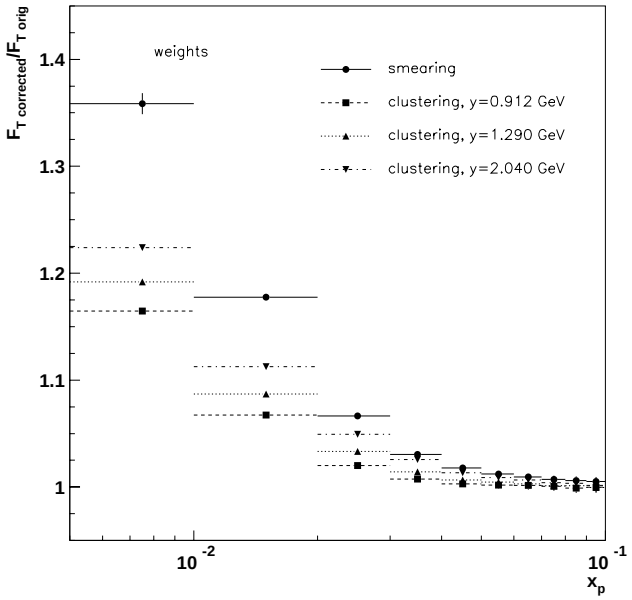

Figure 4.37. Ratio of F_T after the correction divided by F_T before the correction for the fragmentation effect. The correction was done for smearing and for the three cases of clustering. The extraction of F_T was done using weights.

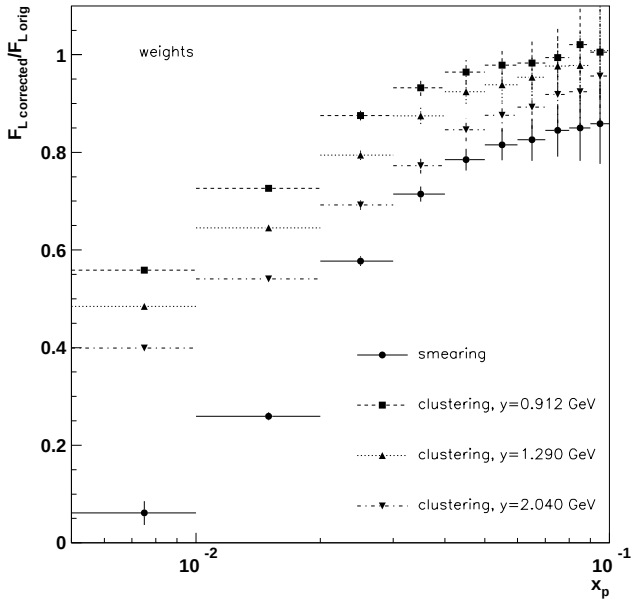

Figure 4.38. Ratio of F_L after the correction divided by F_L before the correction for the fragmentation effect. The correction was done for smearing and for the three cases of clustering. The extraction of F_L was done using weights.

4.9 Systematic uncertainties

The systematic errors were estimated by varying the cuts for the track and event selection and by modifying the extraction methods for the sample of nominal cuts (Section 4.1).

First, the errors due to the cuts will be discussed. In order to estimate these errors, the 1995 sample was reprocessed six times, each reprocessing entailing the variation of one selection cut as follows:

- run 1: track polar angle between 25° and 155°,
- run 2: track polar angle between 18° and 162°,
- run 3: track momentum above 0.2 GeV,
- run 4: track impact parameter in z below 5 cm / sinθ,
- run 5: track impact parameter in Rϕ below 3 cm,
- run 6: sphericity axis polar angle between 40° and 140°.

For each of the runs above, the fragmentation function components were calculated by the weighting method, as described in Section 4.4. The difference of the components extracted for a given run from the components of the nominal cut sample (for 1995) is the systematic error related to the cut that was varied in this run. The systematic errors estimated from the six runs above are given in Table 4.2 for F_T and in Table 4.3 for F_L.

x_p	run 1	run 2	run 3	run 4	run 5	run 6
0.00 - 0.01	1.0	-.10	-3	-3	-2.0	-4
0.01 - 0.02	2.6	.9	-1.0	-2.3	-.5	-.7
0.02 - 0.03	2.9	2.0	.5	-.016	.5	1.9
0.03 - 0.04	2.1	1.1	.3	.023	.5	2.0
0.04 - 0.05	1.2	.4	-.5	-.7	-.28	-.21
0.05 - 0.06	1.5	1.0	.5	.4	.6	1.1
0.06 - 0.07	.6	.05	-.29	-.5	-.16	-.3
0.07 - 0.08	.24	-.022	-.4	-.4	-.3	-.11
0.08 - 0.09	.18	-.012	-.4	-.5	-.26	-.17
0.09 - 0.10	.05	-.23	-.5	-.6	-.4	-.6
0.10 - 0.12	.11	-.09	-.28	-.4	-.26	-.16
0.12 - 0.14	-.03	-.10	-.15	-.24	-.15	.15
0.14 - 0.16	-.10	-.15	-.20	-.26	-.16	-.4
0.16 - 0.18	.024	-.07	-.13	-.18	-.12	.23
0.18 - 0.20	-.05	-.10	-.12	-.15	-.11	-.11
0.20 - 0.25	-.13	-.15	-.15	-.17	-.14	.06
0.25 - 0.30	-.07	-.06	-.06	-.05	-.05	-.05
0.30 -0.40	-.03	-.03	-.026	-.020	-.025	-.10
0.40 -0.50	-.005	-.004	.003	.005	.004	.015
0.50 -0.60	-.0011	-.0024	.0006	.0003	-.0012	-.03
0.60 - 0.80	.0020	.003	.005	.006	.006	.03
0.80 - 1.00	-.0011	-.0006	-.0011	.0004	-.0007	.009

Table 4.2: Systematic errors of F_T from varying the selection cuts.

x_p	run 1	run 2	run 3	run 4	run 5	run 6
0.00 - 0.01	1.3	2.7	6	5	4	6
0.01 - 0.02	-1.7	.21	2.1	3	2.2	1.3
0.02 - 0.03	-2.2	-1.1	.4	.6	.7	-1.2
0.03 - 0.04	-2.2	-1.1	-.17	.07	-.028	-1.9
0.04 - 0.05	-1.4	-.6	.3	.4	.3	-.4
0.05 - 0.06	-1.5	-1.0	-.4	-.3	-.4	-1.2
0.06 - 0.07	-.8	-.17	.28	.4	.21	-.10
0.07 - 0.08	-.5	-.12	.3	.3	.27	-.13
0.08 - 0.09	-.5	-.21	.17	.22	.10	-.18
0.09 - 0.10	-.4	-.04	.25	.29	.21	.11
0.10 -0.12	-.4	-.17	.08	.11	.06	-.16
0.12 -0.14	-.18	-.06	.07	.10	.06	-.26
0.14 - 0.16	-.10	-.006	.10	.13	.07	.10
0.16 -0.18	-.16	-.05	.05	.06	.029	-.26
0.18 - 0.20	-.08	-.005	.05	.06	.04	-.018
0.02 - 0.25	-.005	.04	.07	.08	.06	-.11
0.25 - 0.30	-.005	.004	.021	.012	.015	-.010
0.30 - 0.40	-.009	.0021	.008	.004	.007	.04
0.40 - 0.50	-.010	-.007	-.007	-.009	-.008	-.020
0.50 - 0.60	-.0013	.0008	.0010	.0016	.0021	.021
0.60 - 0.80	-.0028	-.003	-.004	-.004	-.004	-.020
0.80 - 1.00	.00012	-.00022	.00024	-.0007	-.0003	-.007

Table 4.3: Systematic errors of F_L from varying the selection cuts.

The systematic errors introduced by the method of extraction of the components of the fragmentation function were calculated from

- the difference between fits and weights,
- variations of the range of the cosθ values used in the extraction and
- the removal of central points in the cosθ distributions.

For these errors, the complete data sample was used. For the first error, the differences were taken between F_T and F_L from weights and F_T and F_L from fits, as they were calculated in Section 4.4 and in Section 4.5. The results are given in the first column of Table 4.4 and Table 4.5. For the second error, calculations by weights were used. Each calculation corresponded to a different value of $v = |\cos\theta|_{max}$, with v=0.85 being the value of the reference sample. Three other values for v were used: 0.9, 0.8 and 0.75. The differences of F_T and F_L obtained from the reference sample minus F_T and F_L obtained from the three other samples gave three errors for the three variations of v. The average value of the three errors (absolute values) was calculated as the systematic error due to the variation of v. The three individual errors are given in columns 3-5 of Table 4.4 and Table 4.5, whereas the average error is given in the next column.

The removal of central points in the cosθ distributions was artificially performed as follows. The cosθ distributions were first fitted with the four central points excluded from the fit. Then the values of the data in the four central bins were replaced by the corresponding values of the fitted function. The weighting method was subsequently applied to the modified cosθ distributions to extract new values for F_T and F_L. These new values were subtracted from the values of the reference sample giving the errors for the exclusion of the central points in the cosθ distributions (last column in Table 4.4 and Table 4.5).

4.10 First results

The fragmentation function components before and after the correction by clustering are given in Table 4.6 and Table 4.7. In the following, and unless otherwise stated, the first error quoted is the statistical error and the second error quoted is the systematic error.

As was explained in Appendix D, there is no ideal value for the clustering cut-off, as it is not precisely known at which scale the hadronization process starts. Therefore, there is no unique answer for the helicity components of the fragmentation function, rather a scale-dependent answer is considered.

As the results presented in this section involve a rather substantial correction which relies on the JETSET generator, an effort was made to extract the same information, the corrected functions, directly from data. This is described in the following section.

x_p	$F_{T,weights} - F_{T,fit}$	$F_{T,v=0.85} - F_{T,v=0.9}$	$F_{T,v=0.85} - F_{T,v=0.8}$	$F_{T,v=0.85} - F_{T,v=0.75}$	average for v	central points
0.00 - 0.01	1.5	4	.4	-.07	1.4	2.3
0.01 - 0.02	-1.3	-.10	-1.3	.4	.6	-.05
0.02 - 0.03	-1.1	-.3	-1.8	.3	.8	-.20
0.03 - 0.04	-.8	-.29	-.8	.9	.7	-.18
0.04 - 0.05	-.5	-.07	.03	1.5	.5	-.16
0.05 - 0.06	-.4	-.11	-.012	1.1	.4	-.12
0.06 - 0.07	-.3	-.13	.09	1.3	.5	-.17
0.07 - 0.08	-.17	-.24	.18	.9	.4	-.04
0.08 - 0.09	-.19	-.10	.07	.7	.28	-.05
0.09 - 0.10	-.03	.07	.16	.7	.3	.05
0.10 - 0.12	-.11	.07	-.17	-.025	.09	.04
0.12 - 0.14	-.05	.004	-.06	.08	.05	.05
0.14 - 0.16	-.06	.0024	-.017	.15	.06	.005
0.16 - 0.18	-.06	.04	-.05	-.009	.03	.010
0.18 - 0.20	-.05	.0016	-.03	-.011	.015	.008
0.20 - 0.25	-.023	.0017	-.018	.05	.023	.008
0.25 - 0.30	-.019	.006	-.020	-.023	.016	.0026
0.30 - 0.40	-.012	.007	-.003	.018	.009	-.0022
0.40 - 0.50	-.0011	.0013	-.0003	.017	.006	.0009
0.50 - 0.60	.0017	-.009	.006	.020	.011	.0008
0.60 - 0.80	.0004	-.005	.004	.010	.006	-.0008
0.80 - 1.00	.0007	-.004	.0016	.004	.003	-.0004

Table 4.4: Systematic errors of F_T due to the extraction method.

x_p	$F_{L,weights} - F_{L,fit}$	$F_{L,v=0.85} - F_{L,v=0.9}$	$F_{L,v=0.85} - F_{L,v=0.8}$	$F_{L,v=0.85} - F_{L,v=0.75}$	average for v	central points
0.00 - 0.01	-2.3	-2.6	-.24	.06	1.0	-2.9
0.01 - 0.02	1.1	.05	.9	-.21	.4	.08
0.02 - 0.03	1.0	.20	1.2	-.15	.5	.26
0.03 - 0.04	.7	.19	.5	-.5	.4	.23
0.04 - 0.05	.5	.04	-.013	-1.0	.3	.21
0.05 - 0.06	.4	.07	.014	-.7	.25	.16
0.06 - 0.07	.3	.08	-.06	-.8	.3	.21
0.07 - 0.08	.16	.16	-.11	-.6	.28	.05
0.08 - 0.09	.17	.06	-.04	-.4	.18	.06
0.09 - 0.10	.004	-.05	-.10	-.5	.21	-.06
0.10 -0.12	.06	-.05	.11	.024	.06	-.06
0.12 -0.14	.016	-.004	.04	-.05	.03	-.06
0.14 - 0.16	.05	-.0029	.012	-.09	.04	-.006
0.16 -0.18	.04	-.03	.03	.009	.024	-.012
0.18 - 0.20	.03	-.0019	.023	.010	.011	-.010
0.02 - 0.25	.015	-.0017	.013	-.03	.015	-.010
0.25 - 0.30	.014	-.004	.013	.016	.011	-.003
0.30 - 0.40	.010	-.005	.0023	-.011	.006	.0028
0.40 - 0.50	.0007	-.0009	.0003	-.011	.004	-.0012
0.50 - 0.60	-.0014	.006	-.004	-.012	.007	-.0010
0.60 - 0.80	.0003	.003	-.0027	-.007	.004	.0010
0.80 - 1.00	-.00020	.0028	-.0010	-.0024	.0021	.0005

Table 4.5: Systematic errors of F_L due to the extraction method.

x_p	F_T uncorrected	F_T (y=0.912 GeV)	F_T (y=1.290 GeV)	F_T (y=2.040 GeV)
0.00-0.01	279.8 ± .4 ± 7.2	325.8 ± .6 ± 7.4	333.5 ± .6 ± 7.5	342.4 ± .6 ± 7.6
0.01-0.02	323.8 ± .4 ± 4.1	345.5 ± .5 ± 4.1	351.9 ± .5 ± 4.1	360.2 ± .5 ± 4.2
0.02-0.03	226.15 ± .30 ± 4.27	230.7 ± .4 ± 4.3	233.7 ± .4 ± 4.3	237.3 ± .4 ± 4.3
0.03-0.04	165.51 ± .25 ± 3.35	166.8 ± .4 ± 3.4	167.8 ± .4 ± 3.4	169.8 ± .4 ± 3.4
0.04-0.05	125.39 ± .21 ± 1.69	125.8 ± .3 ± 1.7	126.2 ± .3 ± 1.7	127.1 ± .3 ± 1.7
0.05-0.06	98.07 ± .19 ± 2.36	98.24 ± .26 ± 2.37	98.53 ± .26 ± 2.37	98.95 ± .26 ± 2.37
0.06-0.07	78.91 ± .17 ± 1.06	79.02 ± .24 ± 1.07	79.15 ± .24 ± 1.07	79.43 ± .24 ± 1.07
0.07-0.08	64.65 ± .15 ± .86	64.69 ± .21 ± .87	64.73 ± .21 ± .87	64.92 ± .21 ± .87
0.08-0.09	53.80 ± .14 ± .77	53.74 ± .19 ± .78	53.87 ± .19 ± .78	53.99 ± .19 ± .78
0.09-0.10	45.48 ± .13 ± 1.12	45.47 ± .18 ± 1.12	45.45 ± .18 ± 1.12	45.54 ± .18 ± 1.12
0.10-0.12	35.74 ± .08 ± .59	35.72 ± .11 ± .59	35.74 ± .11 ± .59	35.83 ± .11 ± .59
0.12-0.14	26.86 ± .07 ± .37	26.85 ± .10 ± .38	26.87 ± .10 ± .38	26.90 ± .10 ± .38
0.14-0.16	20.54 ± .06 ± .55	20.55 ± .08 ± .56	20.57 ± .08 ± .56	20.60 ± .08 ± .56
0.16-0.18	16.10 ± .05 ± .35	16.12 ± .08 ± .36	16.12 ± .08 ± .36	16.13 ± .08 ± .36
0.18-0.20	12.73 ± .05 ± .27	12.73 ± .07 ± .27	12.74 ± .07 ± .27	12.76 ± .07 ± .27
0.20-0.25	8.727 ± .025 ± .340	8.72 ± .03 ± .34	8.73 ± .03 ± .34	8.74 ± .03 ± .34
0.25-0.30	5.323 ± .019 ± .143	5.321 ± .027 ± .144	5.321 ± .027 ± .144	5.323 ± .027 ± .144
0.30-0.40	2.710 ± .010 ± .113	2.709 ± .014 ± .114	2.709 ± .014 ± .114	2.709 ± .014 ± .114
0.40-0.50	1.147± .007± .019	1.147± .009± .020	1.147± .009± .020	1.149± .009± .020
0.50-0.60	.503 ± .004 ± .034	.504 ± .006 ± .034	.503 ± .006 ± .034	.502 ± .006 ± .034
0.60-0.80	.1598±.0018± .0320	.1597± .0023± .0320	.1598± .0023± .0320	.1599± .0023± .0320
0.80-1.00	.0227±.0007±.0098	.0227±.0008±.0098	.0227±.0008±.0098	.0227±.0008±.0098

Table 4.6: F_T from original data and corrected for the three values of the clustering cut-off (simulation correction).

x_p	F_L uncorrected	F_L (y=0.912 GeV)	F_L (y=1.290 GeV)	F_L (y=2.040 GeV)
0.00-0.01	104.46 ± .3 ± 11.4	58.3 ± 0.4 ± 11.5	50.6 ± 0.4 ± 11.6	41.7 ± 0.4 ± 11.6
0.01-0.02	79.37 ± .28 ± 5.00	57.7 ± .4 ± 5.0	51.2 ± .4 ± 5.0	42.9 ± 0.4 ± 5.0
0.02-0.03	36.80 ± .22 ± 3.13	32.2 ± .3 ± 3.1	29.2 ± .3 ± 3.1	25.5 ± .3 ± 3.1
0.03-0.04	18.66 ± .19 ± 3.27	17.40 ± .26 ± 3.28	16.32 ± .26 ± 3.28	14.41 ± .26 ± 3.28
0.04-0.05	11.07 ± .16 ± 1.78	10.68 ± .23 ± 1.79	10.23 ± .23 ± 1.79	9.37 ± .23 ± 1.79
0.05-0.06	6.91 ± .14 ± 2.27	6.77 ± .20 ± 2.28	6.49 ± .20 ± 2.28	6.06 ± .20 ± 2.28
0.06-0.07	4.69 ± .13 ± 1.06	4.61 ± .18 ± 1.07	4.47 ± .18 ± 1.07	4.18 ± .18 ± 1.07
0.07-0.08	3.26 ± .11 ± .82	3.25 ± .16 ± .83	3.19 ± .16 ± .83	3.00 ± .16 ± .83
0.08-0.09	2.44 ± .10 ± .69	2.49 ± .15 ± .70	2.39 ± .15 ± .70	2.26 ± .15 ± .70
0.09-0.10	1.71 ± .10 ± .62	1.72 ± .13 ± .63	1.72 ± .13 ± .63	1.64 ± .13 ± .63
0.10-0.12	1.30 ± .06 ± .50	1.31 ± .08 ± .50	1.29 ± .08 ± .50	1.21 ± .08 ± .50
0.12-0.14	.67 ± .05 ± .36	.69 ± .07 ± .36	.67 ± .07 ± .36	.63 ± .07 ± .36
0.14-0.16	.47 ± .05 ± .23	.47 ± .06 ± .24	.45 ± .06 ± .24	.43 ± .06 ± .24
0.16-0.18	.25 ± .04 ± .33	.24 ± .06 ± .33	.23 ± .06 ± .33	.23 ± .06 ± .33
0.18-0.20	.19 ± .04 ± .13	.19 ± .05 ± .13	.18 ± .05 ± .13	.17 ± .05 ± .13
0.20-0.25	.116 ± .018 ± .170	.119 ± .026 ± .171	.117 ± .026 ± .171	.106 ± .026 ± .171
0.25-0.30	.010 ± .014 ± .036	.012 ± .020 ± .038	.012 ± .020 ± .038	.009 ± .020 ± .038
0.30-0.40	.021 ± .007 ± .045	.022 ± .010 ± .045	.022 ± .010 ± .045	.021 ± .010 ± .045
0.40-0.50	.004 ± .005 ± .028	.004 ± .007 ± .028	.004 ± .007 ± .028	.002 ± .007 ± .028
0.50-0.60	.000 ± .003 ± .022	-.000 ±.004 ± .022	.000 ± .004 ± .022	.000 ± .004 ± .022
0.60-0.80	-.0060±.0013±.0223	-.0060±.0017±.0223	-.0060±.0017±.0223	-.0062±.0017±.0223
0.80-1.00	-.0035±.0005±.0070	-.0035±.0006±.0070	-.0035±.0006±.0070	-.0035±.0006±.0070

Table 4.7: F_L from original data and corrected for the three values of the clustering cut-off (simulation correction).

4.11 Clustering data

To avoid a model-dependent correction on the measurement of the fragmentation function components, the data was reprocessed to apply the clustering directly on the measured particles. The clustering was performed by the same algorithm and for the same values of the cut-off parameter as discussed in Section 4.8. For each clustering parameter, the helicity components of the fragmentation function were extracted by weights and fits from the clustered distributions of cosθ.

An example of correction factors (for 1994) and cross sections (for all data) is given in Fig. 4.39 and Fig. 4.40, respectively. The first row in the figures shows factors and cross sections for the first momentum bin. The second row corresponds to the tenth momentum bin. The plots (a) and (d) correspond to the lowest clustering cut-off, whereas the plots (b) and (e) correspond to the cut-off value of y=1.290 GeV. The plots (c) and (f) show the factors and cross sections for y=2.040 GeV. There is a smoothening effect in the factors induced by the clustering in the lowest momentum bin. This effect cannot be seen in the tenth momentum bin. Apart from this effect, there is no difference in the correction factors as y varies, as expected. The cross sections are also smoother if compared to the non-clustered data (Fig. 4.6).

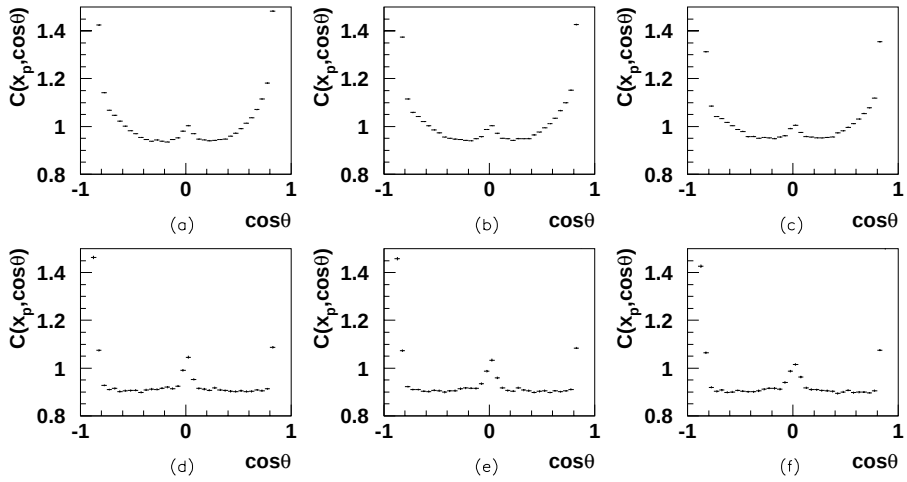

Figure 4.39. Correction factors for clustered data (1994): (a)-(c) x_p from 0 to 0.01, (d)-(f) x_p from 0.09 to 0.1. Plots (a) and (d) correspond to the lowest Durham cut-off value, y=0.912 GeV. In plots (b) and (e), y=1.290 GeV, whereas (c) and (f) have y=2.040 GeV.

The fragmentation function components for the three clustering cut-offs are shown in Fig. 4.41 - Fig. 4.44. The first two figures show calculation by weights and the other two figures show results from fits. The agreement with the Monte Carlo corrected functions is good. So far, comparisons have been performed between measured functions and simulated functions but also between functions corrected by simulation and functions extracted by directly clustering the data. The agreement in all cases has been very good. This shows that both the detector simulation and the event generator are very good. This gives confidence to the measurement of the helicity components presented in this report, so that one can use them to extract information about the strong coupling constant or the gluon fragmentation function. Only the former will be addressed in Section 4.12.

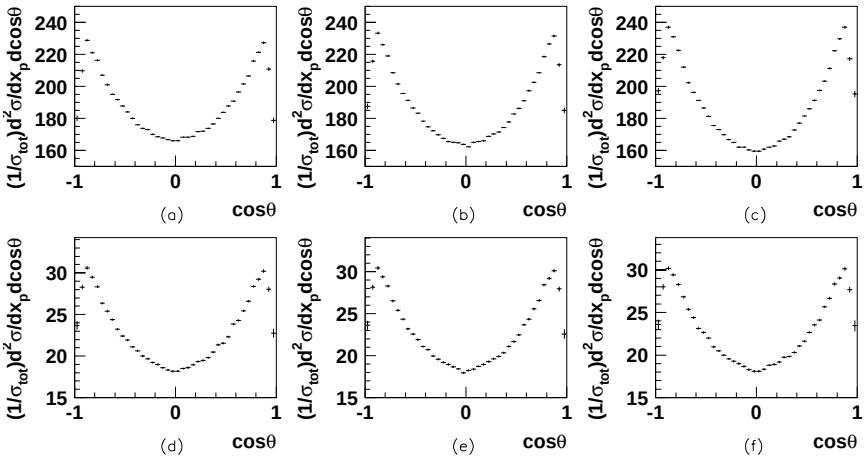

Figure 4.40. Cross sections for clustered data (1994): (a)-(c) x_p from 0 to 0.01, (d)-(f) x_p from 0.09 to 0.1. Plots (a) and (d) correspond to the lowest Durham cut-off value, y=0.912 GeV. In plots (b) and (e), y=1.290 GeV, whereas (c) and (f) have y=2.040 GeV.

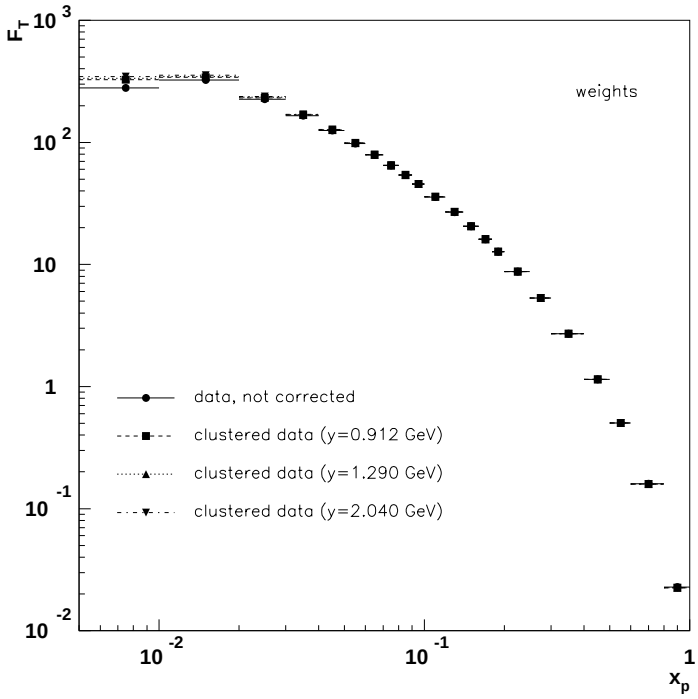

Figure 4.41. F_T from original data and F_T from clustered data. The weighting method has been applied to both samples. The clustered components are given for three values of the cut-off parameter, y, for the Durham clustering algorithm.

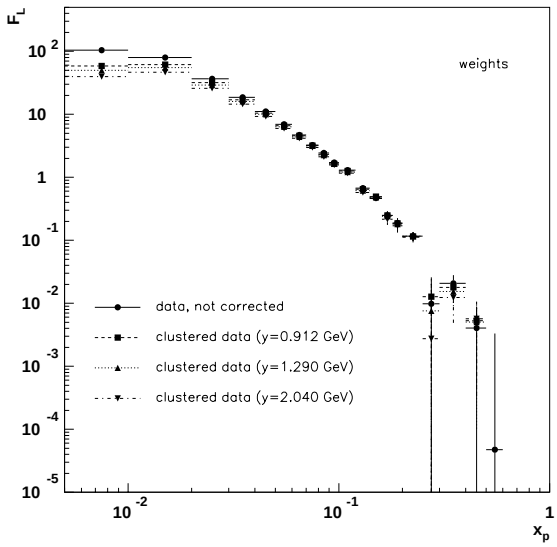

Figure 4.42. F_L from original data and F_L from clustered data. The weighting method has been applied to both samples. The clustered components are given for three values of the cut-off parameter, y, for the Durham clustering algorithm.

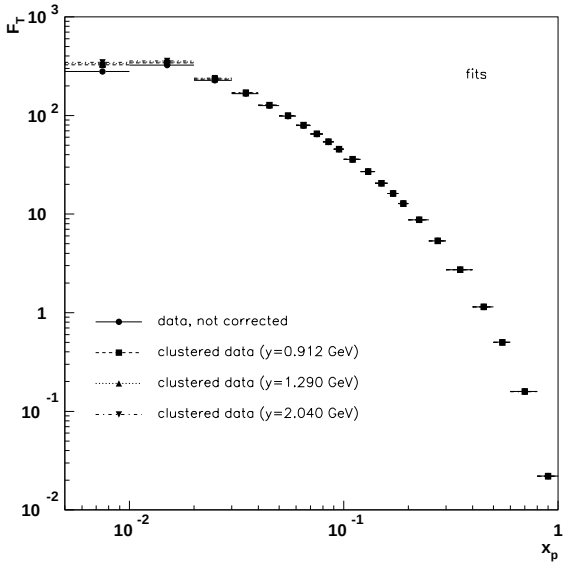

Figure 4.43. F_T from original data and F_T from clustered data. The fitting method has been applied to both samples. The clustered components are given for three values of the cut-off parameter, y, for the Durham clustering algorithm.

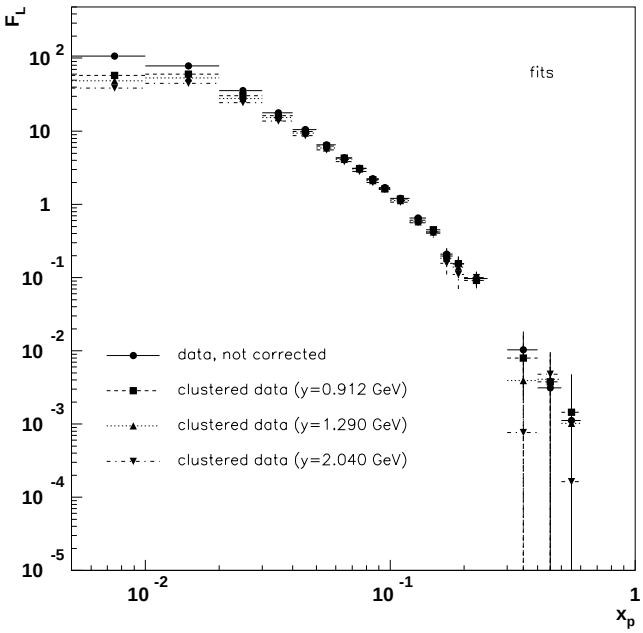

Figure 4.44. F_L from original data and F_L from clustered data. The fitting method has been applied to both samples. The clustered components are given for three values of the cut-off parameter, y, for the Durham clustering algorithm.

x_p	F_T (y=0.912 GeV)	F_T (y=1.290 GeV)	F_T (y=2.040 GeV)
0.00-0.01	326.2 ± 0.5 ± 7.1	335.3 ± 0.5 ± 8.9	345.9 ± 0.5 ± 11.2
0.01-0.02	340.5 ± 0.4 ± 9.3	346.7 ± 0.4 ± 9.7	355.0 ± 0.5 ± 10.4
0.02-0.03	231.3 ± 0.3 ± 4.1	233.7 ± 0.3 ± 4.7	237.0 ± 0.3 ± 5.1
0.03-0.04	167.41 ± 0.26 ± 2.59	168.36 ± 0.28 ± 2.73	169.75 ± 0.28 ± 3.04
0.04-0.05	126.15 ± 0.23 ± 2.11	126.60 ± 0.23 ± 2.46	127.30 ± 0.24 ± 3.22
0.05-0.06	98.45 ± 0.20 ± 2.21	98.79 ± 0.20 ± 2.17	99.11 ± 0.20 ± 2.14
0.06-0.07	79.06 ± 0.18 ± 1.27	79.26 ± 0.18 ± 1.74	79.50 ± 0.18 ± 1.83
0.07-0.08	64.78 ± 0.16 ± 1.23	64.81 ± 0.16 ± 1.03	64.97 ± 0.16 ± 1.30
0.08-0.09	53.94 ± 0.15 ± 0.75	54.03 ± 0.15 ± 0.78	54.18 ± 0.15 ± 0.87
0.09-0.10	45.57 ± 0.13 ± 1.00	45.57 ± 0.14 ± 1.01	45.61 ± 0.14 ± 0.80
0.10-0.12	35.77 ± 0.08 ± 0.45	35.83 ± 0.08 ± 0.44	35.89 ± 0.08 ± 0.46
0.12-0.14	26.89 ± 0.07 ± 0.27	26.92 ± 0.07 ± 0.29	26.97 ± 0.07 ± 0.24
0.14-0.16	20.49 ± 0.06 ± 0.69	20.51 ± 0.06 ± 0.48	20.53 ± 0.06 ± 0.36
0.16-0.18	16.09 ± 0.06 ± 0.37	16.10 ± 0.06 ± 0.39	16.13 ± 0.06 ± 0.22
0.18-0.20	12.71 ± 0.05 ± 0.17	12.72 ± 0.05 ± 0.17	12.73 ± 0.05 ± 0.26
0.20-0.25	8.716 ± 0.025 ± 0.279	8.715 ± 0.026 ± 0.255	8.722 ± 0.026 ± 0.292
0.25-0.30	5.311 ± 0.019 ± 0.127	5.319 ± 0.020 ± 0.115	5.328 ± 0.020 ± 0.181
0.30-0.40	2.709 ± 0.009 ± 0.070	2.713 ± 0.010 ± 0.050	2.717 ± 0.010 ± 0.061
0.40-0.50	1.142 ± 0.007 ± 0.049	1.142 ± 0.007 ± 0.039	1.142 ± 0.007 ± 0.041
0.50-0.60	0.502 ± 0.005 ± 0.049	0.503 ± 0.005 ± 0.085	0.502 ± 0.005 ± 0.096
0.60-0.80	0.1593± 0.0018 ± 0.0384	0.1591 ± 0.0018 ± 0.0366	0.1588 ± 0.0018 ± 0.0348
0.80-1.00	0.0225± 0.0007 ± 0.0084	0.0226 ± 0.0007 ± 0.0088	0.0226 ± 0.0007 ± 0.0100

Table 4.8: F_T from clustered data for the three values of Durham cut-off.

x_p	F_L (y=0.912 GeV)	F_L (y=1.290 GeV)	F_L (y=2.040 GeV)
0.00-0.01	58.6 ± 0.4 ± 8.6	49.8 ± 0.4 ± 7.5	39.5 ± 0.4 ± 6.9
0.01-0.02	61.3 ± 0.3 ± 9.3	55.0 ± 0.3 ± 9.4	46.5 ± 0.3 ± 9.5
0.02-0.03	31.87 ± 0.24 ± 4.04	29.27 ± 0.25 ± 4.63	25.87 ± 0.25 ± 4.92
0.03-0.04	16.96 ± 0.20 ± 2.65	16.00 ± 0.21 ± 2.51	14.51 ± 0.21 ± 2.61
0.04-0.05	10.43 ± 0.17 ± 2.00	9.98 ± 0.17 ± 2.06	9.24 ± 0.18 ± 2.43
0.05-0.06	6.62 ± 0.15 ± 2.12	6.31 ± 0.15 ± 2.04	5.97 ± 0.15 ± 1.99
0.06-0.07	4.56 ± 0.13 ± 1.30	4.40 ± 0.13 ± 1.60	4.16 ± 0.14 ± 1.66
0.07-0.08	3.18 ± 0.12 ± 1.01	3.14 ± 0.12 ± 0.97	2.98 ± 0.12 ± 1.09
0.08-0.09	2.33 ± 0.11 ± 0.84	2.25 ± 0.11 ± 0.92	2.12 ± 0.11 ± 0.91
0.09-0.10	1.64 ± 0.10 ± 0.81	1.63 ± 0.10 ± 0.75	1.58 ± 0.10 ± 0.68
0.10-0.12	1.27 ± 0.06 ± 0.59	1.21 ± 0.06 ± 0.66	1.16 ± 0.06 ± 0.63
0.12-0.14	0.64 ± 0.05 ± 0.39	0.62 ± 0.05 ± 0.44	0.58 ± 0.05 ± 0.34
0.14-0.16	0.50 ± 0.05 ± 0.33	0.48 ± 0.05 ± 0.24	0.46 ± 0.05 ± 0.26
0.16-0.18	0.25 ± 0.04 ± 0.38	0.24 ± 0.04 ± 0.40	0.22 ± 0.04 ± 0.31
0.18-0.20	0.19 ± 0.04 ± 0.12	0.18 ± 0.04 ± 0.16	0.17 ± 0.04 ± 0.13
0.20-0.25	0.116 ± 0.019 ± 0.133	0.116 ± 0.019 ± 0.135	0.112 ± 0.019 ± 0.177
0.25-0.30	0.013 ± 0.015 ± 0.057	0.008 ± 0.015 ± 0.056	0.003 ± 0.015 ± 0.063
0.30-0.40	0.018 ± 0.007 ± 0.022	0.015 ± 0.007 ± 0.036	0.012 ± 0.008 ± 0.042
0.40-0.50	0.005 ± 0.005 ± 0.048	0.005 ± 0.005 ± 0.042	0.006 ± 0.005 ± 0.026
0.50-0.60	-0.000 ± 0.003 ± 0.032	-0.001 ± 0.003 ± 0.056	-0.000 ± 0.003 ± 0.063
0.60-0.80	-0.0061±0.0013 ± 0.0265	-0.0060±0.0013 ± 0.0254	-0.0057± 0.0013± 0.0241
0.80-1.00	-0.0035 ±0.0005± 0.0059	-0.0034±0.0005±0.0060	-0.0034±0.0005 ±0.0069

Table 4.9: F_L from clustered data for the three values of Durham cut-off

4.12 The strong coupling constant

The strong coupling constant was extracted from the F_L distributions presented in the previous section, using Eq. 3.10. As this relation implies that both charged and neutral particles have been included in the analysis, a correction was required for having neglected the neutral ones. This correction was obtained by using the tuned simulation to calculate the ratio of (the normalized to the total cross section) σ_L for all particles divided by σ_L for charged particles only. The calculation was done for no fragmentation correction and for the three cut-off values of the clustering. The results are given in Table 4.10.

The normalized longitudinal cross sections from the data were corrected by multiplication with the correction factor of Table 4.10. The cross sections before and after the correction for the neutral particles is given in Table 4.11. In the last column of the table, the corresponding values of the strong coupling constant are given.

y cut-off value	$\sigma_{L,\,all}$	$\sigma_{L,\,charged}$	$\sigma_{L,\,charged}/\sigma_{L,\,all}$
-	0.060 ± 0.009	0.034 ± 0.003	0.567 ± 0.050
0.912 GeV	0.055 ± 0.006	0.0306 ± 0.0022	0.556 ± 0.040
1.290 GeV	0.053 ± 0.005	0.0292 ± 0.0019	0.551 ± 0.036
2.040 GeV	0.049 ± 0.005	0.0268 ± 0.0017	0.547 ± 0.035

Table 4.10: Correction factor for neglecting the neutral particles in the analysis. The cross sections have been calculated using the tuned simulation.

y cut-off value	$\sigma_{L,\,charged}$	$(\sigma_{L,\,charged})^{\mathbf{corrected}}$	α_s
-	0.030 ± 0.004 ± 0.004	0.053 ± 0.008 ± 0.009	0.125 ± 0.014 ± 0.017
0.912 GeV	0.0263 ± 0.0024 ± 0.0039	0.047 ± 0.006 ± 0.008	0.114 ± 0.011 ± 0.015
1.290 GeV	0.0246 ± 0.0021 ± 0.0039	0.045 ± 0.005 ± 0.008	0.109 ± 0.010 ± 0.015
2.040 GeV	0.0223 ± 0.0018 ± 0.0038	0.041 ± 0.004 ± 0.007	0.101 ± 0.009 ± 0.015

Table 4.11: Longitudinal cross sections from data and the strong coupling constant.

To estimate whether there is a significant dependence of the calculation of σ_L on the clustering algorithm, simulated events where clustered using the JADE algorithm [31] instead of Durham. This was done for a sample of 5 million events generated with the tuned generator. The clustering cut-off for Jade was selected so as to give approximately the same mean cluster multiplicity as the second Durham cut-off (y_{Durham}=1.290 GeV). This was found to be 2.192 GeV giving a mean number of clusters equal to 5.164 ± 0.001 (to be compared with 5.162 ± 0.001 clusters for Durham). The calculated σ_L for JADE was 0.0303 ± 0.0024 to be compared with 0.0292 ± 0.0019 for Durham (Table 4.10). This shows that the analysis is not sensitive to the choice of the clustering algorithm.

The strong coupling constant values given in Table 4.11 are somewhat low in comparison with the values obtained in scaling violation or jet rate measurements. Measurements from event shape distributions also gave a slightly higher value [33].

The previously published DELPHI result for the measurement of fragmentation functions, based on a smaller data sample, gave [23]:

$$\alpha_s = 0.101 \pm 0.002\,(stat) \pm 0.013\,(syst) + 0.007\,(scale) \qquad (4.24)$$

In Eq. 4.24, it was assumed that the average value of x_p in each bin was known precisely. In Table 4.10 and Table 4.11, however, more conservative results are given, which have been calculated assuming that the average value of x_p in each bin is uncertain by half the bin width. If no error had been taken into account for x_p, the results of Table 4.10 and Table 4.11 would have been as given in Table 4.12 and Table 4.13.

y cut-off value	$\sigma_{L,\,all}$	$\sigma_{L,\,charged}$	$\sigma_{L,\,charged}/\sigma_{L,\,all}$
-	0.0600 ± 0.0002	0.0339 ± 0.0002	0.5650 ± 0.0033
0.912 GeV	0.0549 ± 0.0002	0.0307 ± 0.0002	0.5592 ± 0.0036
1.290 GeV	0.0528 ± 0.0002	0.0292 ± 0.0002	0.5530 ± 0.0038
2.040 GeV	0.0492 ± 0.0002	0.0268 ± 0.0002	0.5447 ± 0.0041

Table 4.12: Correction factor for neglecting the neutral particles in the analysis. The cross sections have been calculated using the tuned simulation. The average value of x_p in each bin was assumed to be known precisely.

y cut-off value	$\sigma_{L,\,charged}$	$(\sigma_{L,\,charged})^{corrected}$	α_s
-	0.0300 ± 0.0003 ± 0.0027	0.0531 ± 0.0006 ± 0.0048	0.1249 ± 0.0011 ± 0.0090
0.912 GeV	0.0263 ± 0.0003 ± 0.0031	0.0470 ± 0.0006 ± 0.0056	0.1132 ± 0.0012 ± 0.0109
1.290 GeV	0.0246 ± 0.0003 ± 0.0033	0.0445 ± 0.0006 ± 0.0060	0.1083 ± 0.0012 ± 0.0119
2.040 GeV	0.0223 ± 0.0003 ± 0.0034	0.0409 ± 0.0006 ± 0.0062	0.1010 ± 0.0012 ± 0.0126

Table 4.13: Longitudinal cross sections from data and the strong coupling constant. The average value of x_p in each bin was assumed to be known precisely.

As is discussed in Appendix D, clustering at parton and hadron level showed the best agreement for a 'clustering' scale around 1.3 GeV and therefore the corresponding value of α_s might be considered as a preferred value. However, it should perhaps be mentioned again that this value depends on the model and should be treated carefully. Therefore, a more conservative approach would be to consider the spread of the values of α_s obtained for the different clustering cut-off values as an uncertainty steming from the hadronization correction procedure.

4.13 Summary

The fragmentation function analysis presented in this report concentrates on the extraction of the transverse and longitudinal components of the fragmentation function and the hadronization correction required. The analysis has shown that the hadronization correction is mostly important for the longitudinal component and at low momentum values.

Two methods for the hadronization correction of the fragmentation function components have been considered. The first method, consists in simulating a symmetric smearing around the directions of the primary quark-antiquark pair. This correction is however exaggerated as it ignores the string effect.

The second correction is a more realistic one, as it takes into account the string picture. A clustering of the particles is introduced in order to bring the event backwards in time, namely approximately at the moment where the non-perturbative regime begins. This strategy has been applied both in terms of a Monte Carlo correction and directly to the data. The two results showed nice agreement. The clustering method therefore seems to be a good approach for accounting for hadronization. However, it introduces an uncertainty in the cut-off scale itself. A reasonable range of scales has therefore been selected.

The corrected longitudinal component of the fragmentation function was used to extract the strong coupling constant. As the fragmentation functions depend on the cut-off scale of the clustering, this implies an uncertainty for the value of α_s. The preferred cut-off value for y gives

$$\alpha_s = 0.109 \pm 0.010 \pm 0.015 \qquad (4.25)$$

Using fixed values for x_p as in the previously published analysis, Eq. 4.24, this new analysis would give

$$\alpha_s = 0.1083 \pm 0.0012 \pm 0.0119 \qquad (4.26)$$

ACKNOWLEDGEMENTS

It is impossible to mention here all the people that have helped me during my studies. I will therefore mention here only a few.

First of all, I would like to thank my supervisors, Sissi Rinaudo, Bengt Lörstad, Sverker Almehed and Oxana Smirnova for their help and guidance and Göran Jarlskog for the opportunity to work with the DELPHI experiment. The financial support I have received from NFR and Lund University is gratefully acknowledged.

The VSAT group members deserve a special mention for helping me so much in the beginning of my studies and during my stationing at CERN. I would especially like to thank Sverker Almehed, Per Jonsson and Fabio Cossutti for patiently answering many questions.

Klaus Hamacher has been very helpful in discussing the QCD analysis. I also want to thank the rest of the members of the QCD team for their comments and suggestions.

Jon Guy was very kind to give me the simulation program that was used for the LEP1 production and to help me set it up on the CERN off-line cluster. Sverker Almehed ported the program to the HP's in Lund. I thank them both very much, the fragmentation corrections would have not been made without this simulation.

Fabio Cossutti, Ryszard Gokieli, Ulrich Schwickerath and Jan van Eldik have been very patient and generous with their time and help with the DELPHI software.

I would like to thank the people at the Theory Department for their kind help during the courses and for many and very helpful discussions, in particular Gösta Gustafson, who also helped me with the muon lab and Torbjörn Sjöstrand, who spent a lot of time and effort in the fragmentation function analysis.

I am grateful to Ulf Mjörnmark and Björn Lundberg for frequent emergency assistance with my PC.

Teaching at Kurslab was one of the most pleasant experiences I had in Lund. I am grateful to Per-Olof Zetterberg and Tomas Brage for receiving me in their group.

Lastly, I would like to thank my parents, though words are not enough for me to express my gratitude for their love and support during my long years of studying.

BIBLIOGRAPHY

[1] L. Arnaudon et al., Z. Phys. C66 (1995) 45.

[2] S. Myers, *The LEP collider*, excerpts from the John Adams Memorial Lecture, CERN, 26 November 1990.

[3] DELPHI Collaboration, *Performance of the DELPHI detector*, CERN-PPE/95-194.

[4] Ch. Jarlskog, *Luminosity measurement for the 1995 Z^0 scan with the Very Small Angle Tagger of DELPHI*, LUNFD6/(NFFL-7160) 1998, licentiate of philosophy thesis.

[5] DELPHI Collaboration, Phys. Lett. B241 (1990) 435.

[6] DELPHI Collaboration, Nucl. Phys. B367 (1991) 511.

[7] DELPHI Collaboration, Eur.Phys.J. C16, 371 (2000).

[8] DELPHI Collaboration, Phys. Lett. B241 (1990) 425.

[9] DELPHI Collaboration, Nucl. Phys. B417 (1994) 3.

[10] DELPHI Collaboration, *High precision relative luminosity measurement with a Very Small Angle Tagger (VSAT) in DELPHI*, DELPHI 92-77 PHYS 188.

[11] DELPHI Collaboration, *Improved measurements of cross sections and asymmetries at the Z^0 resonance*, CERN-PPE/94-31.

[12] The LEP Collaborations and the Line Shape Sub-group of the LEP Electroweak Working Group, *Combination procedure for the precise determination of Z boson parameters from results of the LEP experiments*, CERN-EP-2000-153.

[13] R. K. Ellis et al., *QCD and collider physics*, Cambridge Monographs on Particle Physics, Nuclear Physics and Cosmology, 1996.

[14] Y. L. Dokshitzer et al., *Basics of perturbative QCD*, Editions Frontieres, 1991.

[15] R. K. Ellis et al., Nucl. Phys. B178 (1981) 421.

[16] B. Andersson, *The Lund model*, Cambridge Monographs on Particle Physics, Nuclear Physics and Cosmology, 1998.

[17] T. Sjöstrand, Comp. Phys. Communications 39 (1986) 347; T. Sjöstrand and M. Bengtsson, Comp. Phys. Communications 43 (1987) 367; T. Sjöstrand, Comp. Phys. Communications 82 (1994) 74.

[18] P. Nason, B. R. Webber, Nucl. Phys. B421 (1994) 473.

[19] P. J. Rijken, W. L. van Neerven, Phys. Lett. B386 (1996) 422.

[20] DELPHI Collaboration, Z. Phys. C73, 11-59 (1996).

[21] J. Guy, private communication.

[22] O. Smirnova, Studies of the fragmentation process in hadronic decays of Z^0 boson, LUNFD6/(NFFL-7127) 1996, PhD thesis.

[23] DELPHI Collaboration, Eur. Phys. J. C6 (1999) 19.

[24] DELPHI Collaboration, *DELPHI ShortDST content*, DELPHI 97-146 PROG-221; http://delphiwww.cern.ch/~offline/data/data.html.

[25] F. Cossutti et al., *Improvements to SKELANA for version 2.0*, DELPHI 99-175 PROG 239.

[26] DELPHI Collaboration, Phys. Lett. B240 (1990) 271.

[27] DELPHI Collaboration, Phys. Lett. B311 (1993) 408.
[28] T. Sjöstrand, private communication.
[29] H. Georgi, H. D. Politzer, Nucl. Phys. B136 (1978) 445.
[30] B. Andersson et al., Phys. Lett. B94 (1980) 211; Y. I. Azimov et al., Phys. Lett. B165 (1985) 147.
[31] S. Moretti et al., *New and old jet clustering algorithms for electron-positron events*, hep-ph/9804296.
[32] L. Lyons, *Statistics for nuclear and particle physicists*, Cambridge University Press, 1999.
[33] DELPHI Collaboration, E. Phys. J. C14 (2000) 557.

Appendix A

DELPHI Collaboration

DELPHI 95-150 LEDI 2
27 September, 1995

Measurement of the beam parameter variations in DELPHI with the VSAT

S. Almehed[1], **F. Cossutti**[2], **Ch. Jarlskog**[1], **G. Jarlskog**[1], **P. Jonsson**[1], **P. Poropat**[2], **G. Rinaudo**[3], **E. Vallazza**[4]

Abstract

The beam parameter variations during 1994 data taking, obtained by the measurements of the Very Small Angle Tagger (VSAT) luminometer, are presented; a comparison with 1993 data is shown.

[1]Lund
[2]Trieste
[3]Torino
[4]CERN

1 Introduction

The Very Small Angle Tagger (VSAT) is an electromagnetic sampling calorimeter for the luminosity measurement in DELPHI. It consists of four rectangular modules placed symmetrically at about 7.7 m from the DELPHI origin, around a short elliptical section of the beam pipe behind the low beta superconducting quadrupoles (SCQ) as shown in fig. 1. The distance between two neighbouring modules is about 12 cm, corresponding to the smaller beam pipe dimension in that region. Since the physical process studied for the luminosity measurement is the Bhabha scattering, where electrons and positrons are emitted back to back, we use the coincidences of signals between a module in the forward region and a module in the backward region, thus defining two diagonals for the trigger: diagonal 1 (modules F1-B2) and diagonal 2 (modules F2-B1).

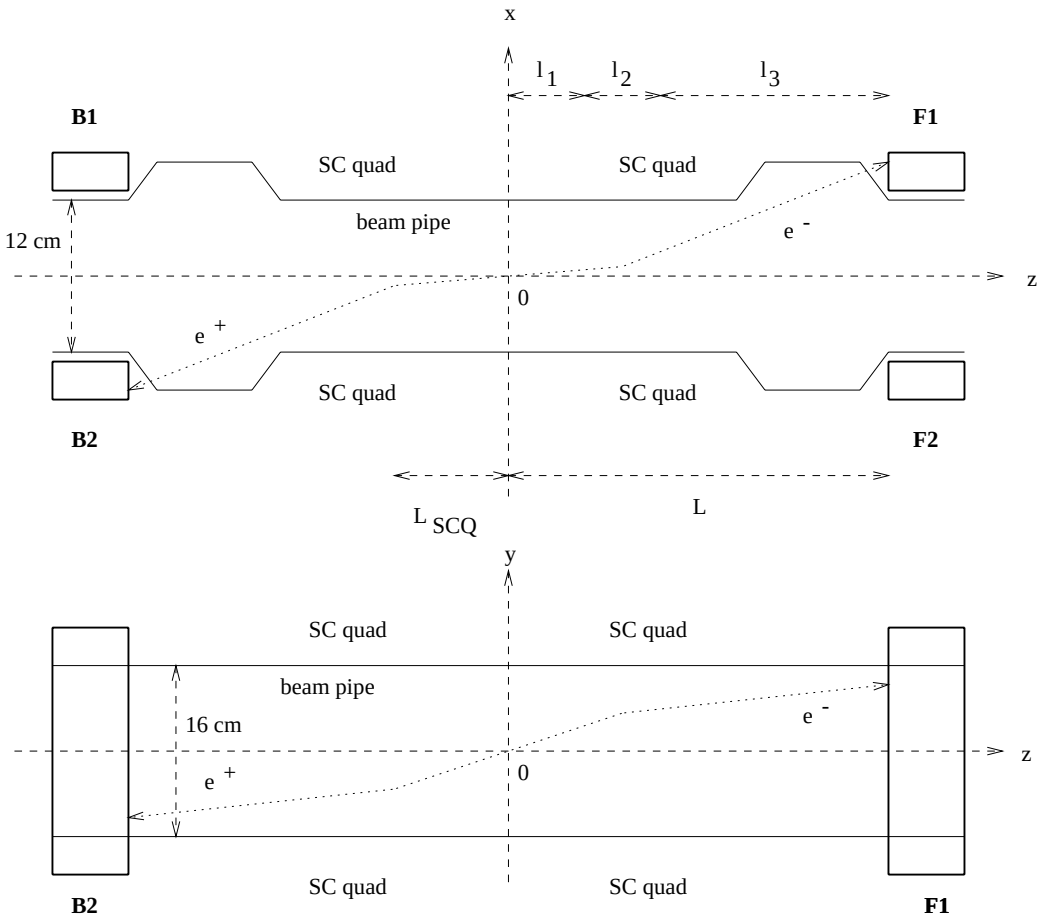

Figure 1: *Layout of the position of the VSAT modules in the (x,z) and (y,z) planes: the distance L_{SCQ} of the center of the superconducting quadrupoles from the DELPHI origin is about 4 m and the distance L of the front of the VSAT modules is about 7.7 m; the distances l_1, l_2 and l_3 define the three regions relevant to the beamspot equations.*

Each VSAT module contains 12 tungsten absorbers ($X_0 = 0.38$ cm) interspaced with 12 silicon planes (Full Area Detectors, (FAD)) for energy measurement (fig. 2). The

dimensions of the calorimeters are 3 cm in the transverse horizontal direction (x), 5 cm in the vertical direction (y) and 24 radiation lengths (about 10 cm) along the beam direction (z). The center of the electromagnetic shower is given by three silicon strip planes with 1 mm pitch placed close to the shower maximum at 5, 7 and 9 X_0; the second plane is used for the y coordinate measurement and the other two planes for the x coordinate measurement. More details are given in references [1], [2], [3] and [4].

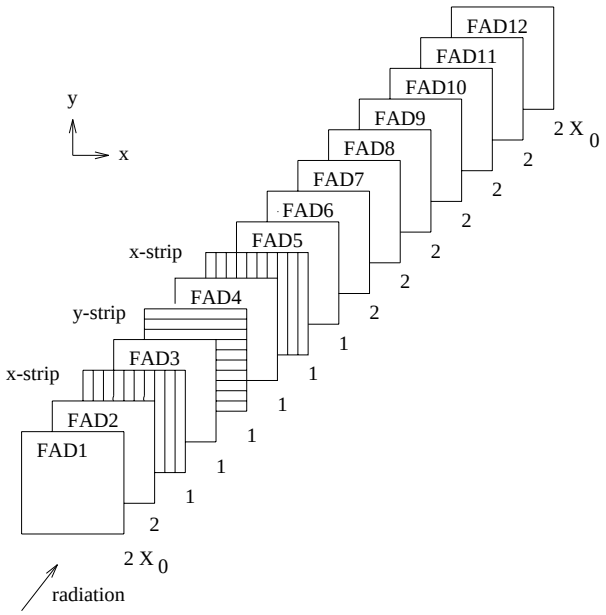

Figure 2: *Layout of the VSAT modules.*

Due to the very small emission angle of the Bhabha events accepted in the VSAT, in spite of the restricted angular acceptance of the detector (between 5 and 7 mrad in polar angle and about 50 degrees in azimuth), the accepted Bhabha cross section is very large (about 500 nb): this allows to monitor with high statistics, besides the luminosity, also the beam background and the variation of beam parameters.

The effect of the variation of beam parameters on the quantites measured by the VSAT will be discussed in section 2. In section 3, the procedure used to obtain the information on the beam parameters will be described and their variation during 1994 will be discussed.

2 Beam parameters monitoring with the VSAT

The beam parameters that are relevant for the following discussion are:

- the average values of the coordinates x_b, y_b and z_b of the interaction point;
- the corresponding beam widths σ_x, σ_y and σ_z;
- the average values of the incident positron and electron beam directions at the interaction point, in the (x, z) and in the (y, z) planes (we will call them briefly *tilts*), respectively θ^x_+, θ^x_-, θ^y_+ and θ^y_-;

- the beam divergence in the two planes, that is the spread around the above average directions.

The quantities measured with the VSAT which are used to extract information on the beam parameters are the x and y coordinates of the impact points of the scattered leptons on the four modules, while their directions cannot be measured. In the following two sections, we will discuss the dependence on the beam parameters of such coordinates.

2.1 Beam parameters in the (x,z) plane

The transport of the positron and the electron from the interaction point to the VSAT module is given by the product of three matrices which describe the trajectory in the three relevant regions shown in fig. 1:

- region 1, of length l_1, from the interaction point to the superconducting quadrupole in the DELPHI solenoid;
- region 2, of length l_2, through the superconducting quadrupole;
- region 3, of length l_3, from the superconducting quadrupole to the VSAT module.

Since the effect of the DELPHI solenoid is completely negligible for the Bhabha electrons in the VSAT, trajectories in region 1, as well as 3, are straight lines and the resulting equations between initial and final coordinates and directions are linear. Explicitly, the x coordinates of the impact points on the four VSAT modules are:

$$\begin{aligned} x_{F1} &= f_x(x_b - z_b(\theta_1^x + \theta_-^x)) + l_x(\theta_1^x + \theta_-^x) \qquad & x_{B2} &= f_x(x_b - z_b(\theta_1^x + \theta_+^x)) - l_x(\theta_1^x + \theta_+^x) \\ x_{B1} &= f_x(x_b + z_b(\theta_2^x - \theta_+^x)) + l_x(\theta_2^x - \theta_+^x) \qquad & x_{F2} &= f_x(x_b + z_b(\theta_2^x - \theta_-^x)) - l_x(\theta_2^x - \theta_-^x) \end{aligned} \tag{1}$$

where x_b, z_b are the x and z coordinates of the interaction point, θ_1^x and θ_2^x are the production angles in diagonal 1 and 2, respectively (always assumed to be positive) and θ_+^x (θ_-^x) is the tilt angles in the (x,z) plane of the incident positron (electron). The coefficients f_x and l_x are functions of the lengths l_1, l_2 and l_3 of the three regions and of the "k-factor" of the superconducting quadrupoles. For the values of 1993 and 1994 periods, their values are:

$$f_x = 2.1 \pm 0.1 \qquad l_x = (12.60 \pm 0.02)m \tag{2}$$

essentially equal for the four modules. Eqs. (1) show that particle trajectories can be treated as straight lines by assuming the modules to be located at an effective distance, l_x, from the center of DELPHI (z_b=0). Fig. 3 illustrates different situations, corresponding to one or more of the four beam parameters (x_b, z_b, θ_+^x, θ_-^x) being different from zero.

From eqs. (1), we see that it is convenient to use the quantities:

$$\begin{aligned} \Delta x_1 &= x_{F1} + x_{B2} = 2 \cdot f_x(x_b - z_b(\theta_1^x + \theta_x)) + \epsilon_x l_x \\ \Delta x_2 &= x_{F2} + x_{B1} = 2 \cdot f_x(x_b + z_b(\theta_2^x - \theta_x)) + \epsilon_x l_x \end{aligned} \tag{3}$$

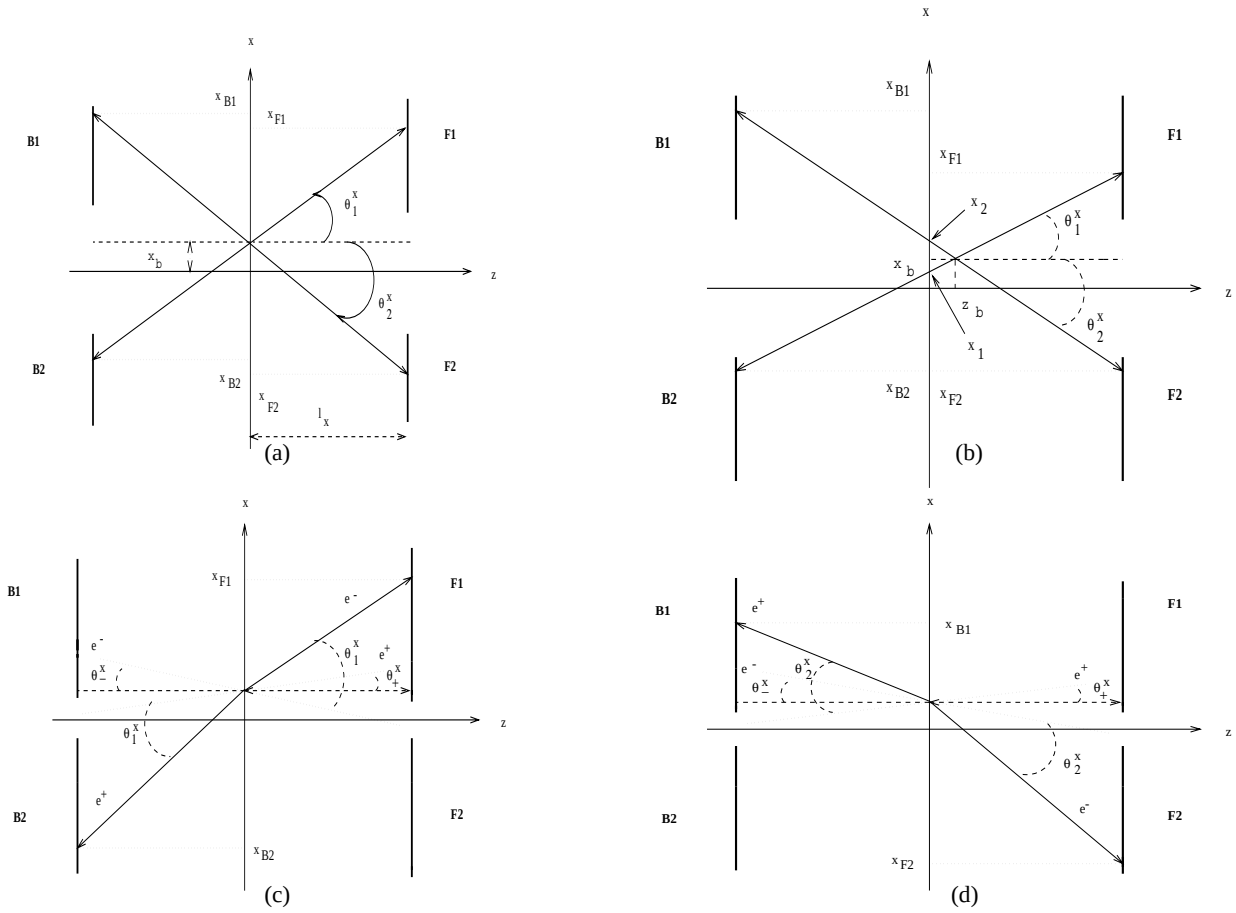

Figure 3: *(a) events with positive x displacement, zero z displacement and zero tilts; (b) events with the same values of x displacement and tilts but with a positive displacement in z; events for which only the z displacement is zero, in diagonal 1 (c) and in diagonal 2 (d).*

where we have defined the average tilt, θ_x, and the acollinearity, ϵ_x, as follows

$$\theta_x = \frac{\theta^x_+ + \theta^x_-}{2} \qquad \epsilon_x = \theta^x_- - \theta^x_+ \tag{4}$$

Eqs. (3) evidentiate the similarity of the x_b and ϵ_x effects on the impact points. This is more clearly depicted in fig. 4, where we have assumed for simplicity that only the electron beam has a nonzero tilt: the full lines correspond to outgoing particle tracks for $x_b = \theta^x_- = \theta^x_+ = 0$, whereas the dotted line shows the case of nonzero acollinearity and x_b=0 and the dashed line shows an event with zero acollinearity but nonzero x_b, which has the same impact points on the modules, showing that the ϵ_x and x_b effects are equivalent, and therefore these two parameters cannot be determined separately using the VSAT information alone.

To better separate the dependence on different beam parameters, we define the following quantities:

$$\Delta x = \frac{\Delta x_1 + \Delta x_2}{2} = 2 \cdot f_x x_b + \epsilon_x l_x + f_x z_b(\theta^x_2 - \theta^x_1 - 2\theta_x) \tag{5}$$

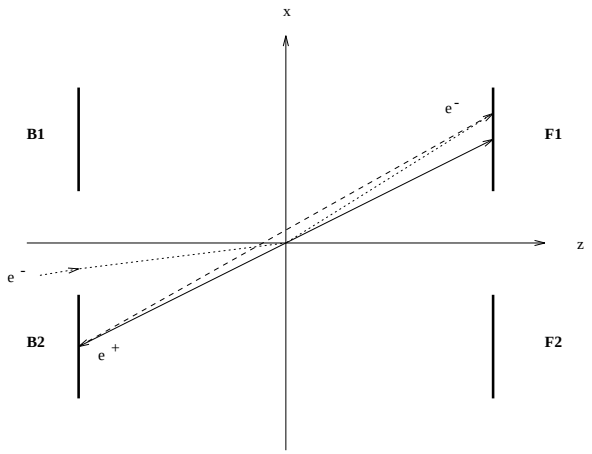

Figure 4: *Effects of the acollinearity and the x displacement on the impact points.*

$$\delta x = \Delta x_2 - \Delta x_1 = 2 \cdot f_x z_b (\theta_1^x + \theta_2^x) \tag{6}$$

By taking the average over a reasonably long period of time (we usually assume the time needed to write a cassette, which is about 20 minutes and corresponds to about 4 K events), we can substitute to θ_1^x and θ_2^x their average values, $\overline{\theta_i^x}$, which are both very close to 5.5 mrad. The equations show that the average value of the δx distribution essentially depends only on the value of z_b. On the contrary, the average value of the Δx distribution essentially measures the combined effect of the beam x displacement and beam acollinearity in the (x,z) plane, since the third term in eq. (5) is completely negligible.

From eq. (5) it also follows that the dispersion $\sigma_{\Delta x}$ of the Δx distribution is related to the dispersion of the distribution of x_b and ϵ_x, i.e. to the beam parameters σ_x and σ_{θ_x}:

$$\sigma_{\Delta x} = 2\ f_x\ \sigma_x + l_x\ \sigma_{\theta_x} + \sigma_m \tag{7}$$

where σ_m is the measurement error on Δx. The first and the third term are small compared to the middle one and are also rather well known, thus $\sigma_{\Delta x}$ can be used to measure the beam divergence, σ_{θ_x}.

However, due to the limited VSAT acceptance, the averaging procedure introduces second order dependences on the beam parameters, which can only be evaluated by an appropriate Monte Carlo simulation. We used to this aim the extensive simulations of different beam conditions which were done with the fast simulation program FASTSIM to determine the VSAT acceptance of Bhabha events for the measure of the luminosity (details of the program are found in [2]). Two major dependences are found: on σ_x and σ_{θ_x}, i.e. on the widths of the x_b and ϵ_x distributions and on the y tilt. Fortunately, both such dependences can be parametrized in terms of quantities directly measured by the VSAT, the former by $\sigma_{\Delta x}$ and the latter by the quantity Δy, which will be introduced below. The resulting corrections to Δx and δx are small and linear. Also, all the effective parameters of eq. (5) and (6), such as f_x and l_x, have been calculated with FASTSIM.

There are two other useful measures that can be done with the VSAT and which are related to the beam tilts. With a view to this, it is helpful to consider events with equal

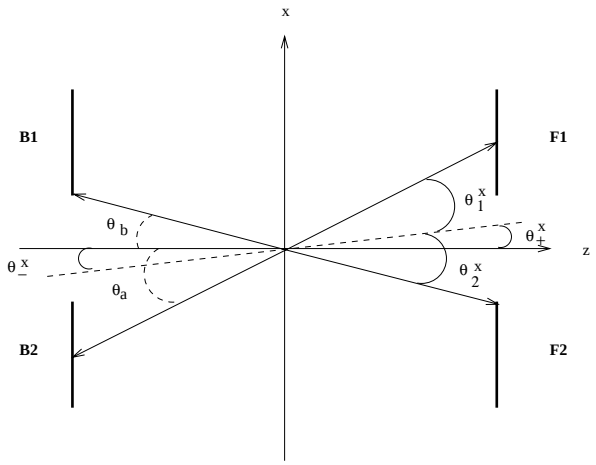

Figure 5: *Effect of the beam tilts on the production angles on the two diagonals.*

(positive) beam tilt angles, θ^x_+ and θ^x_-, as in fig. 5. The figure shows clearly that for the same values of the impact points the production angle on diagonal 1, θ^x_1, is smaller than in the case of zero tilts, where it would be equal to θ_a, while the opposite holds for the production angle on diagonal 2 (θ^x_2 is larger than θ_b). Due to the rapid decrease of the Bhabha cross section with the angle, this induces an opposite variation of the number of accepted Bhabha events on the two diagonals: the number of events on diagonal 1, N_1, will increase, whereas the number of events on diagonal 2, N_2, will decrease. Therefore, we expect to observe a variation of the variable:

$$A_D = \frac{N_1 - N_2}{N_1 + N_2} \tag{8}$$

called *diagonal asymmetry*. It must be noted, however, that the diagonal asymmetry is only affected by the average tilt angle, θ_x, and not by the separate values of θ^x_- and θ^x_+. By consequence, it cannot be used to extract information on the acollinearity, ϵ_x. The relationship between A_D and θ_x has been evaluated by FASTSIM.

2.2 Beam parameters in the (y,z) plane

The transport equations in the (y,z) plane are very similar to those of the (x,z) plane:

$$\begin{aligned} y_{F1} &= f_y(y_b - z_b(\theta^y_1 + \theta^y_-)) + l_y(\theta^y_1 + \theta^y_-) \qquad & y_{B2} &= f_y(y_b - z_b(\theta^y_1 + \theta^y_+)) - l_y(\theta^y_1 + \theta^y_+) \\ y_{B1} &= f_y(y_b + z_b(\theta^y_2 - \theta^y_+)) + l_y(\theta^y_2 - \theta^y_+) \qquad & y_{F2} &= f_y(y_b + z_b(\theta^y_2 - \theta^y_-)) - l_y(\theta^y_2 - \theta^y_-) \end{aligned} \tag{9}$$

There are however two important differences with respect to the (x,z) plane. The first difference is due to the fact that in the y direction the superconducting quadrupoles have a convergent effect, opposed to the divergent effect in the other plane. This gives values for the f_y and l_y parameters which are much smaller than those of the corresponding parameters in the (x,z) plane:

$$f_y = 0.10 \pm 0.02 \qquad l_y = (3.50 \pm 0.02)m \tag{10}$$

In particular, because of the small value of f_y, VSAT measures in the (y,z) plane are practically insensitive to the values of y_b and z_b. The second difference is the small angle of the production angles θ_1^y and θ_2^y, which average to zero.

We define

$$\Delta y_1 = y_{F1} + y_{B2} \qquad \Delta y_2 = y_{F2} + y_{B1} \tag{11}$$

and

$$\Delta y = \frac{\Delta y_1 + \Delta y_2}{2} \tag{12}$$

Taking the average value over one cassette, we obtain

$$\Delta y = 2 f_y y_b + l_y \epsilon_y \tag{13}$$

where we have defined the average acollinearity, ϵ_y, in a similar way as for the (x,z) plane.

Information on the average tilt

$$\theta_y = \frac{\theta_+^y + \theta_-^y}{2} \tag{14}$$

is provided by the difference

$$y_{F1} - y_{B2} \approx y_{F2} - y_{B1} \approx 2\, l_y\, \theta_y \tag{15}$$

We point out that a similar measure is in principle possible also in the (x,z) plane to obtain the value of θ_x, however, due to the narrow acceptance of the VSAT calorimeters, fluctuations in the average production angle completely mask possible effects of θ_x: for this reason in the (x,z) plane we use the diagonal asymmetry, A_D, which provides a much better measure of θ_x.

Finally, the width, $\sigma_{\Delta y}$, of the Δy distribution can be used to obtain the y divergence, σ_{θ_y}, of the beams.

3 Variation of the beam parameters

From VSAT data alone we can estimate the z coordinate of the interaction point using eq. (6), but this is not possible neither for the x nor for the y coordinate. This is due to the fact that, as shown in eq. (5) and (13), the detector variables depend both on the beam displacement and on the acollinearity in those directions. However, we can use eqs. (5) and (13) together with the beamspot values for x and y as they are determined by VD and TPC to obtain information on the variations of acollinearity.

3.1 Estimation of z beamspot

From eq. (6), we have

$$z_b = \frac{\delta x}{2 f_x (\theta_1^x + \theta_2^x)} \tag{16}$$

where δx has been corrected for second order dependence on beam parameters as explained in section 2. The sum of the production angles can be derived from the expressions of the impact points, eq. (1), as follows:

$$\theta_1^x + \theta_2^x = \frac{x_{F1} - x_{B2} - x_{F2} + x_{B1}}{2 \cdot l_x} \tag{17}$$

The distribution of z_b during 1994 is given in fig. 6. We observe an increase by 3 mm during period 1, a decrease of 1 mm during period 3 and small variations in period 2.

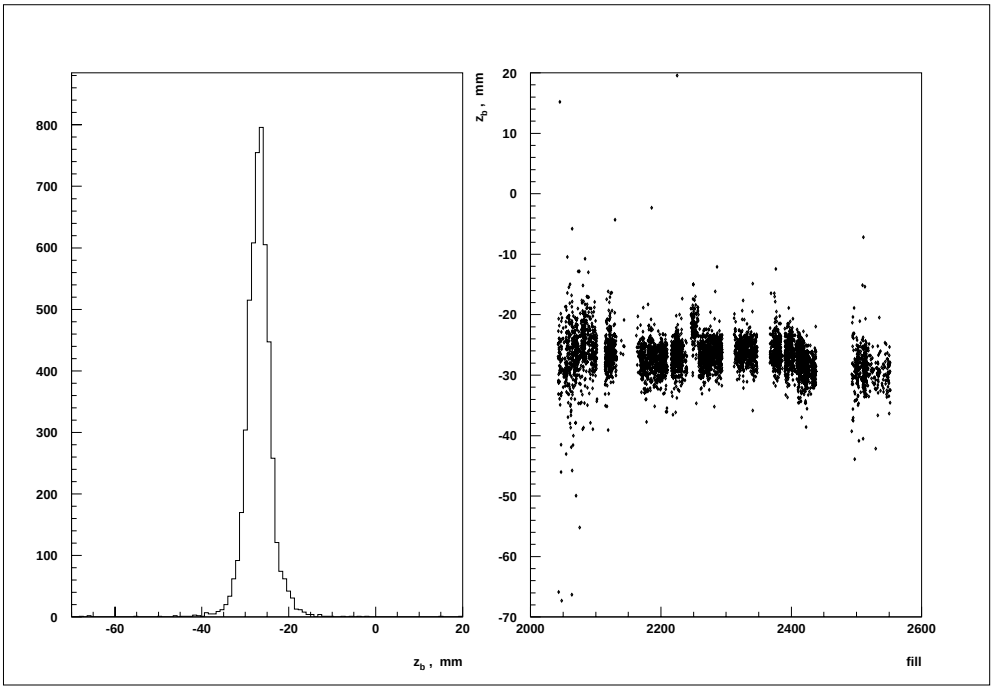

Figure 6: *z beamspot from* Δx_1 *and* Δx_2.

In fig. 7, we have plotted the VSAT versus the TPC measurement for the z beamspot.

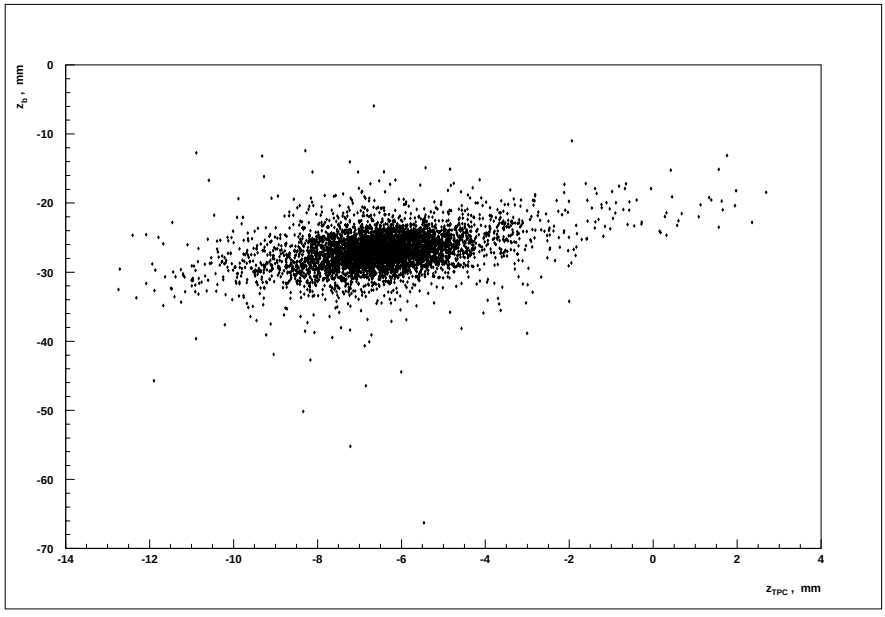

Figure 7: z_b *from VSAT versus* z_{TPC}.

In spite of the much larger error in the VSAT determination, We discern a linear relation, which is seen more clearly in the profile plot of fig. 8. The offset between the two measurements is of the order of 20 mm.

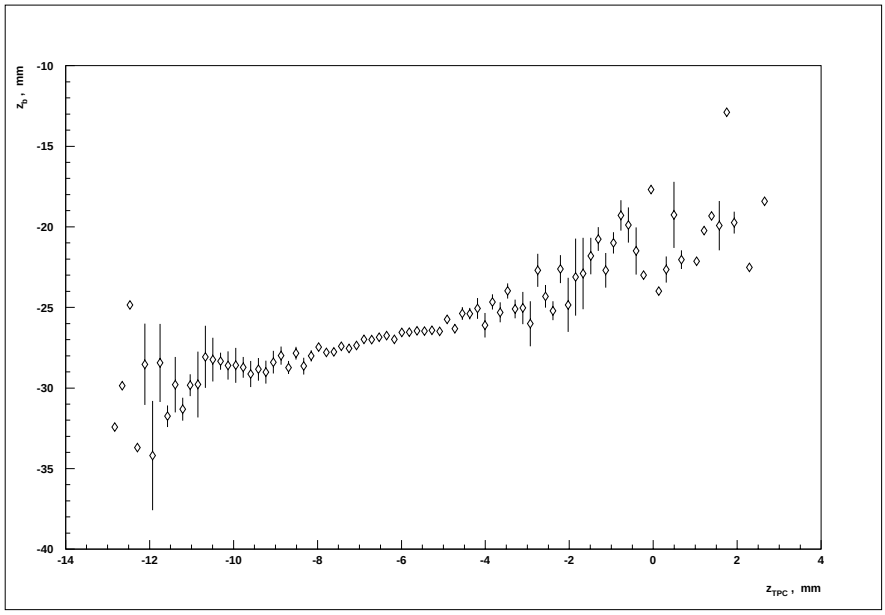

Figure 8: *Correlation between z_b and z_{TPC}, 1994 data.*

The distributions of the pulls of the VSAT and TPC determinations for all 1994 data and for the three periods are given in fig. 9 and 10, respectively and show that our

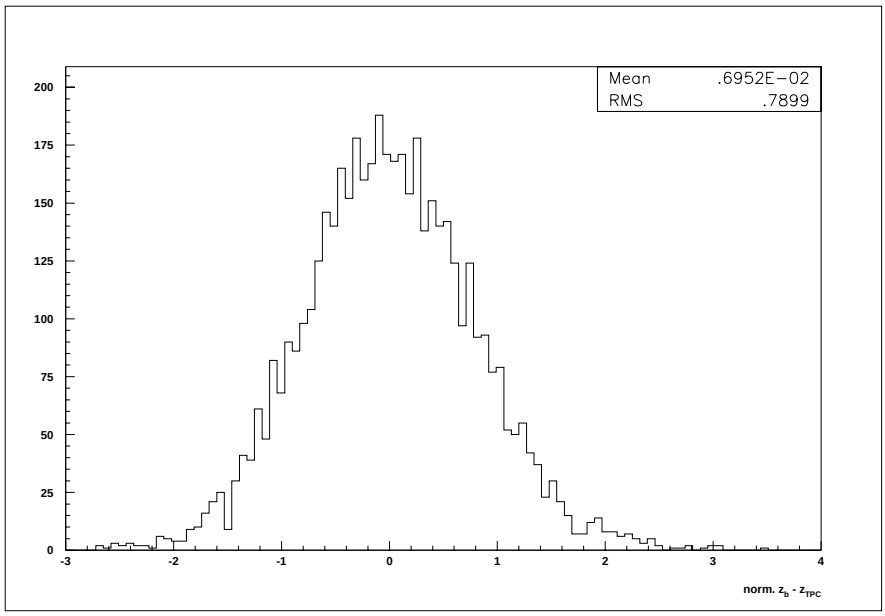

Figure 9: *Normalized difference between z_b and z_{TPC} for all 1994 data.*

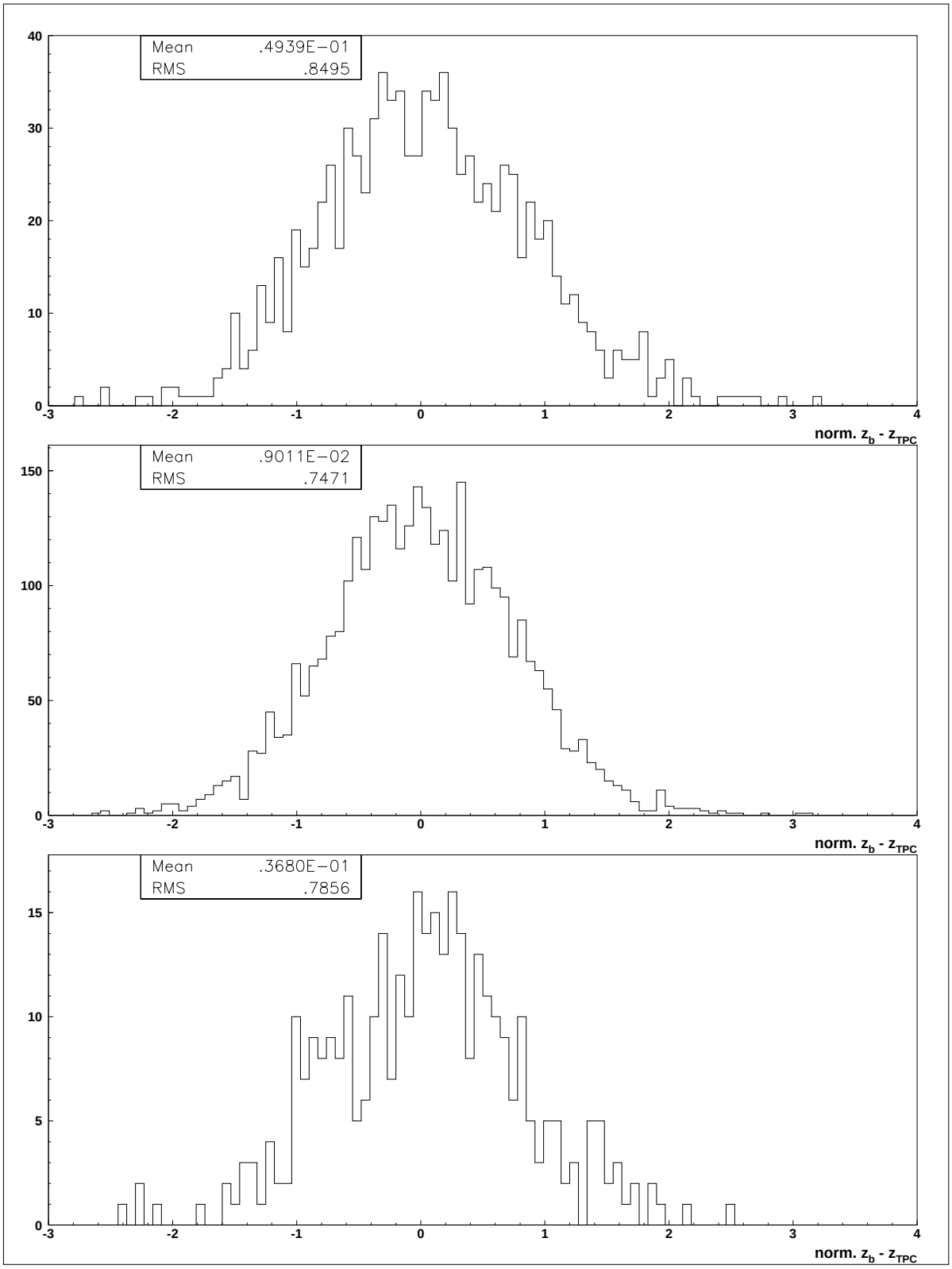

Figure 10: *Normalized difference between z_b and z_{TPC}, 1994 data, periods 1, 2 and 3.*

determination of z_b is compatible within errors with the TPC measure. The distributions of z_b for 1993 data and the corresponding difference from TPC are shown in figs. 11 and 12.

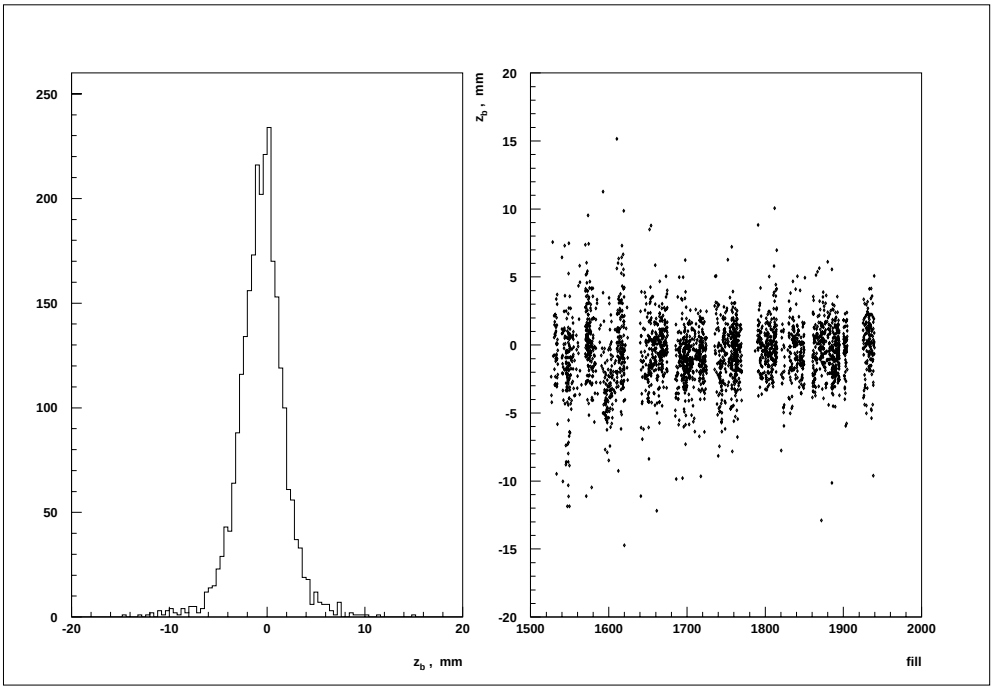

Figure 11: *z_b from 1993 data.*

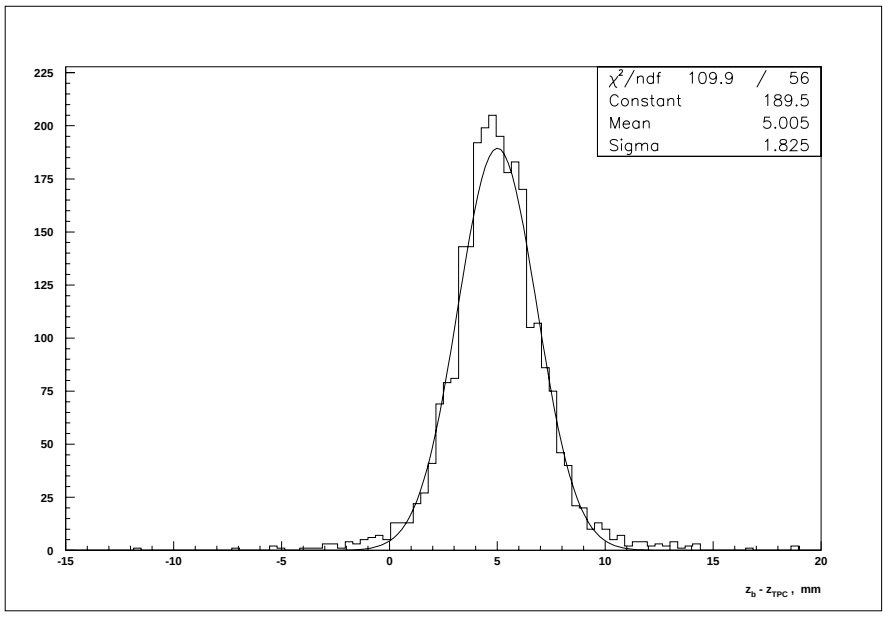

Figure 12: *Difference between z_b and z_{TPC}, 1993 data.*

3.2 Beam divergence, asymmetry and tilt

The variations of the beam width and divergence values are detected in terms of variations of $\sigma_{\Delta x}$. We show the variations of this parameter for 1994 in fig. 13.

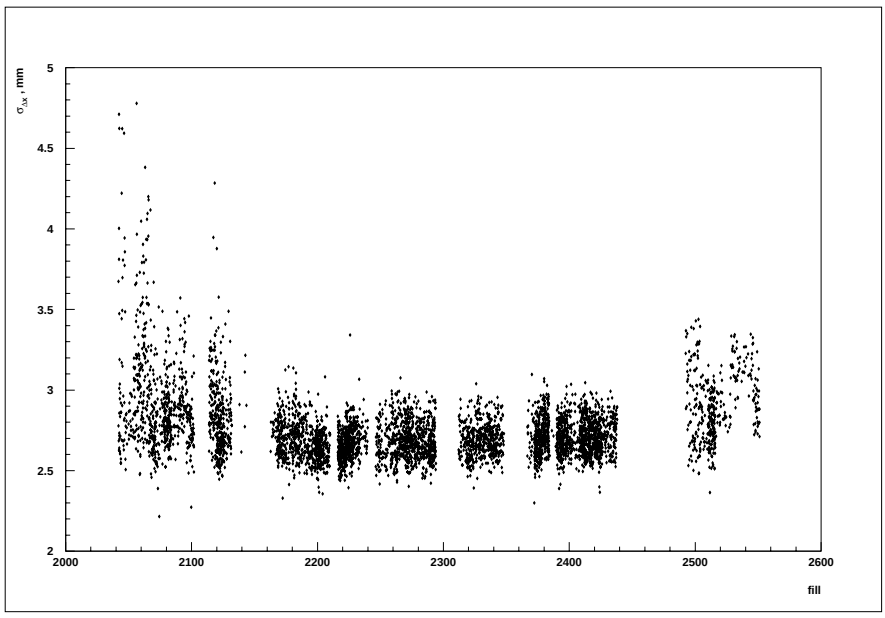

Figure 13: *Variation of $\sigma_{\Delta x}$ during 1994.*

We see that $\sigma_{\Delta x}$ varied from 2.2 mm to 4.8 mm in period 1, 3.4 mm in period 2 and 3.5 mm in period 3. There is an increase of the order of 50 μm during period 2. This variable covered a smaller interval in 1993 than in 1994, i.e. from 2.4 mm to 3.4 mm, within which it manifested more moderate fluctuation than in the following year.

The variations of the tilt angle in the (x,z) plane are monitored by the diagonal asymmetry defined in eq. (8). They are shown in fig. 14 for 1994 data and in fig. 15 for 1993 data.

The mean tilt, θ_y, in the (y,z) plane is monitored by the average y values of the impact points (see eq. 15). The variation of the mean tilt in the (y,z) plane during 1994 is given in fig. 16 and in fig. 17 for 1993 data.

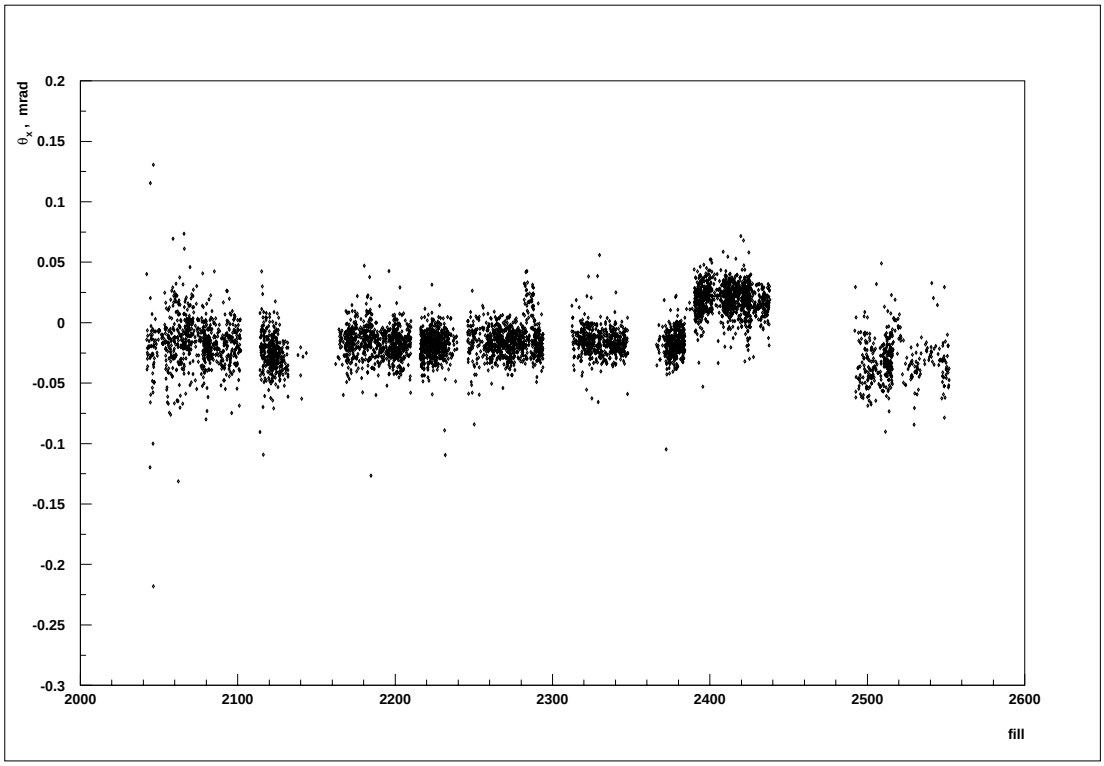

Figure 14: *Variation of θ_x during 1994.*

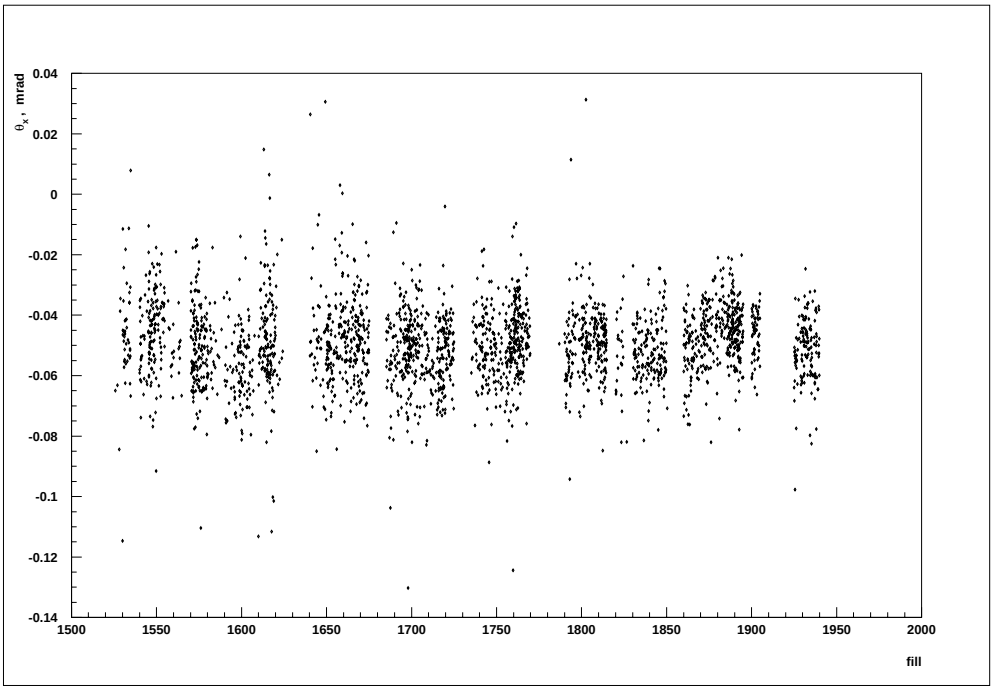

Figure 15: *Variation of θ_x during 1993.*

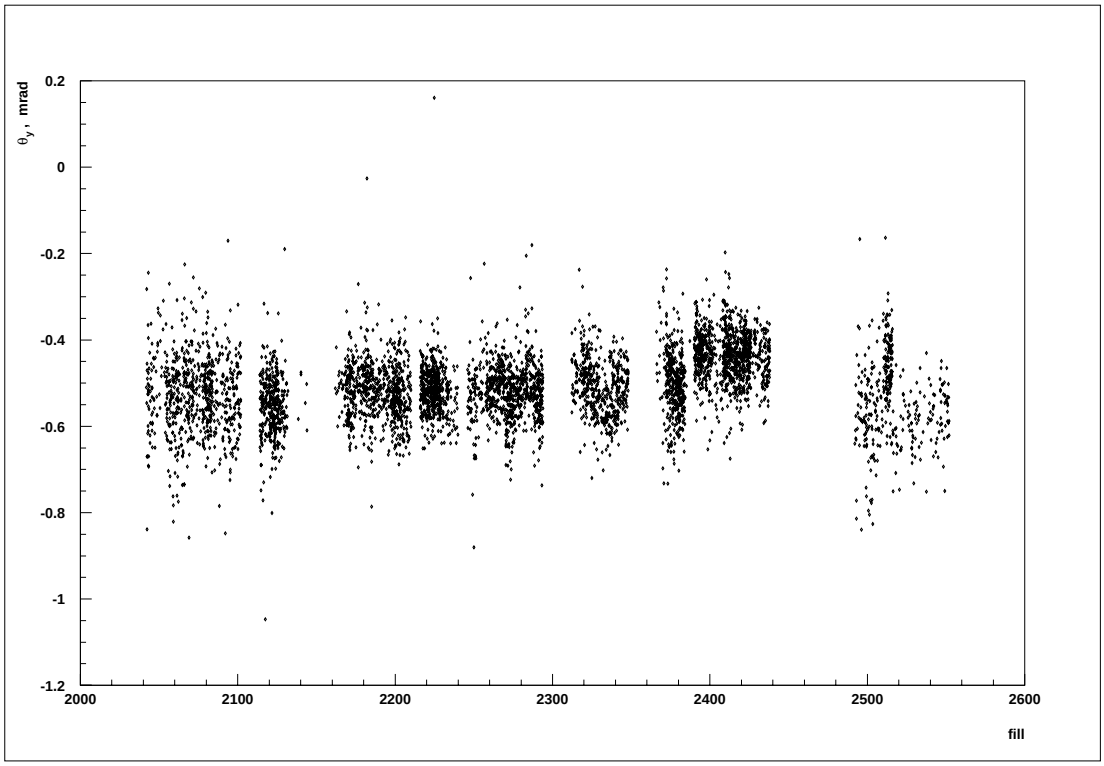

Figure 16: *Variation of θy during 1994.*

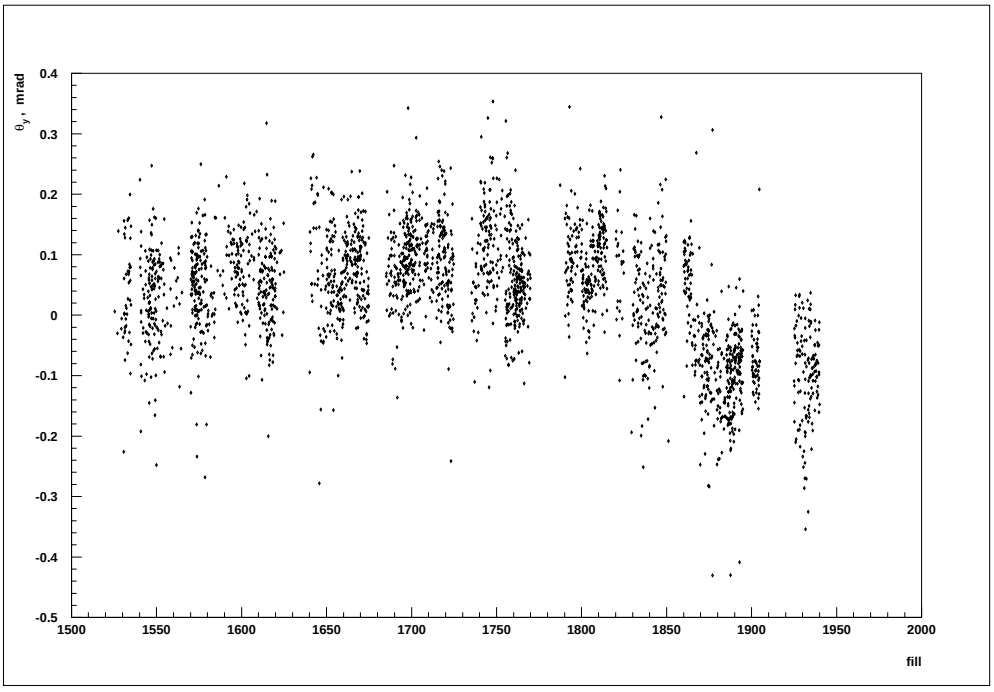

Figure 17: *Variation of θy during 1993.*

3.3 Acollinearity

In order to obtain acollinearity estimations in the (x,z) and (y,z) planes, we introduce the VD values for x beamspot and y beamspot in eqs. (5) and (13), from which we obtain the following expressions:

$$\epsilon_x \approx \frac{\Delta x - 2f_x \cdot x_{VD}}{l_x} \tag{18}$$

and

$$\epsilon_y \approx \frac{\Delta y - 2f_y \cdot y_{VD}}{l_y} \tag{19}$$

Fig. 18 shows ϵ_x for 1994 data. The most significant features are the increase of ϵ_x of the order of 50 μrad in period 1 and the rather large fluctuations in period 3. In fig. 19, the ϵ_x data for 1993 are shown: the range of ϵ_x fluctuations in 1993 was clearly smaller than in 1994.

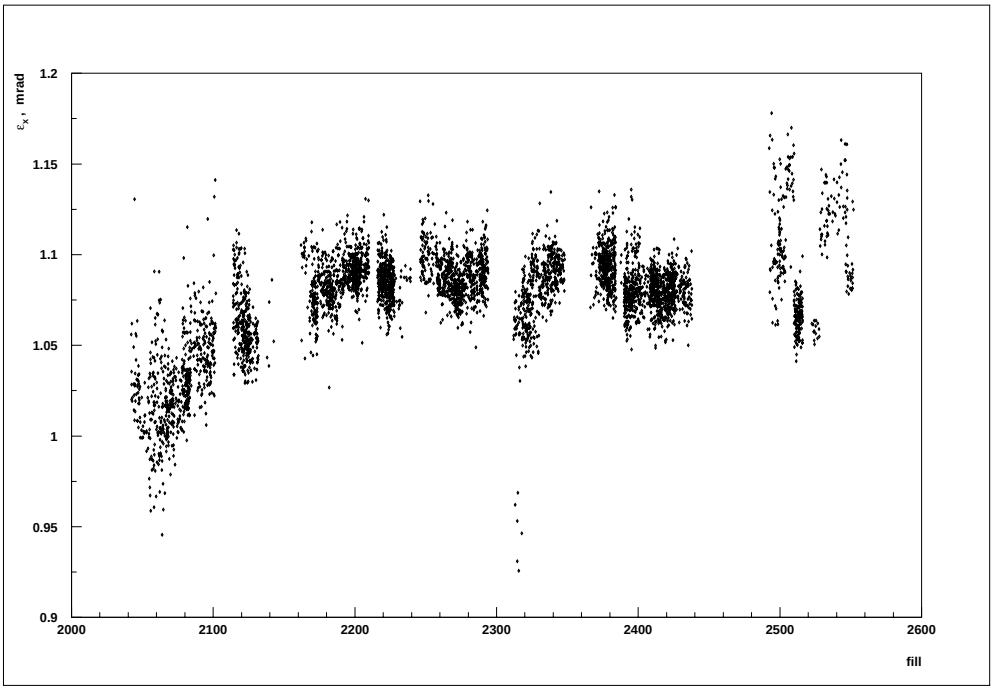

Figure 18: *Variation of ϵ_x during 1994.*

The 1994 variations of the acollinearity in the (y,z) plane are shown in fig. 20. The variations are much larger than those of ϵ_x with a large step of about 0.4 mrad between period 2 and periods 1 and 3. The ϵ_y variations in 1993 data are shown in fig. 21, where no sharp variation is observed.

In figs. 22-25, we give the corresponding distributions of figs. 18-21 for the results presented by LEP. Apart from an overall shift of the mean values, the agreement between the VSAT and LEP determination of the acollinearity in both planes and during both years is very good.

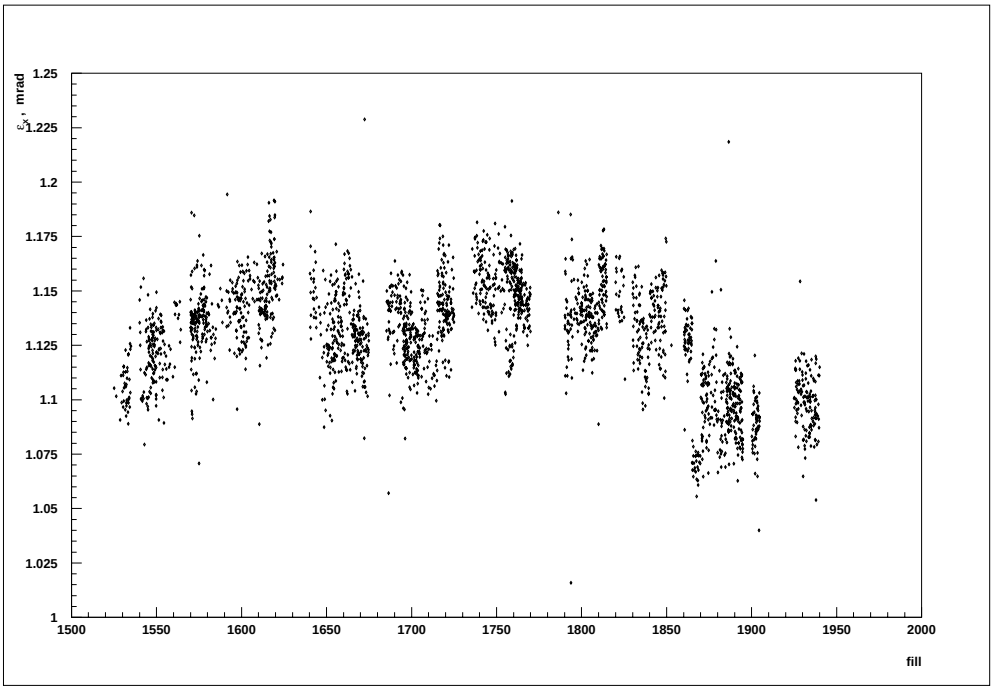

Figure 19: *Variation of ϵ_x during 1993.*

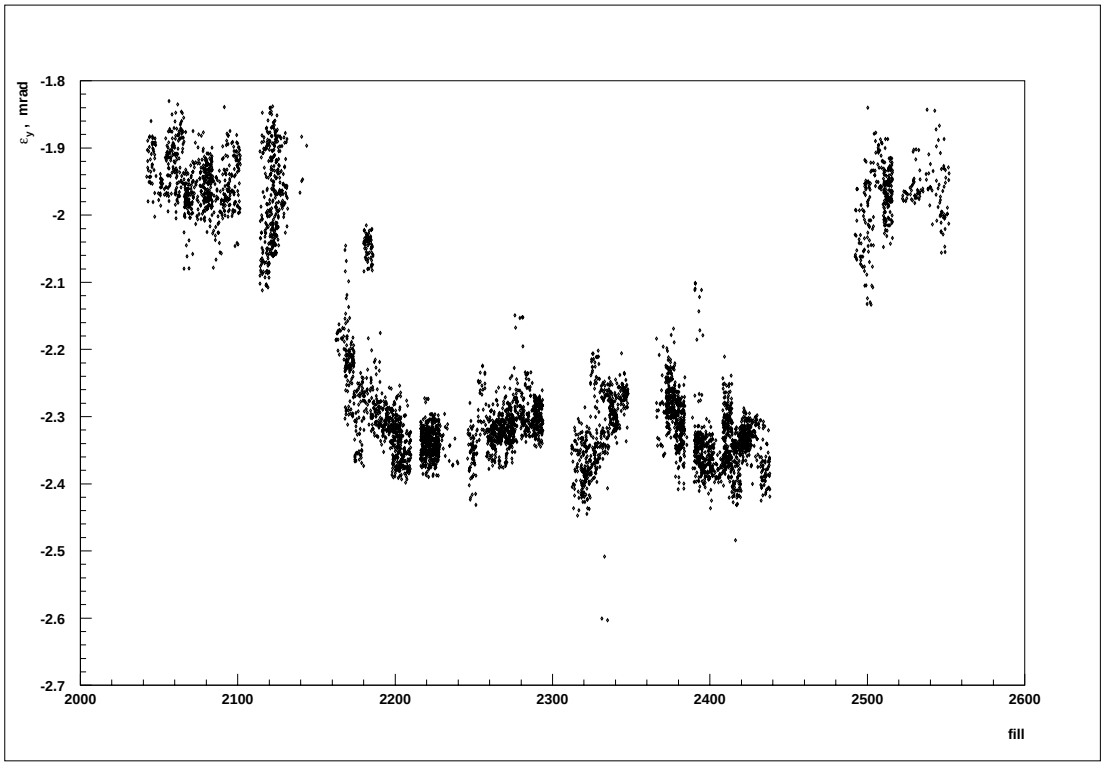

Figure 20: *Variation of ϵ_y during 1994.*

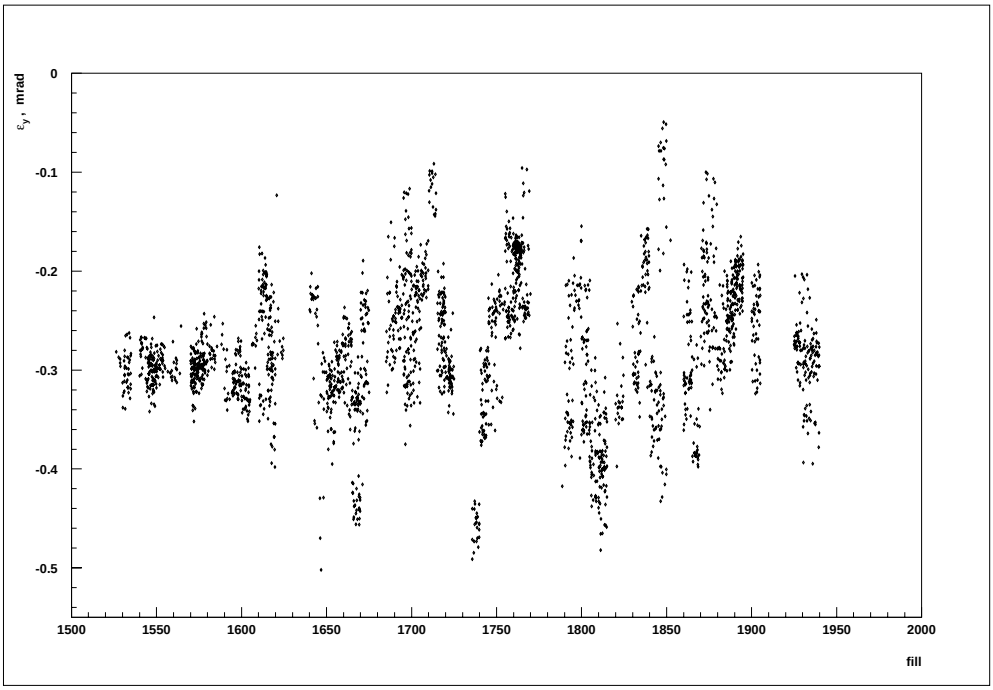

Figure 21: *Variation of ϵ_y during 1993.*

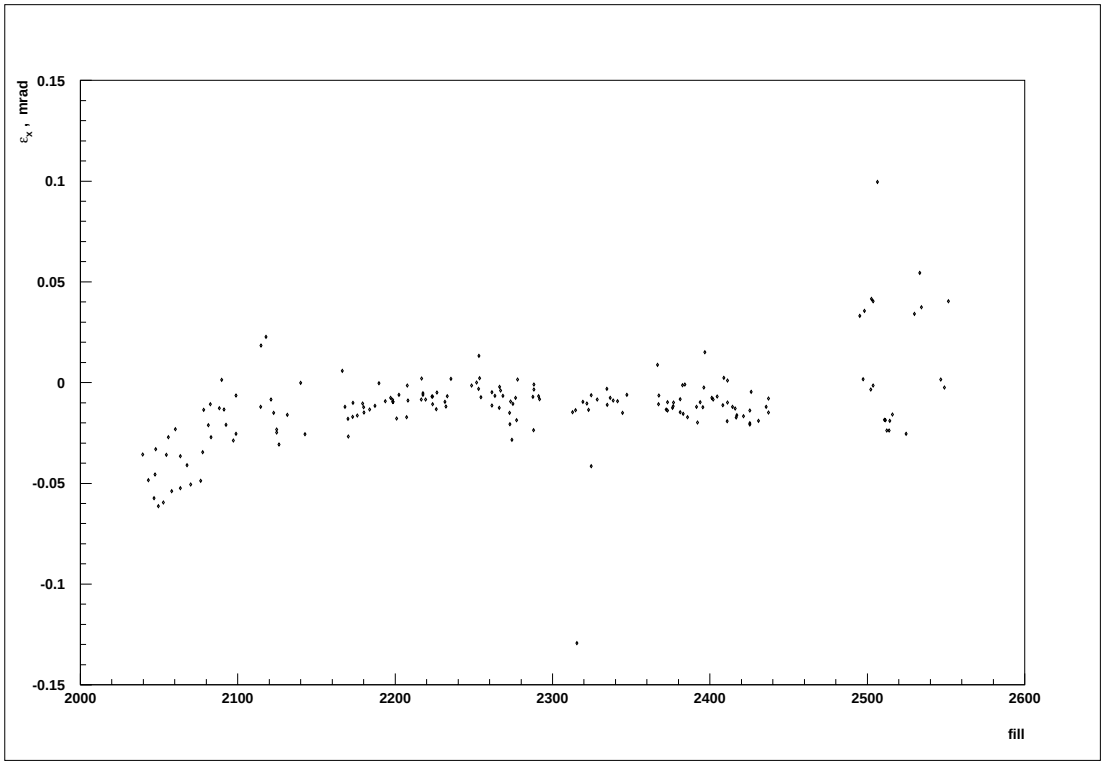

Figure 22: *ϵ_x from LEP during 1994.*

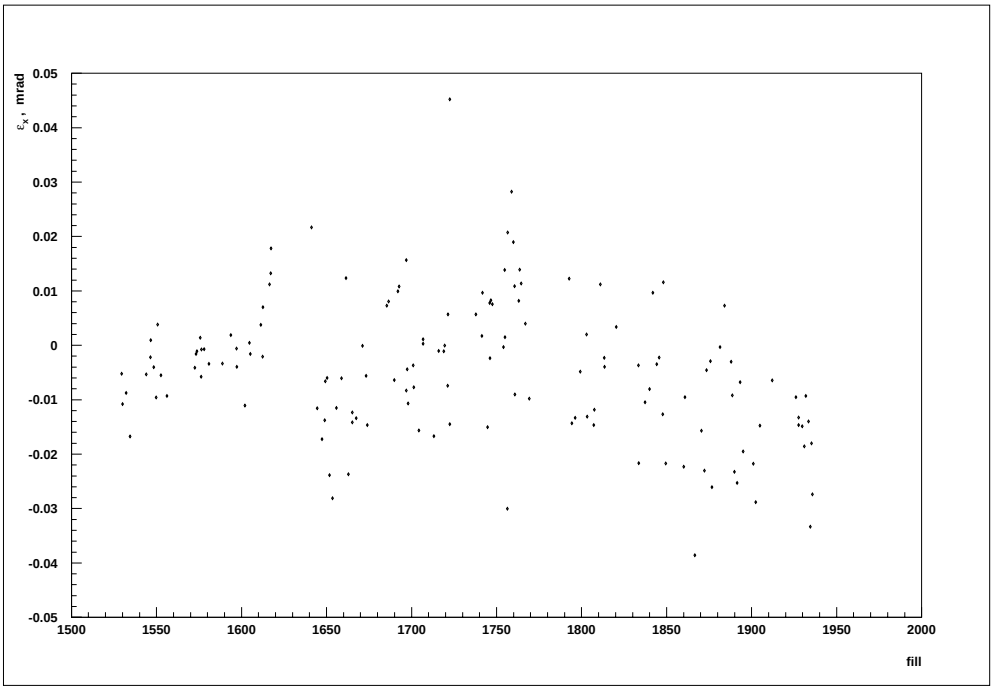

Figure 23: ϵ_x *from LEP during 1993.*

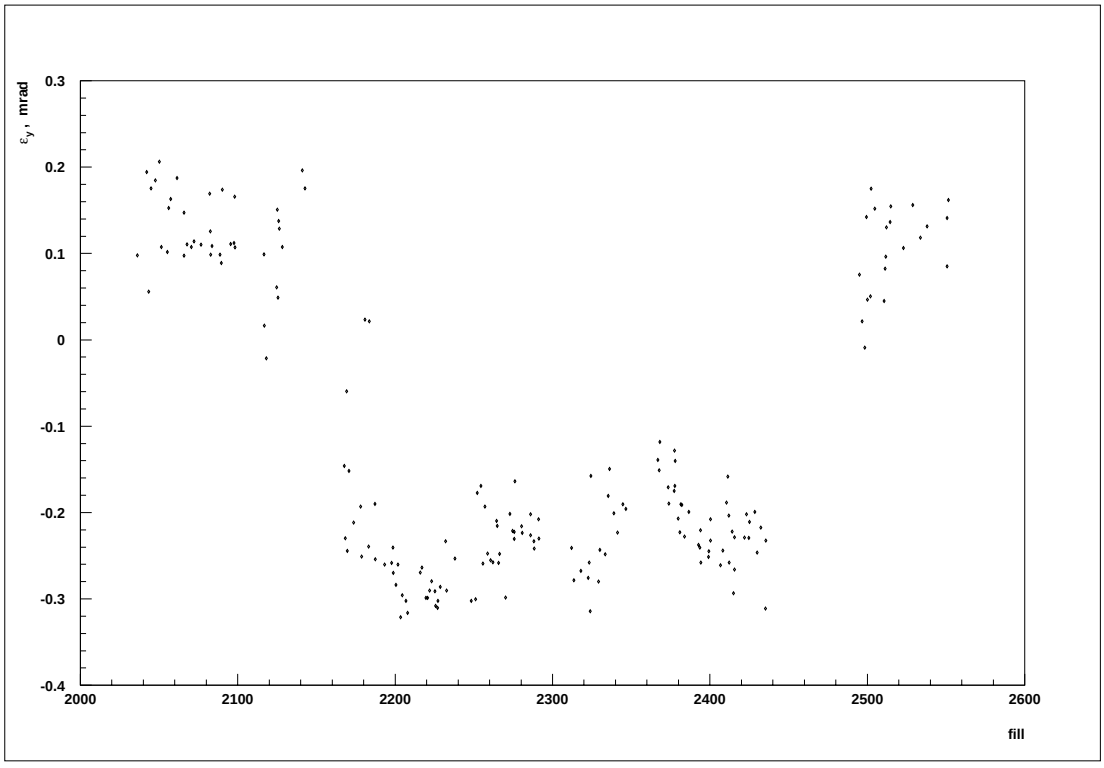

Figure 24: ϵ_y *from LEP during 1994.*

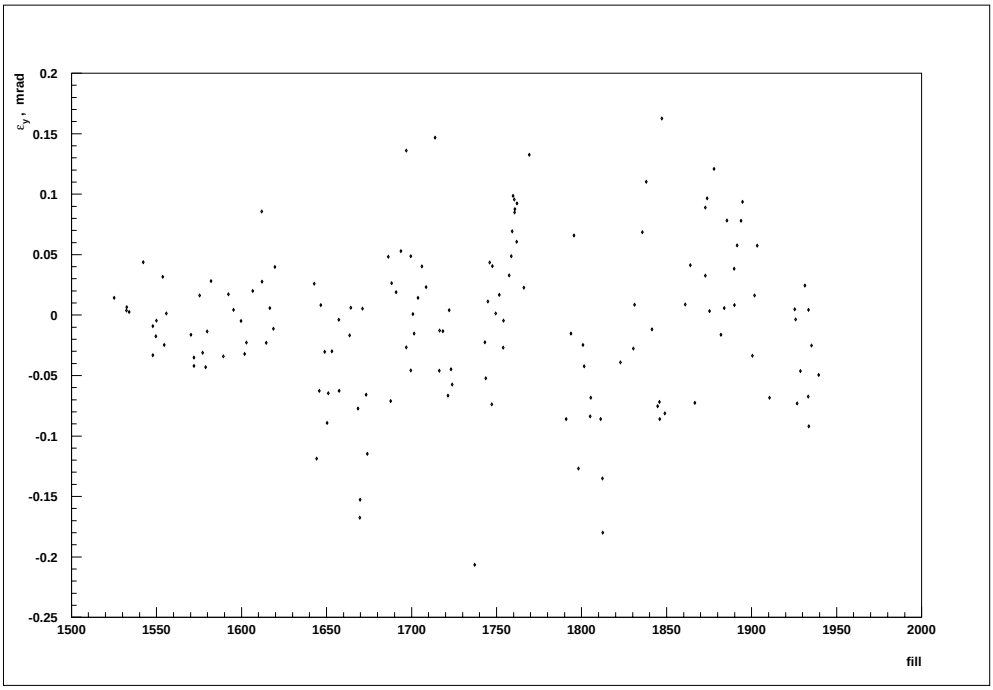

Figure 25: ϵ_y *from LEP during 1993.*

4 Conclusions

The position of the VSAT allows for high accuracy measurements of variation in time of LEP beam parameters. In particular, we have shown that the VSAT measurements, combined with the measurements of the beam spot done by TPC and VD, give useful information on tilt and acollinearity of beams. This information cannot be obtained easily from other detectors in DELPHI and it is very useful for a better understanding of the beam conditions at the DELPHI interaction point, which are relevant for many physics analyses.

References

[1] Almehed et al., *A silicon tungsten electromagnetic calorimeter for LEP.*

[2] Almehed et al., *High precision relative luminosity measurement with a Very Small Angle Tagger (VSAT) in DELPHI*, DELPHI 92-77 PHYS 188

[3] Almehed et al., *Beam parameter monitoring and interaction point measurement in DELPHI with the VSAT* DELPHI 94-144 PHYS 453

[4] Ch. Jarlskog, *Interaction point estimation and beam parameter variations in DELPHI with the VSAT*, LUNF D6/(NFFL-7110)/1995

Appendix B

DELPHI Collaboration

DELPHI 2000-005 PHYS 848
08 FEBRUARY 2000

VSAT Luminosity for the 1995 Scan

Ch. Zacharatou Jarlskog
Lund University

Abstract

The relative luminosity measurement performed by the Very Small Angle Tagger during the 1995 Z^0 scan is reported. The detector simulation, the systematic uncertainty and the comparison with the STIC luminosity are discussed.

1 Introduction

The luminosity monitors of e^+e^- storage rings benefit from the presence of Bhabha scattering, i.e. of the process[1] $e^+e^- \to e^+e^-$. At polar angles between 5 and 50 $mrad$, the scattering is in practice entirely described by a photon exchange in the t-channel. This ensures a low theoretical error on the calculation of the cross section. The lowest-order differential cross section can be approximated by the expression

$$\frac{d\sigma_0^{QED}}{dp_T} = \frac{2\pi\alpha^2}{p_T^3} \tag{1}$$

where p_T is the transverse momentum of the scattered particles. Eq. 1 implies a large forward peak, which gives to the process the additional advantage of high statistics.

The luminosity measurement in DELPHI is performed by two luminometers: the STIC detector, which calculates the absolute luminosity and the VSAT detector, whose task is to obtain a relative measurement with lower statistical error. This report presents the VSAT analysis with emphasis on the event selection and the dependence of the accepted cross section on variations of beam parameters.

2 Event selection and performance

The VSAT consists of four modules placed symmetrically to the DELPHI origin [1]. The modules in the forward region (C side) are called F1 and F2. The modules in the backward region are called B1 and B2. The modules F1 and B1 are located on the side of the beam pipe that is closest to the LEP center and are therefore labelled as inner modules in contrast with the modules F2 and B2, which are the so-called outer modules. One outer module together with the opposite inner module define one diagonal (arm) of the detector. We thus have two diagonals, named after the number of the forward module, i.e. diagonal one means F1-B2 and diagonal two means F2-B1. In either diagonal, the detector is triggered by coincidences with an energy deposit in each module greater than 20 GeV. These events are labelled as 'Bhabha triggers' and they form our initial sample. In order to extract the Bhabha set on which the luminosity calculation is performed, we first apply a set of cuts on an event-by-event basis, as described in the following subsections.

2.1 The energy measurement

We will first address the performance of the detector as far as the energy measurement is concerned, as this is of paramount importance for the event selection.

During the 1995 scan, the energy calibration was a complicated task because of the high contamination of our sample by events with wrongly assigned minibunch number[2]. Their majority consisted of high energy minibunch three data, representing approximately 10% of the total number of events. Their calibration is described in [2]. The rest of the

[1] The initial and final state radiation can be neglected for the purposes of this report.

[2] For the 1995 scan, LEP had modified its previous mode of single bunch operation to a scheme of tightly spaced minibunch-trains, i.e. instead of having only one bunch crossing every 25 μs there were 2 to 4 minibunches within each bunch. The time separation between minibunches was a fraction of a μs. Most of the scan data taking was done with 3 minibunches separated by about 250 ns.

mismatched events was a mixture of seven different combinations of minibunch numbers. They accounted for about 1% of the data. Their recovery is described in [3]. Moreover, the radiation accident of September 15 [4], having damaged the backward modules, entailed a separate treatment of the sample for the two periods before and after the accident. In spite of these complications, the energy calibration confirmed the stability of the modules: in fig. 1, we give the calibration constants for the four modules and the three minibunches. They have been extracted from the clean sample, after the mismatched events have been subtracted. The effect of the radiation accident is evident in the steps seen in the calibration constants of modules B2 and B1. The response of the modules was otherwise stable. The linearity of the modules is also established by fig. 1 as different fills have different beam energies.

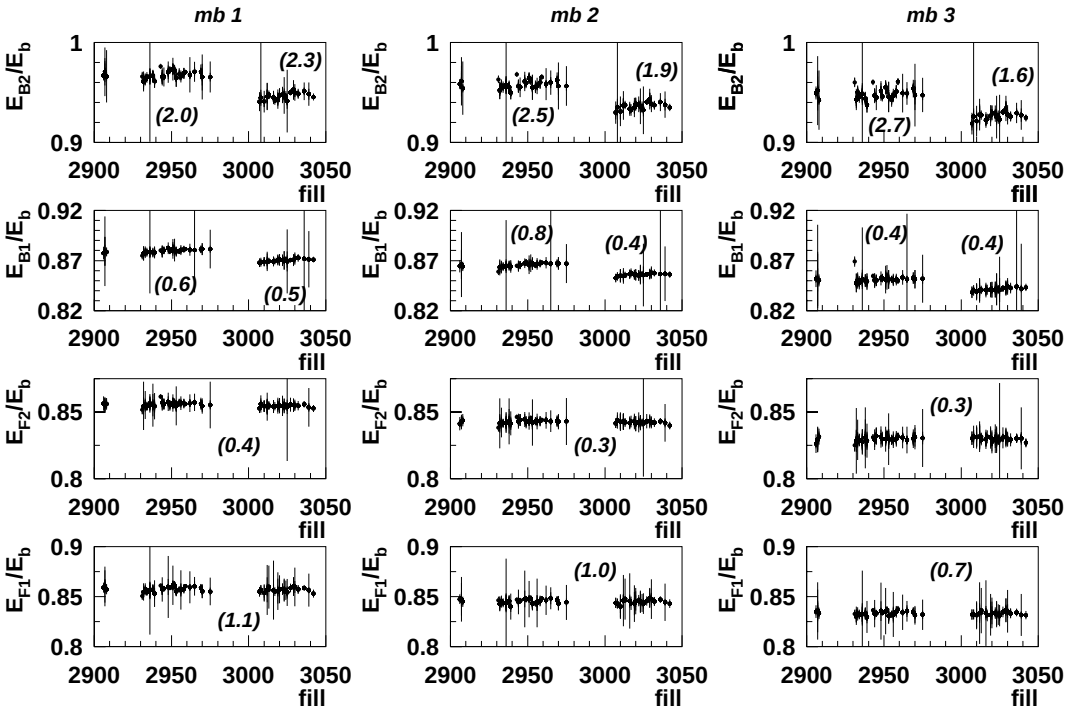

Figure 1: *Calibration constants for the four modules. The first, second and third column refer to events of minibunch one, two and three, respectively. The numbers in parentheses are the χ^2/dof for fits to constants. Two fits were done for each plot of modules B2 and B1 (corresponding to the periods before and after the radiation accident, i.e. before and after fill number 3000).*

2.2 Background subtraction

The background has two components: (a) accidental coincidences (also called false Bhabha events) and (b) coincidences between low energy depositions, mainly originating from off-momentum particles. The accidental coincidence rate is estimated by tagging one particle in one module and one particle in the diagonal module four beam crossings later. The low energy coincidences are removed from the data by applying a cut at 70% of the beam energy. However, there may be events where the particle's energy is above that cut but still lower than a full energy deposit. These refer to particles that have began to shower

outside the module. Such particles have their maximum energy deposit in the inner x-strip of the detector and we thus use this x-position cut in order to remove them. An example of the above mentioned distributions for module B1, fill 3029, is given in fig. 2. There were 51221 triggers registered (solid line), 3190 (6%) of which were removed by the 70% energy cut on B1 (depicted by the arrow in fig. 2(a)). The same cut on the diagonal module discarded 3290 B1 events (dashed line). The accidental coincidences (dotted line) represented only 0.08% of the triggers (42 events). Fig. 2(b) shows that the x-position cut removed 2753 events (5%) (dashed line) and 3560 events (dotted line) of B1, i.e. 7% of the triggers, when applied on F2. The remaining Bhabha distribution contained 44268 events, i.e. 86% of the initial sample.

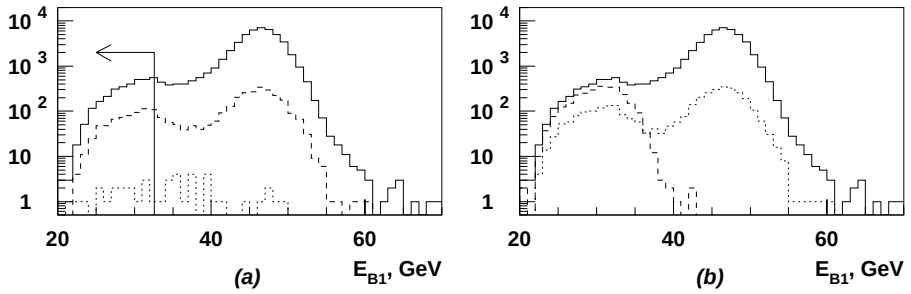

Figure 2: *The effect of background and position cuts on the Bhabha triggers of B1 (solid line): (a) energy cut on B1 (arrow) and on F2 (dashed line), accidental coincidences (dotted line), (b) x cut on B1 (dashed line) and on F2 (dotted line). (The vertical axes show numbers of events.)*

2.3 Acceptance cuts

The acceptance of the detector is restricted by the so-called radial cut. This cut defines a volume with outer edge corresponding to a maximum allowed radius of 7.7 *cm* (fig. 3(a)) and inner edge corresponding to a minimum allowed sum of the x positions ($sx = |x_{inner\ module}| + |x_{outer\ module}|$) equal to 13.2 *cm* (fig. 3(b)). The reason for the outer

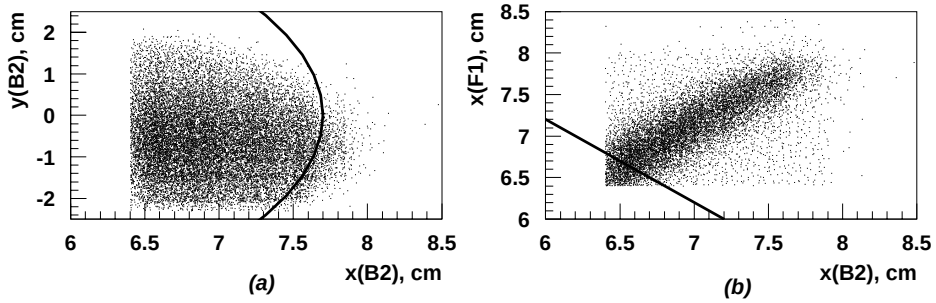

Figure 3: *The acceptance cuts; (a) the cut on the outer edge, (b) the cut on the inner edge of the detector.*

edge cut is the following. Upstream of the VSAT modules (at about 6.5 m from the interaction point), the x radius of the beam pipe is increased from 6 *cm* to 8 *cm*. In the connection region there is a thick flange which strongly absorbs the electrons with a large angle. From the (x, y) distribution of the impact points of the electrons in the VSAT we see that the absorption is not sharp and also that it is difficult to reproduce it faithfully with the simulation. For this reason, we set a cut at the value of the radius for which the (x, y) distributions of the data are compatible with the (x, y) distributions of the detector

simulation FASTSIM (described in the following section). A similar argument holds for the cut at the inner edge. Again, by comparing the sx distributions of simulation and data, we see that there are small differences (of the order of few permille) at small sx. The events with very small sx are those in which both the forward and the backward electron have a small angle and thus a small x, that is they are both close to the inner edge of the VSAT module. These events are difficult to simulate faithfully because they depend critically on many parameters (beam position, beam tilt, etc.) and thus we set an sx cut at the value for which the sx distributions of the simulation and of the data are compatible.

The mean value of Bhabha events for the total volume (i.e. before applying the radial cut) was 3136 events per cassette in diagonal one and 3445 events per cassette in diagonal two. These numbers were reduced by 22% and 28%, respectively, when the acceptance cut was applied.

2.4 Corrupted data

Due to imperfections in the electronics, especially in the beginning of the run of 1995, the read out was occassionally corrupted. In order to remove the cassettes with high contamination we set two limits: first, the number of corrupted Bhabha triggers must be less than 10% and second, the number of corrupted buffers must be less than 1 permille. The reason for applying this cut is that we correct for the corrupted events that we miss using the trigger information which is generally available even if the buffer is corrupted, but this is a correction which has a large uncertainty, so it is valid only if the fraction of corrupted data is small, otherwise it introduces an error larger than the gain in statistics we would have by including the corrupted cassettes.

Fig. 4 shows the distributions of these two variables and the positions of the cuts. In order to decide on the values of the cuts we tried different combinations and we kept the one that gave the largest number of cassettes possible without allowing the normalized differences between STIC and VSAT luminosities to become too large. In total, the two cuts rejected 31% of the initial number of cassettes (1200).

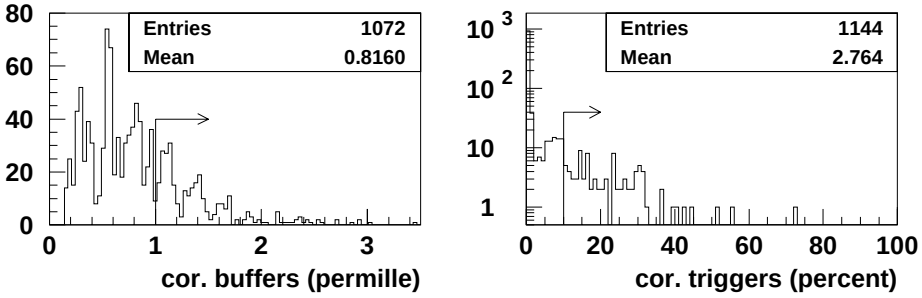

Figure 4: *Distributions of corrupted buffers and corrupted triggers. The arrows show the position of the cuts. The vertical axes show numbers of cassettes.*

3 The detector simulation

The visible Bhabha cross section can be evaluated by convoluting the theoretical cross section with the geometrical acceptance of the detector but as this task is very complicated

the detector simulation is used instead. First, it determines the accepted cross section and then it calculates its dependence on beam parameter variations [5].

3.1 Description of FASTSIM

The events are generated with BHLUMI 4.03, where the radiative corrections are calculated with the YFS exponentiation, giving a theoretical uncertainty of 1.1 permille. Then FASTSIM tracks the particles from the interaction point to the detector dividing the path of the scattered particle into three transport regions [6]:

- from the interaction point to 3.7 m along the z-direction, i.e. through the magnetic field of the DELPHI solenoid,
- through the field of the superconducting quadrupoles, which are located between 3.7 m and 5.7 m along the beam axis and
- in the field-free region between the quadrupoles and the modules.

The motion of the particle through each of the above mentioned regions is represented by a matrix describing the transformation of the phase space coordinates. In order to reduce the execution time, the simulation ressorts to a number of approximations. First, the particles that hit the flanges or the material in front of them are discarded. Second, the beam pipe has to be taken into account: behind the flanges it is made of 1.5 mm of iron, which corresponds to 0.085 r.l., so it is possible that the outgoing particle's shower starts when it hits the beam pipe. FASTSIM calculates the thickness of the traversed material and adds it on the front of the module. The difference from the data is then that the angle between the shower products at the module's front face is not taken into account but this has no significant effect on the analysis. Particle synchrotron radiation in the magnetic fields is also neglected. Lastly, the longitudinal and transverse shower profiles are parametrized as described in [7].

3.2 The accepted cross section

After FASTSIM has calculated the energy and position of the particles that hit the detector, the events are analyzed by the same program we analyze the data with. The accepted cross section is then calculated as follows [8]. BHLUMI generates events according to the Born cross section and then modifies it by adding the radiative corrections. If σ_g is the (differential) Born cross section for a particular event and σ_i is the same cross section with all corrections, a weight $w_i = \sigma_i/\sigma_g$ is assigned to the event. After the event has passed the detector simulation and the experimental cuts we can calculate the average weight for all the accepted events $\overline{w} = \sum_{acc} w_i/N_{generated}$, where $N_{generated}$ is the number of generated events. The accepted cross section is then given by the expression $\sigma_{acc} = \overline{w} \cdot \sigma_{approx}$, where σ_{approx} is the integrated Born cross section for the kinematical region which was used for the run of BHLUMI.

3.3 Correction of the cross section for beam parameter variations

In order to correct the accepted cross section for the variation of the beam parameters, 29 FASTSIM runs were done. In 21 runs the x beamspot and the electron and positron divergences in x were varied. In the remaining 8 runs the electron and positron tilts in y were varied [8]. All runs had 1.2 million generated events, except for 9 of the 21 first runs, which had 2 million generated events.

In the simulation, the values of the x beamspot and divergence and of the y tilt were chosen so that the impact points of the electrons and positrons on the modules would be close to those of the real data. This is necessary because the corrections to be applied to the cross section are valid only for small variations of the average positions of the impact points, which have thus to be similar between real and simulated data. The average x and y positions of the simulated data are shown in fig. 5 for the two diagonals, compared with those of the real data: as one can see, the simulation is reasonably close to the real data, the small differences being tolerable within the statistical uncertainties of the correction factors (Table 1).

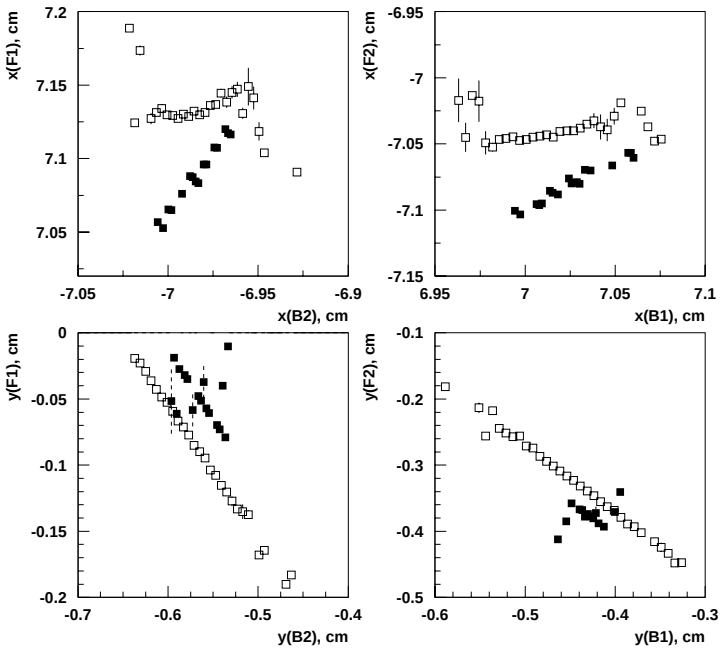

Figure 5: *Comparison between data (open squares) and FASTSIM (solid squares) for the coordinates of the impact points. (The positive tail values of the y(F1) distribution are not shown [7].)*

The correction of the cross section is subsequently done in terms of variables which are directly measured by the detector as follows [9]. For each FASTSIM run and for each diagonal i we calculate the accepted cross section σ_i and the variables $\Delta x_i, R\Delta x_i, \Delta y_i$ and A_D defined as

$$\Delta x_i = x_i^{forward} + x_i^{backward}, \qquad \Delta y_i = y_i^{forward} + y_i^{backward}, \qquad A_D = \frac{N_1 - N_2}{N_1 + N_2}$$

where $x_i^{forward}$ ($x_i^{backward}$) is the x coordinate (averaged over the run) of the impact point

of the particle on the forward (backward) module, $y_i^{forward}$ ($y_i^{backward}$) is the average y coordinate of the impact point of the particle on the forward (backward) module, N_1 (N_2) is the number of Bhabha events in diagonal one (two) and $R\Delta x_i$ is the dispersion of the Δx_i distribution. The corrected cross section of diagonal i is then

$$\sigma_i = \sigma_0[1-a_i(\Delta x_i-\overline{\Delta x_i})-b_i(\Delta x_i-\overline{\Delta x_i})^2-c_i(\Delta y_i-\overline{\Delta y_i})-d_i(R\Delta x_i-\overline{R\Delta x_i})-e_i(A_D-\overline{A_D})] \quad (2)$$

The mean values are those of the complete data sample. σ_0 is treated as an unknown constant. In order to calculate the coefficients (slopes) a_i, b_i, c_i, d_i, e_i we do fits to the corresponding distributions of σ_i, e.g. to calculate c_i we do a linear fit to the distribution of σ_i versus $\Delta y_i - \overline{\Delta y_i}$, etc. The results are given in Table 1. The small differences between diagonals one and two are due to small asymmetries in the setup.

	value for i=1	value for i=2
a_i (cm^{-1})	0.400 ± 0.030	-0.128 ± 0.020
b_i (cm^{-2})	1.800 ± 0.700	0.200 ± 0.500
c_i (cm^{-1})	-0.090 ± 0.030	-0.190 ± 0.030
d_i (cm^{-1})	0.300 ± 0.100	0.300 ± 0.100
e_i	0.001 ± 0.040	0.001 ± 0.040

Table 1: *Slopes for the 1995 scan.*

4 Results

4.1 Relative luminosity

According to eq. 2, the number of accepted Bhabha events in the data has to be corrected as follows

$$N^j = \frac{N_1^j}{1 - a_1(\Delta x_1^j - \overline{\Delta x_1^j}) + ...} + \frac{N_2^j}{1 - a_2(\Delta x_2^j - \overline{\Delta x_2^j}) + ...}$$

where N^j is the corrected number of events for the j-th cassette, N_i^j is the number of accepted Bhabha events in diagonal i and the denominators contain all the beam parameter corrections that we discussed in the previous section. We calculate the VSAT relative luminosity by adjusting the value of σ_0 so that the normalized differences with the STIC luminosity will be close to zero for the total data sample. The results are given in Table 2. The first four lines give the VSAT luminosity. Its values for all minibunch numbers, for minibunch one, two and three are given in lines one, two, three and four, respectively. The numbers referring to 'all' minibunches include also the Bhabha events that could not be associated with a specific minibunch number (unrecoverable mismatches), thus corresponding to the total Bhabha event sample. The next four lines give the corresponding values for STIC luminosity. Then the total numbers of VSAT and STIC Bhabha events are mentioned. In the next line of the table, we give the normalized differences (pulls) between VSAT and STIC luminosities for all minubunch numbers. We see that the pulls are acceptable. The errors for the VSAT luminosity follow, for all minibunches and for each minibunch separately. The total error is calculated by adding quadratically the statistical error and the systematic error. The systematic error stems mainly from the

cross section correction for the beam parameters. For example, the correction for $R\Delta x_1$ is $d_1(R\Delta x_1 - \overline{R\Delta x_1})$, where d_1 is the slope, i.e. the correction factor given by FASTSIM, $R\Delta x_1$ is the value of the cassette currently processed and $\overline{R\Delta x_1}$ is the average value of $R\Delta x_1$ over all scan data. As a consequence, there are two contributions to the error, one due to the error of the slope, which comes from FASTSIM and is called correlated systematic error and the other being the error of $R\Delta x_1$ (depending on the statistics of the cassette) included in the uncorrelated systematic error. The uncorrelated error also includes the contribution of the uncertainties due to the energy and inner edge cut. The former is about 0.1 permille: it is due to the uncertainty of the trigger efficiency at the energies corresponding to the cut. The latter is estimated to be about 0.25 permille and it is due to the statistical error on the effect of the low sx

	mb	peak	peak-2	peak+2	total
L^{int}_{VSAT}	all	1752.54	4619.77	5520.35	11892.64
(nb^{-1})	1	580.63	1628.97	1951.87	4161.47
	2	619.18	1549.52	1870.15	4038.85
	3	550.50	1434.84	1691.23	3676.57
L^{int}_{STIC}	all	1736.78	4640.97	5515.72	11893.46
(nb^{-1})	1	571.33	1628.97	1948.72	4149.02
	2	614.71	1565.19	1873.14	4053.04
	3	550.21	1445.61	1692.03	3687.85
VSAT Bhabha events	all	612277	1681154	1859281	4152713
STIC Bhabha events	all	95232	266399	290134	651765
Pull	all	2.59	-2.15	0.41	-0.05
VSAT stat. error	all	1.28	0.77	0.73	0.49
(permille)	1	2.22	1.30	1.23	0.83
	2	2.15	1.33	1.26	0.84
	3	2.28	1.38	1.33	0.88
VSAT unc. syst. error	all	0.28	0.17	0.16	0.11
(permille)	1	0.50	0.29	0.28	0.18
	2	0.48	0.29	0.28	0.19
	3	0.51	0.31	0.30	0.20
VSAT cor. syst. error	all	0.34	0.42	0.37	0.09
(permille)	1	0.41	0.52	0.26	0.22
	2	0.33	0.41	0.49	0.19
	3	0.36	0.43	0.47	0.11
VSAT tot. syst. error	all	0.44	0.45	0.41	0.14
(permille)	1	0.64	0.59	0.38	0.29
	2	0.58	0.50	0.56	0.26
	3	0.62	0.53	0.56	0.22
VSAT total error	all	1.35	0.89	0.84	0.51
(permille)	1	2.31	1.43	1.29	0.88
	2	2.23	1.42	1.38	0.88
	3	2.36	1.48	1.44	0.91
STIC error (permille)	all	3.24	1.94	1.85	1.24

Table 2: *STIC and VSAT luminosities.*

cut in real and simulated data. We also state the STIC error for comparison. The total VSAT error is significantly better than the STIC error. The values of the third, fourth and fifth column represent data taken at 45.66 GeV (peak), 44.74 GeV (peak-2) and 46.51 GeV (peak+2), respectively. The quantities in the last column refer to all energies.

4.2 Comparison with STIC

The main use of the VSAT measurement was to cross check the results of STIC. First, a comparison was made of the percentage of events registered in each minibunch (fig. 6). The measurements agree within the errors, of the order 0.1 %.

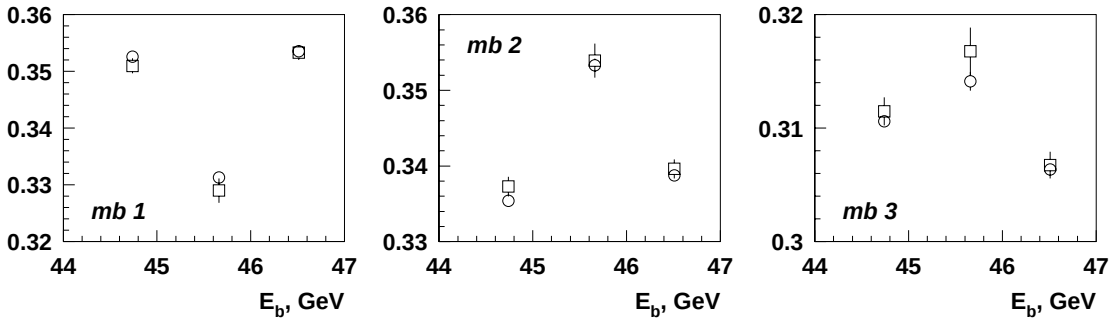

Figure 6: *Number of events in the three minubunches divided by the total number of events for the three nominal energies. The STIC data are shown by the squares and the VSAT data by the circles .*

The luminosity agreement can be confirmed by calculating the normalized differences at the three energy points and for the three minibunches separately. The results are given in fig. 7. The rms is close to unity for all distributions. We conclude that the two measurements have followed each other, as can also be seen in the correlation plots of fig. 8.

5 Conclusions

Due to reduced statistics, mainly at the peak position, the contribution of the VSAT result to the 1995 scan luminosity is only a marginal improvement. The result is consistent with that of STIC and with smaller errors thus reliably cross checking the latter measurement.

Acknowledgements

I wish to express my deepest gratitude to my supervisor G. Rinaudo for her invaluable guidance and support during this analysis. I would also like to thank S. Almehed for producing the simulated data and answering many questions throughout my work with the VSAT.

References

[1] Almehed et al., *A silicon tungsten electromagnetic calorimeter for LEP*, Nucl. Instr. Meth. A305 1991.

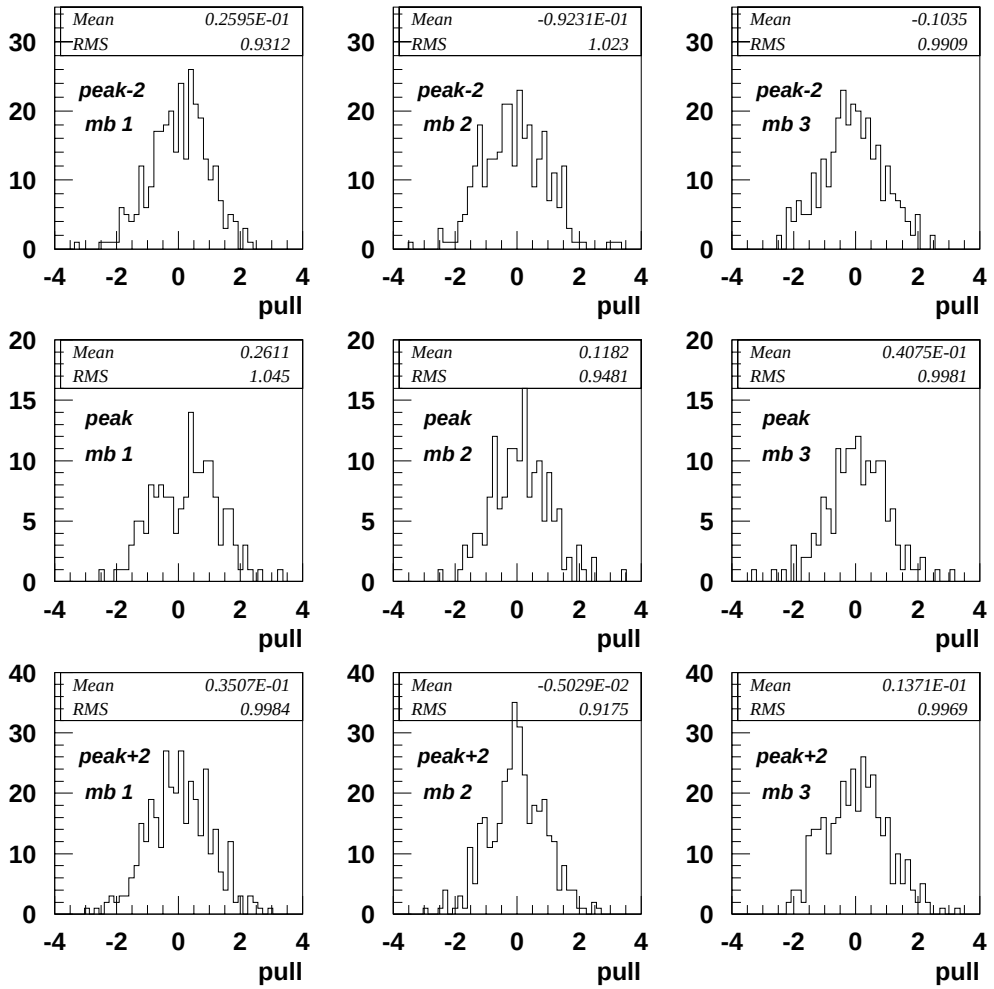

Figure 7: *Normalized differences for STIC and VSAT luminosities at the three beam energies and for the three minibunches.*

[2] Ch. Jarlskog, *VSAT energy calibration for 1995 minibunch data*, LUNFD6/(NFFL-7129) 1996.

[3] Ch. Jarlskog, *VSAT Off-line Minibunch Tagging for the 1995 Scan*, LUNFD6/(NFFL-7154) 1998.

[4] I. Kronkvist, *Data Base and Slow Controls System of the DELPHI VSAT and Two-Photon Physics using DELPHI at LEP*, PhD thesis, LUNFD6/(NFFL-7128) 1996.

[5] Ch. Jarlskog, G. Rinaudo, *Measurement of the beam parameters during the 1995 Z^0 scan with the DELPHI VSAT*, DELPHI note in preparation.

[6] A. Håkanson, *Luminosity Measurement at LEP using the Very Small Angle Tagger of DELPHI*, PhD thesis, LUNFD6/(NFFL-7077) 1993.

[7] Ch. Jarlskog, *Luminosity Measurement for the 1995 Z^0 scan with the Very Small Angle Tagger of DELPHI*, licentiate thesis, LUNFD6/(NFFL-7160) 1998.

[8] S. Almehed, private communication.

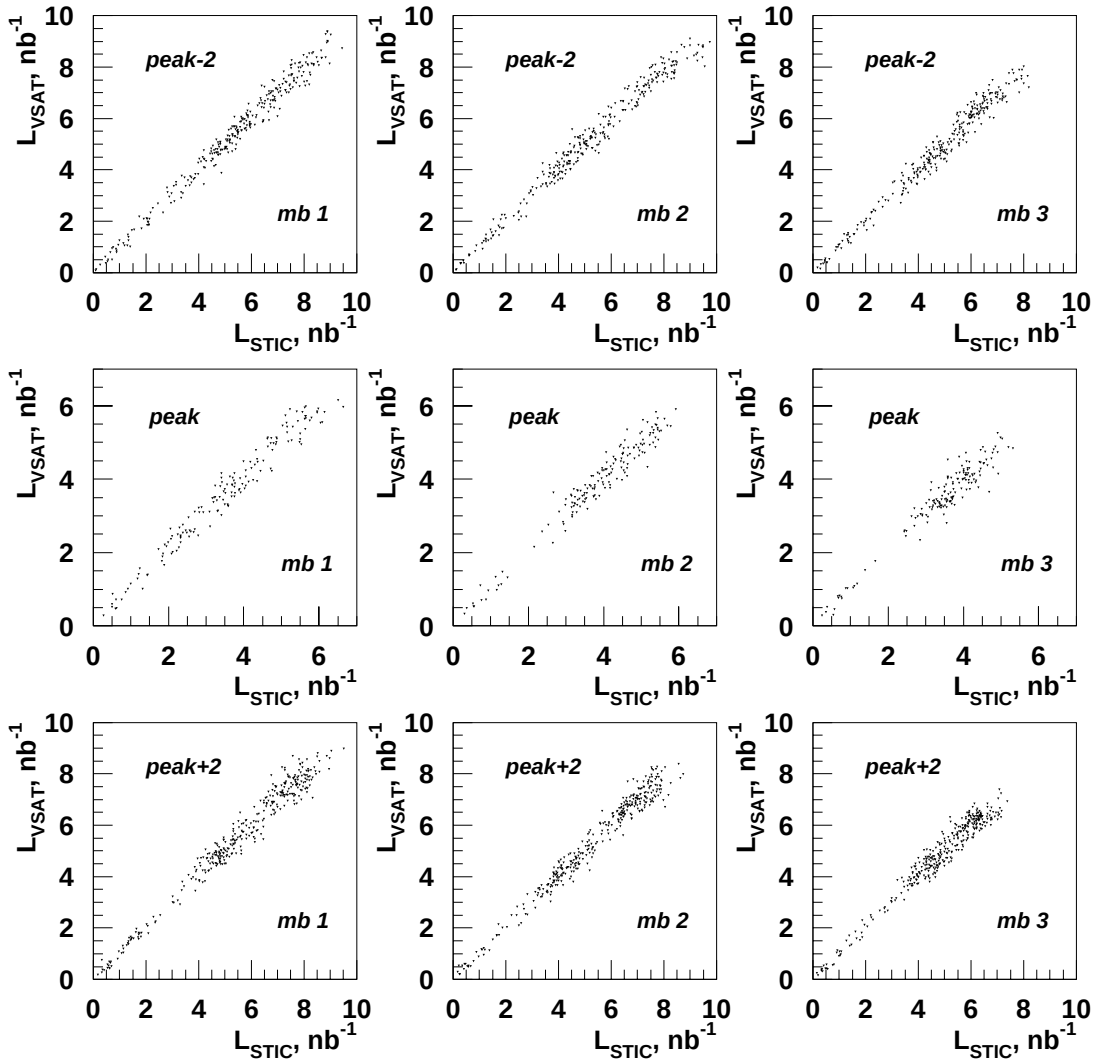

Figure 8: *Luminosity correlation plots at the three beam energies and for the three mini-bunches.*

[9] G. Rinaudo, private communication.

Appendix C

DELPHI Collaboration

DELPHI 2000-006 PHYS849
08 FEBRUARY 2000

Measurement of the beam parameters during the 1995 Z^0 scan with the DELPHI VSAT

Ch. Zacharatou Jarlskog
Lund University

Abstract

The beam parameter variations during the 1995 Z^0 scan obtained by the Very Small Angle Tagger (VSAT) luminometer are presented. The results are compared with the VD and TPC measurements.

1 Introduction

The Very Small Angle Tagger (VSAT) is one of the luminosity monitors of DELPHI [1]. It is an electromagnetic sampling calorimeter consisting of four rectangular modules called F1, F2 in the forward region and B1, B2 in the backward region. The distance of the modules from the DELPHI origin is approximately 7.7 m. The luminometers are placed symmetrically around a short elliptical section of the beam pipe as shown in fig. 1. The process seen by the detector is Bhabha scattering, i.e. electrons and positrons emitted back-to-back carrying approximately the beam energy. We therefore look for coincidences of signals between a module in the forward region and a module in the backward region, defining two diagonals for the trigger: diagonal 1 (modules F1-B2) and diagonal 2 (modules F2-B1).

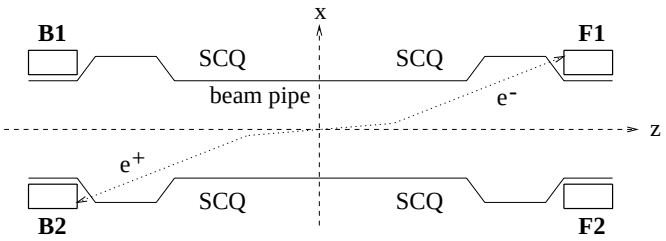

Figure 1: *Layout of the VSAT modules in the (x,z) plane.*

The dimensions of the calorimeters are 3 cm in x, 5 cm in y and approximately 10 cm in z. Each module contains 12 tungsten absorbers interspaced with 12 silicon planes for energy measurement (FADs). The center of the electromagnetic shower is given by three silicon strip planes with 1 mm pitch placed close to the shower maximum at 5, 7 and 9 r.l.; the second plane is used for the y coordinate measurement and the other two planes for the x coordinate measurement.

The detector has an azimuthal coverage of $\pm$ 45 degrees. The polar angles seen by the modules are from 5 to 7 mrad, a region of high Bhabha cross section. This allows the monitoring of the variation of beam parameters with high statistics.

In section 2, we give a short description of the variables used in the analysis, as more detailed accounts have been given in previous reports [2,3]. In sections 3 and 4, the determination of the x and z beamspot is discussed, respectively. The variations of the beam tilts and of the acollinearity are presented in section 5. Finally, section 6 presents beam parameter results for individual minibunches.

2 Measurement in the (x,z) plane

The analysis is based on the measurements of the x and y coordinates of the impact points of the outgoing particles on the four modules. In this section, we will see how these measurements are affected by the various beam parameters in the (x,z) plane.

In the general case, the beam has a displacement both in x and in z equal to x_b and z_b, respectively. Moreover, the incoming electron and positron are expected to have directions at nonzero angles with respect to the z axis. These angles are called tilts and are denoted by θ^x_+ for the positron and by θ^x_- for the electron. If the production angle of

the outgoing particles in diagonal 1 (2) is θ_1^x (θ_2^x), the x coordinates of the impact points on the modules will be

$$x_{F1} = f_x(x_b - z_b(\theta_1^x + \theta_-^x)) + l_x(\theta_1^x + \theta_-^x) \qquad x_{B2} = f_x(x_b - z_b(\theta_1^x + \theta_+^x)) - l_x(\theta_1^x + \theta_+^x)$$
$$x_{B1} = f_x(x_b + z_b(\theta_2^x - \theta_+^x)) + l_x(\theta_2^x - \theta_+^x) \qquad x_{F2} = f_x(x_b + z_b(\theta_2^x - \theta_-^x)) - l_x(\theta_2^x - \theta_-^x) \tag{1}$$

In the derivation of the above equations, we have represented the trajectories of the outgoing particles as straight lines. This entails the introduction of an effective distance, $l_x = (12.60 \pm 0.02)\ m$, of the front face of the modules from the DELPHI origin. This distance is larger than the real one because of the defocusing effect of the superconducting quadrupoles in the (x,z) plane. This effect is also reflected in the magnification factor $f_x = 2.1 \pm 0.1$, which multiplies the x beamspot value.

The electron and positron tilts can be rephrased in terms of two new beam parameters, the average tilt, θ_x, and the acollinearity, ϵ_x. We define them as

$$\theta_x = \frac{\theta_+^x + \theta_-^x}{2} \qquad \epsilon_x = \theta_-^x - \theta_+^x \tag{2}$$

Eqs. 1 can now be combined into the two following measures

$$\Delta x_1 = x_{F1} + x_{B2} = 2 \cdot f_x(x_b - z_b(\theta_1^x + \theta_x)) + \epsilon_x l_x$$
$$\Delta x_2 = x_{F2} + x_{B1} = 2 \cdot f_x(x_b + z_b(\theta_2^x - \theta_x)) + \epsilon_x l_x \tag{3}$$

With a view to extracting information on x_b and z_b separately, we introduce the variables

$$\Delta x = \frac{\Delta x_1 + \Delta x_2}{2} = 2 \cdot f_x x_b + \epsilon_x l_x + f_x z_b(\theta_2^x - \theta_1^x - 2\theta_x) \tag{4}$$

$$\delta x = \Delta x_2 - \Delta x_1 = 2 \cdot f_x z_b(\theta_1^x + \theta_2^x) \tag{5}$$

The production angles in the two diagonals have essentially equal values (5.5 $mrad$ approximately) and since the mean tilt is generally small this allows for the third term in eq. 4 to be neglected. Δx thus reflects the variations of both the x beamspot and the acollinearity. The two parameters cannot be separated with VSAT information only. On the other hand, eq. 5 provides us with a very efficient way to measure the z beamspot, the sum of the production angles being calculated directly from our data, as explained in section 4.

Before we proceed to the beam parameter calculation, it must be noted that the variables Δx_1 and Δx_2 are averages over the time required to write one cassette of data (about 15 minutes). As the corresponding distributions are affected by the variation of beam parameters, the average values Δx_1 and Δx_2 must be corrected in order for this variation to be taken into account. FASTSIM simulation runs have shown that the correction for the effect of the beam width and divergence variations can be parametrized in terms of the widths of the Δx_1 and Δx_2 distributions, $R\Delta x_1$ and $R\Delta x_2$, while the correction for the y tilt can be achieved by using the Δy_1 and Δy_2 variables (defined for the (y,z) plane in a similar way to eqs. 3) [4]:

$$\Delta x_{1C} = \Delta x_1(1 + 0.1(R\Delta x_1 - 2.6)) - 0.1(\Delta y_1 + 7)$$
$$\Delta x_{2C} = \Delta x_2(1 + 0.1(R\Delta x_2 - 2.8)) - 0.05(\Delta y_2 + 8)$$

where all quantities are measured in mm. Consequently, the variables Δx and δx should be replaced by the quantities $\Delta x_C = (\Delta x_{1C} + \Delta x_{2C})/2$ and $\delta x_C = \Delta x_{2C} - \Delta x_{1C}$, respectively.

3 Variation of the x beamspot

As was mentioned in the previous section, the x beamspot and acollinearity cannot be disentangled. We can, nevertheless, apply eq. 4 for the corrected value, Δx_C, in order to obtain an estimation of the variations of the x beamspot. If we define the approximate value of the x beamspot as $x_{VSAT} = \frac{\Delta x_C}{2 f_x}$, eq. 4 will give

$$x_{VSAT} = x_b + \epsilon_x \frac{l_x}{2 f_x} + x_0 \tag{6}$$

where the term x_0 corresponds to the third term of eq. 4 and is thus negligible. The distribution of x_{VSAT} and its variation with fill number are given in fig. 2. One entry in the plots corresponds to one cassette. The mean value for the scan is $(0.162 \pm 0.055)\ mm$. The accuracy for the measurement per fill is $(28 \pm 12)\ \mu m$.

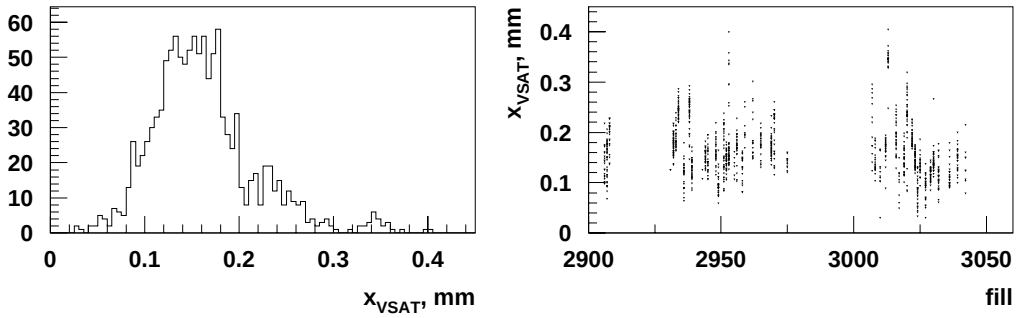

Figure 2: *x_{VSAT} with corrections for the beam width, divergence and y-tilt. The x-acollinearity effect is neglected.*

We can confirm the variation of our estimate by comparing with the x beamspot determination done by VD. The correlation plot is given in fig. 3(a). The linear relation is evident. The presence of the undetermined acollinearity term is clearly evidenced by fig. 3(b), which shows the normalized difference of the two measurements having an rms value significantly larger than unity.

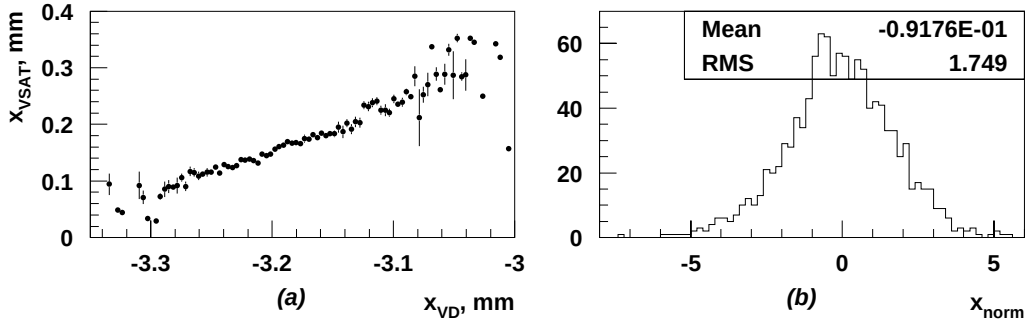

Figure 3: *(a) Correlation plot for the x_{VSAT} and x_{VD} measurements and (b) their normalized difference.*

4 Determination of the z beamspot

The advantage of eq. 5 over eq. 4 is that the acollinearity terms of eqs. 3 have been eliminated. If we substitute δx_C for δx and z_{VSAT} for z_b in eq. 5 we obtain

$$z_{VSAT} = \frac{\delta x_C}{2 f_x (\theta_1^x + \theta_2^x)} \tag{7}$$

Eqs. 1 can provide us with the sum in the denominator

$$\theta_1^x + \theta_2^x = \frac{x_{F1} - x_{B2} - x_{F2} + x_{B1}}{2 \cdot l_x} \tag{8}$$

The resulting distribution for z_{VSAT} and its variation are shown in fig. 4. The overall mean value is $(-47.8 \pm 4.4)\ mm$. The accuracy per fill is $(2.4 \pm 0.6)\ mm$.

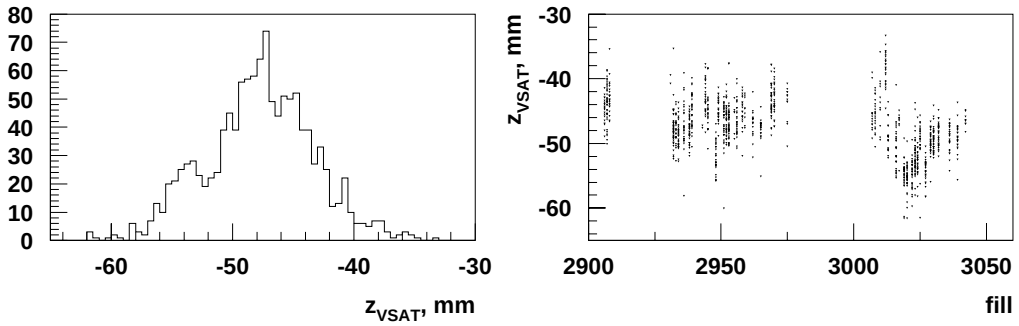

Figure 4: *z_{VSAT} with corrections for the beam width, divergence and y-tilt.*

The comparison with the TPC result is illustrated in fig. 5. The correlation plot demonstrates the qualitative agreement of the two measurements. The rms of the normalized difference confirms that there are no unaccounted effects.

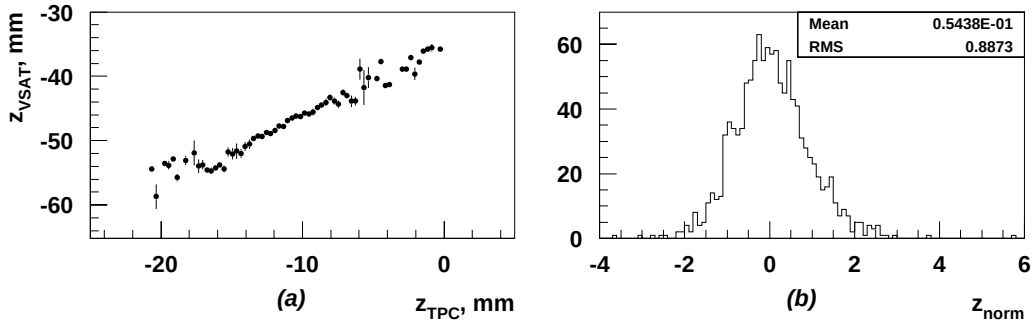

Figure 5: *(a) Correlation plot for the z_{VSAT} and z_{TPC} measurements and (b) their normalized difference.*

5 Variations of acollinearity and tilt

The VD and VSAT measurements can be combined to extract the values of the acollinearity in the (x,z) and (y,z) planes. Neglecting the third term of eq. 4, we obtain

$$\epsilon_x \approx \frac{\Delta x_C - 2 f_x \cdot x_{VD}}{l_x} \tag{9}$$

A similar equation holds in the vertical plane. In eq. 9, we have replaced Δx by Δx_C and introduced the VD measurement for the x beamspot. The variations of ϵ_x and ϵ_y are given in fig. 6. The mean values are $(0.905 \pm 0.012)\ mrad$ and $(-2.101 \pm 0.023)\ mrad$, respectively.

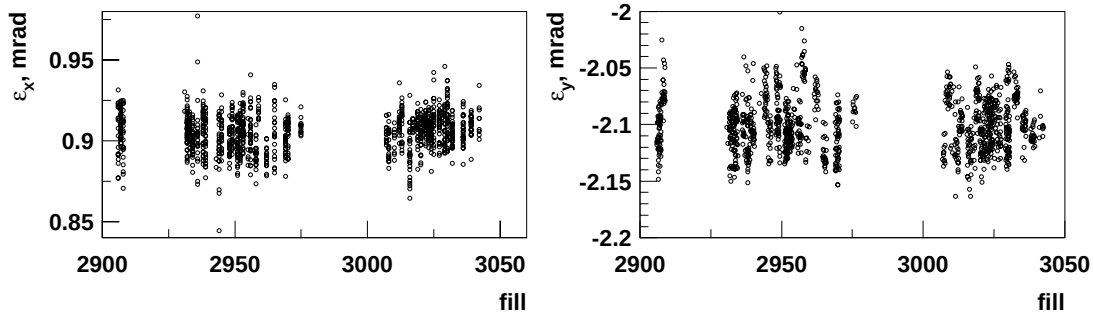

Figure 6: *Variations of ϵ_x and ϵ_y.*

Another measurement that can be performed by the detector is that of the mean beam tilts in the two planes, θ_x (eq. 2) and θ_y. Simulations with FASTSIM have established a relation between the x tilt and the asymmetry [4], A_D,

$$\theta_x\ (mrad) = 1.75 \cdot A_D \tag{10}$$

where the asymmetry is defined as the fractional difference of the number of Bhabha events in the two diagonals of the detector. Moreover, the y tilt is extracted directly from the y coordinates of the impact points on the four modules:

$$y_{F1} + y_{F2} - y_{B1} - y_{B2} = 2f_y z_b(\theta^y_+ - \theta^y_-) + 2l_y(\theta^y_1 - \theta^y_2 + \theta^y_- + \theta^y_+) =$$

$$= -2f_y z_b \epsilon_y + 2l_y(\theta^y_1 - \theta^y_2) + 4l_y\theta_y \approx 4l_y\theta_y$$

and therefore

$$\theta_y \approx (y_{F1} + y_{F2} - y_{B1} - y_{B2})/4l_y \tag{11}$$

Fig. 7 shows the results of eqs. 10 and 11. The average value of θ_x is $(-0.082 \pm 0.038)\ mrad$, whereas θ_y has a mean value of $(0.462 \pm 0.076)\ mrad$.

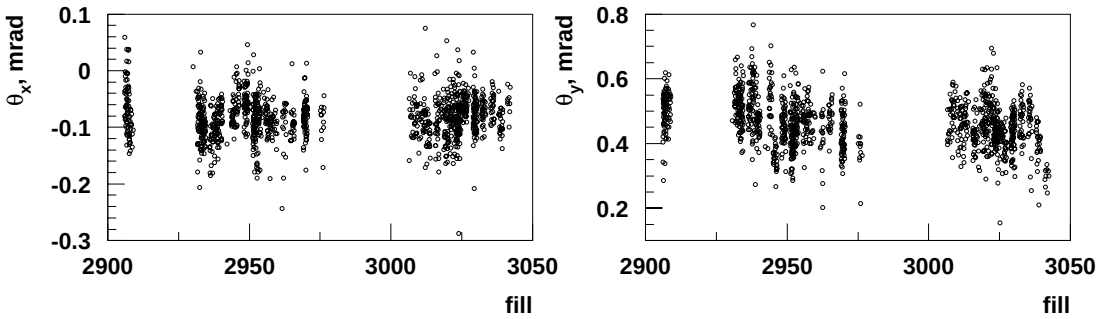

Figure 7: *Variations of θ_x and θ_y.*

As the tilt values above represent only average beam directions, it is useful to determine also the spread around these directions, i.e. the beam divergence. This measurement is not

possible in the vertical plane because of the quadrupole effect. On the other hand, eq. 4 can give the variations of the divergence in the horizontal plane through the dispersion $\sigma_{\Delta x}$ of the Δx distribution. This result is shown in fig. 8.

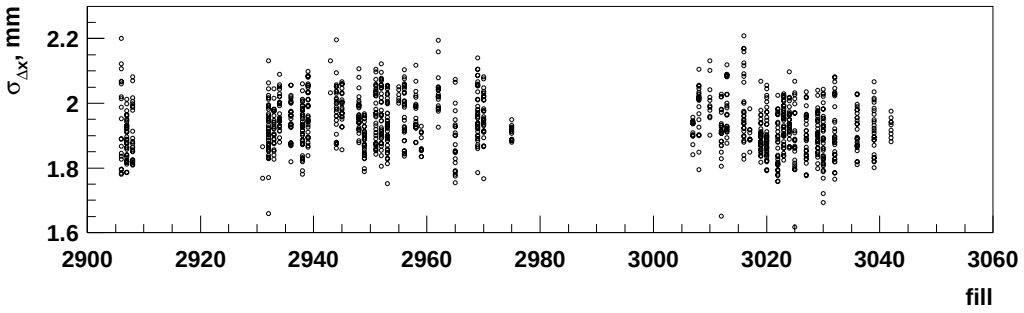

Figure 8: *Variation of* $\sigma_{\Delta x}$.

6 Beam parameters for minibunches

As 1995 was the first year LEP ran in the minibunch scheme, it is of interest to examine whether the three minibunches exhibited differences in their beam parameter characteristics. Since the VD has not supplied beamspot information per minibunch, we cannot perform the calculation of the acollinearity. However, the distributions of x_{VSAT} and z_{VSAT} as well as the mean tilts in the two planes can be extracted from VSAT data alone for the three minibunches. The results are shown in fig. 9. We observe no dependence on minibunch number.

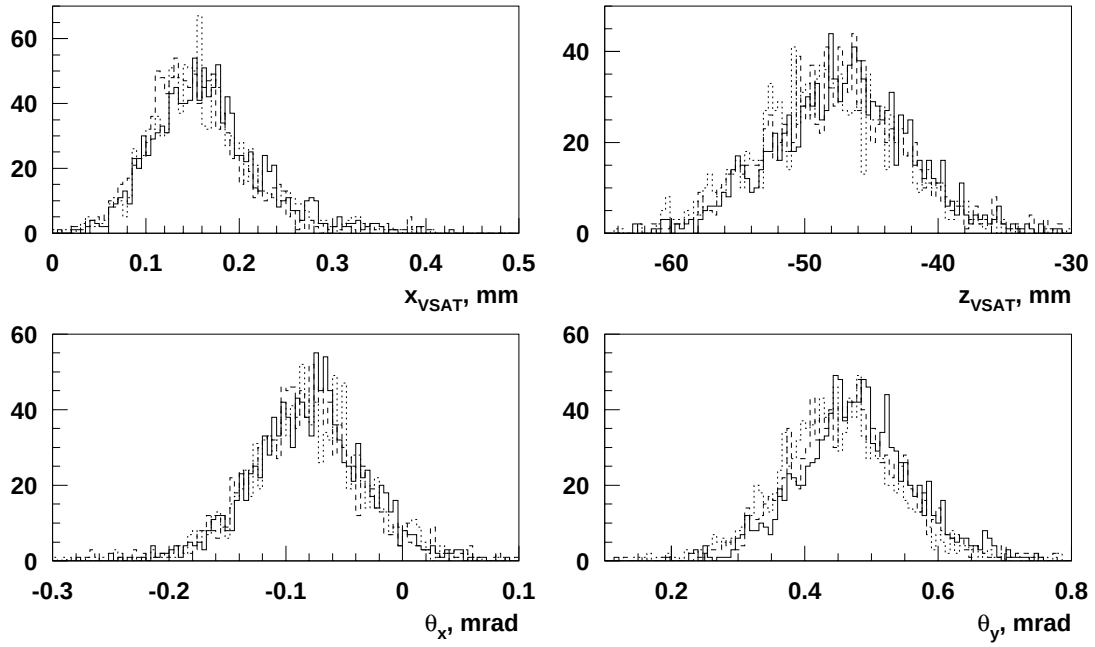

Figure 9: *VSAT beam parameters for minibunch one (solid lines), two (dashed lines) and three (dotted lines).*

7 Conclusions

The x and z beamspot variations have been successfully measured and compared with the results of VD and TPC. The average beam directions have also been calculated in the horizontal and vertical planes. The combination of VD and VSAT data has provided information on beam acollinearities. Beam parameters per minibunch have also been determined. These results have been used for the luminosity analysis [5].

References

[1] Almehed et al., *A silicon tungsten electromagnetic calorimeter for LEP*, Nucl. Instr. Meth. A305 1991.

[2] Almehed et al., *Measurement of the beam parameter variations in DELPHI with the VSAT*, DELPHI 95-150 LEDI 2.

[3] Ch. Jarlskog, *Interaction point estimation and beam parameter variations in DELPHI with the VSAT* , LUNFD6/(NFFL-7110)1995.

[4] S. Almehed, private communication.

[5] DELPHI note in preparation.

Appendix D

LU TP 01-13
LUNFD6/(NFFL-7194)2001

Hadronization corrections to helicity components of the fragmentation function

T. Sjöstrand[1], O. Smirnova[2*] and Ch. Zacharatou Jarlskog[2]

[1]Department of Theoretical Physics, Lund University, Sölvegatan 14A, S 22362 Lund, Sweden
[2] Department of Elementary Particle Physics, Lund University, P.O.Box 118, S 22100 Lund, Sweden

Abstract

In the hadronic decays of Z^0, gluon emission leads to the appearance of the longitudinal component of the fragmentation function, F_L. Measurement of F_L and the transverse component, F_T, could thus provide an insight into the gluon fragmentation function. However, hadronization corrections at low x can be significant. Here we present a method of accounting for such corrections, using the JETSET event generator as illustration.

Submitted to European Physics Journal C

* *On leave from:* JINR, 141980 Dubna, Russia

1 Introduction

Studies of fragmentation functions have always been important, since these distributions can not be predicted theoretically, but only be measured experimentally, and consecutively be described by phenomenological models. Hadronic decays of γ^*/Z^0 provide a particularly convenient set of events for analysis and interpretation. Helicity components of the fragmentation function, measured in such events, can be used in various QCD studies, e.g., the extraction of the gluon fragmentation function, and the evaluation of α_s. However, existing theoretical calculation being restricted to the perturbative region, hadronization corrections must be taken into account. In what follows, methods for applying such corrections using the JETSET event generator [1] as an example, will be discussed.

Consider the angular distribution in the process $e^+e^- \to \gamma^*/Z^0 \to q\overline{q}$ in its rest frame. Assuming that the final quark and antiquark are not charge-tagged, i.e. that the forward–backward asymmetry is not accessed, the cross section can be written as [2]

$$\frac{\mathrm{d}\sigma}{\mathrm{d}(\cos\theta)} = \frac{3}{8}\,(1+\cos^2\theta)\,\sigma_{\mathrm{T}} + \frac{3}{4}\,\sin^2\theta\,\sigma_{\mathrm{L}}\ . \tag{1}$$

Here σ_{T} (σ_{L}) is the cross section associated with a transverse (longitudinal) gauge boson polarization state with respect to the $q\overline{q}$ axis, and θ is the polar angle of a particle with respect to the incoming lepton axis. To lowest order, only mass effects contribute to a non-vanishing σ_{L}, but only for the vector part of the cross section, and there only with a coefficient $\sigma_{\mathrm{L}}/\sigma_{\mathrm{T}} = 2m_q^2/E_{\mathrm{cm}}^2$. Even for the b quarks this gives a negligible σ_{L} contribution at the energies around the Z^0 peak. Therefore, σ_{L} effectively starts in $\mathcal{O}(\alpha_{\mathrm{s}})$ of perturbation theory, associated with the emission of gluons.

Since partons are not directly observable, one may define a hadron-level analogue of Eq.(1) [3],

$$\frac{\mathrm{d}^2\sigma^{\mathrm{h}}}{\mathrm{d}x\,\mathrm{d}(\cos\theta)} = \frac{3}{8}\,(1+\cos^2\theta)\,\frac{\mathrm{d}\sigma_{\mathrm{T}}}{\mathrm{d}x} + \frac{3}{4}\,\sin^2\theta\,\frac{\mathrm{d}\sigma_{\mathrm{L}}}{\mathrm{d}x}\ . \tag{2}$$

Here x would preferably be associated with the energy fraction taken by a hadron, $x_E = 2E/E_{\mathrm{cm}}$, so that $\sum x_E = 2$ in each event. Experimentally it is more convenient to use the momentum fraction x_p. The transverse and longitudinal fragmentation functions are defined by a normalization to the total cross section $\sigma_{\mathrm{tot}} = \sigma_{\mathrm{T}} + \sigma_{\mathrm{L}}$ [4],

$$F_{\mathrm{T}}(x) = \frac{1}{\sigma_{\mathrm{tot}}}\frac{\mathrm{d}\sigma_{\mathrm{T}}}{\mathrm{d}x}\ , \qquad F_{\mathrm{L}}(x) = \frac{1}{\sigma_{\mathrm{tot}}}\frac{\mathrm{d}\sigma_{\mathrm{L}}}{\mathrm{d}x}\ . \tag{3}$$

The former is dominated by the fragmentation of quark jets, whereas the latter receives a major contribution from gluon fragmentation. Therefore an experimental determination of $F_{\mathrm{L}}(x)$ is a first step towards an extraction of the gluon fragmentation function, alternative to what is offered by more direct methods in three-jet events [5]. Several experimental $F_{\mathrm{L}}(x)$ studies have also been presented [6].

A complication is that hadrons are not moving in the direction of their imagined mother parton. Already in lowest order of perturbation theory, for $q\overline{q}$ two-jet events, nonperturbative hadronization gives an effective $p_\perp$ smearing that induces a nonvanishing $F_{\mathrm{L}}(x)$ even where none is expected. Furthermore, the association

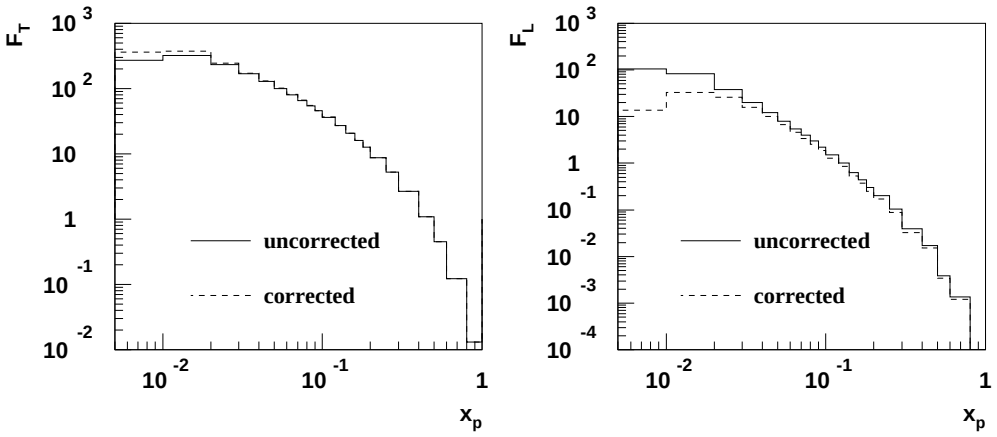

Figure 1: *$F_T(x_p)$ and $F_L(x_p)$ for corrected (smeared) hadron angles (dashed lines) and for uncorrected (non-smeared) hadron angles (solid lines).*

of a hadron to a single mother parton is not in agreement with our current best understanding of the hadronization process, where it is rather the colour field between a colour-connected pair of partons (a string piece [7], or a cluster [8]) that mediates the hadron production. Therefore the structure of smearing effects may become rather nontrivial. Obviously, the effects are especially important at small x, which is also the region where one would hope to have some sensitivity to the gluon fragmentation function. The string picture also casts in doubt the concept of a gluon fragmentation function defined from inclusive quantities, since the string fragmentation of a parton depends on the angles to other colour-connected partons.

The issue of hadronization corrections to fragmentation functions was addressed in [4, 9]. The emphasis was on the $\sigma_{\rm L}$ that can be extracted from $\int_0^1 F_{\rm L}(x)\,x\,{\rm d}x$ rather than on $F_{\rm L}(x)$ itself, however. Therefore we here address how hadronization affects $F_{\rm L}(x)$ (and $F_{\rm T}(x)$). One main conclusion is that a simple smearing approach is not sufficient to describe hadronization effects. Thus it appears impossible to define a completely model-independent, hadronization-smearing-corrected $F_{\rm L}(x)$, that could be used to extract a gluon fragmentation function. We further suggest a correction procedure, based on a cluster search strategy, that should give a less model dependent $F_{\rm L}(x)$, but at the price of introducing the cluster resolution scale y as a new parameter in the problem.

2 The simple smearing

The string model description of $q\overline{q}$ events introduces a Gaussian transverse momentum smearing of primary hadrons, $\propto \exp(-p_\perp^2/2\sigma^2)\,{\rm d}^2p_\perp$, where $\sigma \approx 0.36$ GeV [1, 10]. Many primary hadrons are unstable and decay further; this distorts the original Gaussian spectrum and reduces the average $p_\perp$. Since decay products have smaller $p_\parallel$, momentum parallel to the jet axis, some correlation is also introduced between $p_\perp$ and $p_\parallel$. Therefore no simple parameterization is proposed, but instead a Monte

Carlo simulation with JETSET 7.4 [1] is used to histogram the amount of angular smearing for different x_p bins.

It is now assumed that this smearing should be applied both to quark and gluon jets, so that a hadron will not move exactly in the direction of its mother parton. There are obvious shortcomings to equating different kinds of jets, like that gluon jets have a lower energy and do not contain decays of charm and bottom hadrons, but those particular issues only introduce moderate corrections. More severe objections can be raised to the association of hadrons to individual partons, as we will discuss further in the next section, but forget for the moment.

Had particles not been smeared in $p_\perp$, but parallel with their parton of origin, the shape of the angular distribution

$$F(x_p, \cos\theta) = \frac{3}{8}\,(1+\cos^2\theta)\,F_{\mathrm{T}}(x_p) + \frac{3}{4}\,\sin^2\theta\,F_{\mathrm{L}}(x_p) \tag{4}$$

in a bin of x_p could be used to extract $F_{\mathrm{T}}(x_p)$ and $F_{\mathrm{L}}(x_p)$ in that bin. The abovementioned smearing will now modify this. The two angular shapes, $(3/8)\,(1+\cos^2\theta)$ and $(3/4)\,\sin^2\theta$, both normalized to unity, are therefore convoluted with the x_p-dependent smearing distributions, characterized by a distribution in the smearing angle θ^{sm} and an isotropic azimuthal distribution φ^{sm}. That is, a parton at an angle θ^{p} will produce a hadron at an angle θ^{h}, where

$$\cos\theta^{\mathrm{h}} = \cos\theta^{\mathrm{p}}\,\cos\theta^{\mathrm{sm}} - \sin\theta^{\mathrm{p}}\,\sin\theta^{\mathrm{sm}}\,\cos\varphi^{\mathrm{sm}}\ . \tag{5}$$

Data can now be fitted both to the "non-smeared" angular distribution form, Eq.(4), and to the convoluted ("smeared") analogue. The resulting distributions for F_T and F_L, obtained using the JETSET generated events, are shown in Fig. 1. The effect on F_T and F_L is visible for hadron momenta below 10% of the beam energy. The low momentum region is affected the most, giving F_L values reduced up to one order of magnitude.

3 Objections to the simple smearing

The above smearing procedure is correct to lowest order in α_{s}, i.e. it describes how two-jet events can induce a nonvanishing $F_{\mathrm{L}}(x_p)$. We know, however, that hadronization of three-jet events cannot be described in terms of a simple incoherent sum of three q, $\overline{q}$ and g jets. One example is the string/drag effect [11, 12], i.e. that particle production is suppressed in the angular region between the q and $\overline{q}$ and enhanced in the other two regions, well confirmed experimentally [13]. High-momentum hadrons still essentially follow the separate parton directions, but low-momentum ones are significantly affected. These are the ones where the angular smearing effects are large to begin with. It is well-known that the string effect leads to more two-jetlike events, e.g. in terms of thrust T, than implied by symmetric smearing [14]. The reason is to be found in the enhanced production of particles between two colour-connected partons that are close in angle, leading to them seemingly being even closer, e.g. that the opening angle between the reconstructed jets typically is smaller than that between the original partons.

There is a nontrivial topology dependence on string effects, especially when multiple gluon emission is considered. The issue is therefore best studied in an

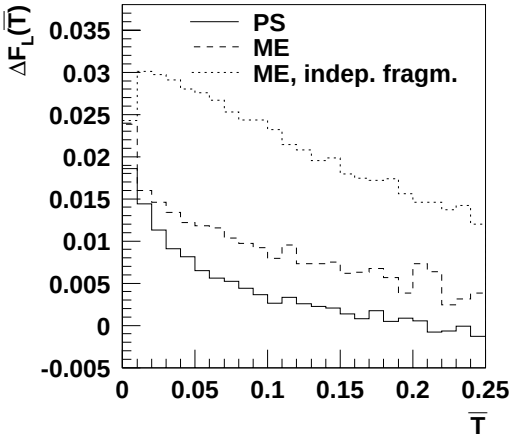

Figure 2: *Event-by-event hadronization corrections* $\Delta F_{\rm L}(\overline{T}) = F_{\rm L}^{\rm h}(\overline{T}) - F_{\rm L}^{\rm p}(\overline{T})$ *for different simulations: solid line corresponds to* JETSET *7.4 PS, dashed –* JETSET *7.4 ME (both using the string fragmentation), and dotted –* JETSET *7.4 ME with independent fragmentation scheme.*

event generator, by comparing angular distributions on the parton (i =p below) and on the hadron (i =h) level. As a simple measure of the jettiness of events we use $\overline{T} = 1 - T$, defined on the parton level of each event. The integrated x_E spectrum is decomposed as

$$\left(\frac{\mathrm{d}\sigma_{\rm tot}}{\mathrm{d}\overline{T}}\right)^{-1} \int_0^1 \frac{\mathrm{d}^3\sigma^i}{\mathrm{d}\overline{T}\,\mathrm{d}x_E\,\mathrm{d}(\cos\theta)}\, x_E\,\mathrm{d}x_E \;\; = \\ = \frac{3}{8}\,(1+\cos^2\theta)\,F_{\rm T}^i(\overline{T}) + \frac{3}{4}\,\sin^2\theta\,F_{\rm L}^i(\overline{T}) \qquad , \tag{6}$$

where the x_E-weighting ensures a common normalization $F_{\rm T}^i(\overline{T}) + F_{\rm L}^i(\overline{T}) = 2$ at parton and hadron level (values of $F_{\rm T}^i$ and $F_{\rm L}^i$ most conveniently are obtained by weighting each particle with an appropriate angular factor [4]). Then $\Delta F_{\rm L}(\overline{T}) = F_{\rm L}^{\rm h}(\overline{T}) - F_{\rm L}^{\rm p}(\overline{T})$ is a simple measure of the hadronization impact on $F_{\rm L}$. This quantity is shown in Fig. 2, for one realistic simulation and two toy ones, for $u\overline{u}$ events at 91.2 GeV. In the realistic case, a parton shower is used to generate multiparton configurations, followed by string fragmentation. The shower develops down to a cut-off scale $Q_0 \approx 1$ GeV, so that also events in the first bin, $\overline{T} < 0.01$, can contain some gluons. The other two histograms are based on $\mathcal{O}(\alpha_{\rm s})$ matrix elements, where only 2- and 3-parton configurations are generated, with a cut $\overline{T} > 0.01$ on the latter to avoid the singularities of the 3-parton matrix element. Thus the first bin here represents pure 2-parton events. While one simulation is again based on string fragmentation, the other assumes isotropic smearing around the jet axes, basically the independent fragmentation scheme of Hoyer et al. [15, 14]. (The same fragmentation parameters, tuned to the shower model, have been used in all three cases. A retuning of parameters for the $\mathcal{O}(\alpha_{\rm s})$ simulations would have given a larger nonperturbative $p_\perp$ width σ to cover for the lack of perturbative gluons, and so would have implied even larger fragmentation smearing.)

The isotropic smearing is, as expected, giving a rather constant hadronization correction $\Delta F_{\mathrm{L}}(\overline{T})$. There is some jump up in going from two to three jets that are smeared, followed by a slow but steady drop with $\overline{T}$, since the longitudinal component itself is increasing in importance with $\overline{T}$ and therefore gives an increasing hadronization smearing of the longitudinal component onto the transverse one rather than only the other way around. By contrast, the string fragmentation provides a much steeper drop of ΔF_{L} with $\overline{T}$, kicking in immediately when going from two to three partons, and enhanced in the shower simulation relative to the simpler $\mathcal{O}(\alpha_{\mathrm{s}})$ one. At large $\overline{T}$ the overall hadronization correction can even turn negative. Averaging over the $\overline{T}$ spectrum (with mean value $\langle\overline{T}\rangle \approx 0.05$), we conclude that the typical hadronization smearing contribution is only about a third of the naively expected one, as obtained from two-parton results. (Qualitatively this agrees with and probably explains a similar observation in [4] of smaller-than-expected hadronization corrections when using HERWIG [16].) That is, if hadronization corrections are viewed as a power series in α_{s}, the $\mathcal{O}(\alpha_{\mathrm{s}})$ term is of opposite sign and almost as big as the $\mathcal{O}(1)$ one.

It should be remembered, however, that this is integrated over all x_E, and that we have no similar way of addressing results in specific x bins, since the parton and hadron x spectra are quite different. Thus it is likely that the $F_{\mathrm{L}}(x_p)$ derived in the previous section is an underestimation, just like an $F_{\mathrm{L}}(x_p)$ found without any smearing corrections is likely to be an overestimation, but it appears impossible to find the "correct" $F_{\mathrm{L}}(x_p)$ without making detailed assumptions about the hadronization process.

4 Clustering

Given the problems with the above smearing recipe, we introduce a new strategy, based on the clustering approach. In a nutshell, we propose to rotate all hadrons to the direction of the cluster they belong to, as an approximate way of removing hadronization smearing effects. Only thereafter is $F_{\mathrm{L}}(x)$ extracted from this modified $\cos\theta$ distribution. The strategy is explained further in the following.

In clustering algorithms, nearby hadrons are combined to form clusters/jets, in a way that should reflect the underlying partonic state, to some approximation. The combination process is controlled by (at least) one separation parameter, call it $y_{\min}$, such that the final state contains no pair of clusters closer to each other than that. Clustering algorithms can be applied also to a partonic state, and here $y_{\min}$ provides a regularization of soft and collinear divergences in the perturbative cross sections. It is then meaningful to calculate the distribution of partons at a factorization scale $\mu^2 = y_{\min}E_{\mathrm{cm}}^2$, and define scale-dependent fragmentation functions parameterizing the subsequent soft-perturbative and nonperturbative hadronization. The latter should obey standard QCD evolution equations, starting from some unknown nonperturbative form at a low reference scale.

Over the years many cluster algorithms have been proposed [17], each with its strengths and weaknesses. In this article we adopt the Durham one [18], which is a standard for many perturbative calculations. The distance measure between two

clusters i and j is

$$y_{ij} = \frac{2\min(E_i^2, E_j^2)(1-\cos\theta_{ij})}{E_{\rm vis}^2} \; , \tag{7}$$

so that $\sqrt{y_{ij}}$ roughly corresponds to the relative transverse momentum, scaled to the total visible energy $E_{\rm vis}$ ($= E_{\rm cm}$ for an ideal detector).

If we begin by considering a simple $q\overline{q}$ event, it should reconstruct back to two clusters, unless $y_{\rm min}$ has been chosen very small. Since the momentum of a cluster is given by the vector sum of its constituent hadrons, it would resum opposite and compensating $p_\perp$ kicks imparted to hadrons in the fragmentation process. The cluster direction should therefore be a better measure of the $q\overline{q}$ axis than that provided by the individual hadron momenta. It is the angular distribution of this axis that relates back to the polarization character of the $\gamma^*/Z^0 \to q\overline{q}$ decay, and that we want to be reflected in our extracted $F_{\rm L}(x)$ and $F_{\rm T}(x)$. Therefore it would be an improvement to rotate all hadrons in a cluster to sit along the cluster direction. That is, the θ of a hadron is redefined while its x value is unchanged.

At this level there is no contradiction with the smearing approach studied earlier. Then we smeared the simple partonic angular shapes to arrive at realistic hadronic ones to compare with data, now we un-smear the hadronic angles to approach the simple partonic distributions. There is one advantage, however: the clustering approach is not sensitive to the width of the $p_\perp$ distribution, i.e. the σ parameter, unlike the smearing procedure. Of course, the $p_\perp$ width still affects the typical error between the $q\overline{q}$ and cluster axes.

When considering multijet production, the $y_{\rm min}$ choice does become relevant, with $\mu^2 = y_{\rm min} E_{\rm cm}^2$ acting as a factorization scale, as noted above. For a large $y_{\rm min}$ all activity is clustered into the two quark jets, and neither the gluon structure nor $F_{\rm L}(x)$ would be probed. For $y_{\rm min} \to 0$ each hadron or parton is a cluster unto itself, and we are back at the starting point. So obviously some intermediate scale is to be preferred. Given that the typical hadronization $p_\perp$ width is ~ 0.4 GeV, with a tail to larger values, one would conclude that clustering up to $p_\perp \sim 1$ GeV would be a sensible minimum to eliminate the bulk of the hadronization $p_\perp$ smearing. At the Z^0 peak this translates into $y_{\rm min} \gtrsim 0.0001$. In the upper end, we want to stay with a picture of multiple gluon emission as the norm, i.e. retain $F_{\rm L}(x)$ as an inclusive quantity, in order not to overlap with traditional studies of gluon jets in exclusive three-jet events. Since the average number of clusters per event is three for $y_{\rm min} \approx 0.0025$, we conclude that $0.0001 \lesssim y_{\rm min} \lesssim 0.0025$ is a reasonable range, over which to study a scale-dependent $F_{\rm L}(x,\mu)$.

In Fig. 3, the distribution of event-by-event x_E-weighted and -integrated hadronization corrections $\Delta\sigma_{\rm L}/\sigma_{\rm tot} = (\sigma_{\rm L}^h - \sigma_{\rm L}^p)/\sigma_{\rm tot}$ is shown for some different $y_{\rm min}$ scales, for events generated with parton showers and string fragmentation (superscripts h and p stand for hadron and parton level, respectively). We note the significant width of these distributions, showing that event-by-event fluctuations in the hadronization process are important and can be of either sign. Even if small by comparison, the mean $\langle\Delta\sigma_{\rm L}/\sigma_{\rm tot}\rangle$ does show a systematic bias, positive for small $y_{\rm min}$ and negative for large $y_{\rm min}$. That is, at small $y_{\rm min}$ the hadronization smearing wins over the string effects, while it is the other way around for large $y_{\rm min}$ — but remember that this is only true when averaging over many events. Nevertheless, one possible criterion for a good choice of $y_{\rm min}$ would be where the two effects cancel, which then gives $y_{\rm min} \approx 0.0002$, i.e. $\mu \approx 1.3$ GeV. While a sensible reference value,

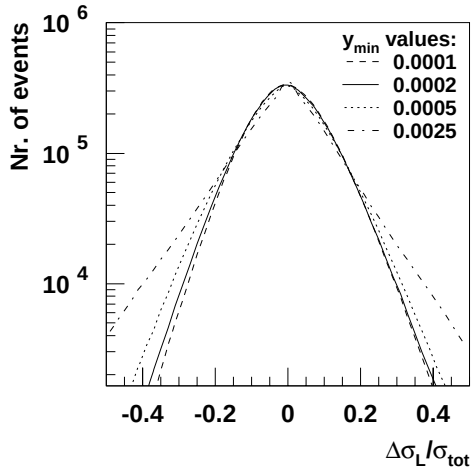

Figure 3: *Event-by-event hadronization corrections* $\Delta\sigma_{\rm L}/\sigma_{\rm tot} = (\sigma_{\rm L}^h - \sigma_{\rm L}^p)/\sigma_{\rm tot}$ *for different* $y_{\rm min}$ *scales (*JETSET *7.4 PS and string fragmentation).*

one should not take this particular value too seriously, since it is for one specific model, and for one specific set of model parameters. Somewhat different parameter values, like for the parton shower cut-off $Q_0 \approx 1$ GeV, defining the parton level of the events studied, could lead to slightly different "preferred" μ values.

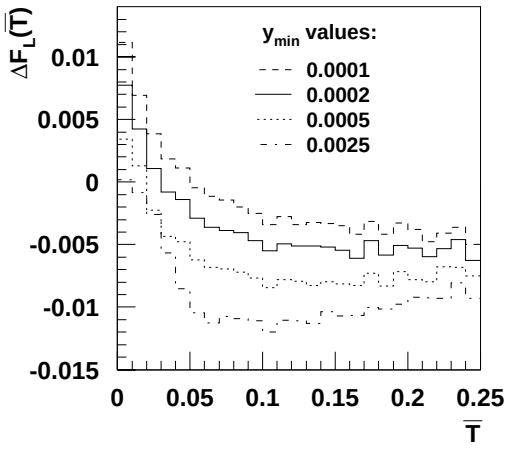

Figure 4: *Hadronization corrections* $\Delta F_{\rm L}(\overline{T}) = F_{\rm L}^{\rm h}(\overline{T}) - F_{\rm L}^{\rm p}(\overline{T})$ *for different* $y_{\rm min}$ *scales (*JETSET *7.4 PS and string fragmentation).*

It is important to note that we here have been considering the x-integrated quantity. This is of relevance if one e.g. would like to extract an $\alpha_{\rm s}$ from an $\sigma_{\rm L}$ measurement, and so not uninteresting. For the purpose of determining the differential x distribution, $F_{\rm L}(x)$, however, one would have reason to fear that any bias could have an x dependence that would not be caught. In the string model, a

string piece connecting two partons is boosted by an increasing velocity vector as the relative opening angle between the partons is decreased, and so the string effects spread upwards to larger x values. A warning signal is then that $\Delta F_{\rm L}$ does depend quite significantly on $\overline{T}$, Fig. 4, i.e. clustering does not reduce the $\overline{T}$ dependence noted in Fig. 2, but mainly shifts the overall level. Since $\overline{T}$ probes the topology of events, we also do expect this topology to reflect itself in an x dependence of hadronization corrections. As in the previous studies, this dependence is then likely to show up mainly in the lower end of the x range. At larger x, hadrons are rather well aligned with the jet axes, so, even with x-weighting, the few particles out there give a small contribution to the $\langle \Delta F_{\rm L} \rangle$. In Fig 5, the relative difference between the inclusive $F_L(x_p)$ and $F_L^{cluster}(x_p)$, obtained by replacing hadron angles with cluster angles for different y_{min} values, is shown. It is clearly seen, indeed, that the hadronization corrections are only important at low x_p, unless $y_{\rm min}$ is chosen too high. For the transverse component of the fragmentation function, $F_T(x_p)$, corrections have the same absolute amplitude but the opposite sign.

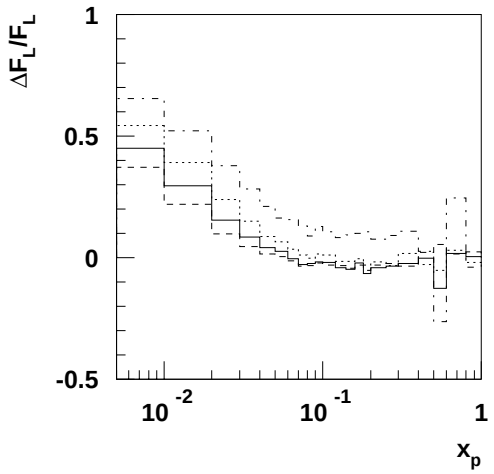

Figure 5: *Ratio* $\Delta F_{\rm L}/F_{\rm L} = (F_{\rm L} - F_{\rm L}^{cluster})/F_{\rm L}$ *for various* y_{min} *values: dashed line corresponds to* $y_{min} = 0.0001$*, solid –* $y_{min} = 0.0002$*, dotted –* $y_{min} = 0.0005$ *and dash-dotted –* $y_{min} = 0.0025$*.*

On the up side, the string effect has its perturbative equivalent in the colour dipole [12]. That is, asymmetries also exist in the production of soft gluons around the direction of the harder partons of an event. Such soft parton emission, below the cut-off scale $Q_0 \approx 1$ GeV we have used, would thus largely fill in the same regions as the nonperturbative hadron production, and with the same topology dependence. If one takes Local Parton-Hadron Duality [19] seriously, this equivalence should come very close. Our proposed strategy, to reset the θ angle of particles to that of the cluster they belong to, would be applicable also to such perturbatively calculated parton topologies.

5 Summary

The coherence phenomenon [20] kills the concept of gluon fragmentation functions that can be defined independently of the environment they are found in. The "hump-backed" shape of inclusive x spectra [19, 21] is an excellent illustration: by coherence the multiplication of partons/hadrons at small x is much less than if the hard partons could radiate/hadronize independently. The immediate consequence is that the expected "softer gluon than quark jets" picture is difficult to test. This impacts both on studies of gluon jets directly in identified three-jet events and indirectly via $F_{\mathrm{L}}(x)$. In this article we have illustrated some of these issues for the latter observable.

It appears safe to conclude that a straightforward extraction of $F_{\mathrm{L}}(x)$ from hadron angular distributions exaggerates the rate of particles at small x that should be attributed to gluon jets, since even the hadronization of pure $q\overline{q}$ events induces a "false" $F_{\mathrm{L}}(x)$ by $p_\perp$ smearing. We have also here shown that a symmetric smearing around jet axes introduces a bias in the other direction, since it misses important string/drag effects that tend to make three-jet events more two-jetlike. In summary, there is no model-independent extraction of a unique $F_{\mathrm{L}}(x)$, especially not at small x values.

We therefore propose to introduce a scale-dependent quantity $F_{\mathrm{L}}(x, \mu^2)$. Particles are clustered, e.g. with the Durham algorithm, and thereafter assigned the θ angle of the cluster they belong to, while retaining their x value. Thus μ^2 sets an "un-smearing" scale, below which $p_\perp$ fluctuations are killed. We find that a $\mu \approx 1.3$ GeV gives opposite and compensating $p_\perp$ smearing and string effects in JETSET simulations. While the exact number certainly is model-dependent, the order is a sensible one, given that the average hadronization $p_\perp$ is of the order of 0.4 GeV. If this then sets a reasonably lower limit, an upper one is related to the desire to stay away from the region of exclusive two- or three-jet events. Over an intermediate range, one could imagine several experimental determinations providing the scale dependence. We also remind that, so far, our studies have only been intended for LEP1 energies. Coverage of a wider energy range, e.g. at LEP2, introduces s as a further scale of the process and allows more differential tests.

References

[1] T. Sjöstrand, Computer Phys. Commun. **82** (1994) 74.

[2] A. C. Hirschfeld and G. Kramer, Nucl. Phys. **B74** (1974) 211.

[3] G. Altarelli et al., Nucl. Phys. **B160** (1979) 301; Phys. Rep. **81**, (1982) 1.

[4] P. Nason and B. R. Webber, Nucl. Phys. **B421** (1994) 473, *e*rratum **B480** (1996) 755.

[5] OPAL Coll., G. Abbiendi et al., Eur. Phys. J. **C11** (1999) 217;
DELPHI Coll., P. Abreu et al., Eur. Phys. J. **C13** (2000) 573;
ALEPH Coll., R. Barate et al., Eur. Phys. J. **C17** (2000) 1.

[6] TASSO Coll., R. Brandelik et al., Phys. Lett. **B114** (1982) 65;
OPAL Coll., R. Akers et al., Z. Phys. **C68** (1995) 203;

ALEPH Coll., D. Buskulic et al., Phys. Lett. **B357** (1995) 487;
DELPHI Coll., P. Abreu et al., Eur. Phys. J. **C6** (1999) 19.

[7] B. Andersson, G. Gustafson, G. Ingelman and T. Sjöstrand, Phys. Rep. **97** (1983) 31;
B. Andersson, *The Lund Model* (Cambridge University Press, 1998).

[8] B. R. Webber, Nucl. Phys. **B238** (1984) 492.

[9] Yu. L. Dokshitzer, B. R. Webber, Phys. Lett. **B352** (1995) 451;
M. Dasgupta, B. R. Webber, Nucl. Phys. **B484** (1997) 247;
M. Beneke, V. M. Braun, L. Magnea, Nucl. Phys. **B497** (1997) 297.

[10] I. G. Knowles et al., in *Physics at LEP2*, eds. G. Altarelli, T. Sjöstrand and F. Zwirner, CERN 96–01, Vol. 2, p. 103

[11] B. Andersson, G. Gustafson and T. Sjöstrand, Phys. Lett. **94B** (1980) 211

[12] Ya. I. Azimov, Yu. L. Dokshitzer, V. A. Khoze and S. I. Troyan, Phys. Lett. **165B** (1985) 147

[13] JADE Coll., W. Bartel et al., Z. Phys. **C21** (1983) 37;
OPAL Coll., R. Akers et al., Z. Phys. **C68** (1995) 531;
DELPHI Coll., P. Abreu et al., Z. Phys. **C70** (1996) 179;
ALEPH Coll., R. Barate et al., Phys. Rep. **294** (1998) 1.

[14] T. Sjöstrand, Z. Phys. **C26** (1984) 93.

[15] P. Hoyer, P. Osland, H. G. Sander, T. F. Walsh and P. M. Zerwas, Nucl. Phys. **B161** (1979) 349.

[16] G. Marchesini, B. R. Webber, G. Abbiendi, I. G. Knowles, M. H. Seymour and L. Stanco, Computer Phys. Commun. **67** (1992) 465.

[17] for a review see e.g. S. Moretti, L. Lönnblad and T. Sjöstrand, J. High Energy Phys. **08** (1998) 001.

[18] S. Catani, Yu. L. Dokshitzer, M. Olsson, G. Turnock and B. R. Webber, Phys. Lett. **B269** (1991) 432.

[19] Ya. I. Azimov, Yu. L. Dokshitzer, V. A. Khoze and S. I. Troyan, Z. Phys. **C27** (1985) 65, Z. Phys. **C31** (1986) 213.

[20] A. H. Mueller, Phys. Lett. **104B** (1981) 161;
B. I. Ermolaev and V. S. Fadin, JETP Lett. **33** (1981) 269.

[21] Yu. L. Dokshitzer, V. S. Fadin and V. A. Khoze, Phys. Lett. **B115** (1982) 242; Z. Phys. **C15** (1982) 325; Z. Phys. **C18** (1983) 37;
A. Bassetto, M. Ciafaloni, G. Marchesini and A. H. Mueller, Nucl. Phys. **B207** (1982) 189.